β-DELAYED PROTON EMISSION IN THE ^{100}SN REGION

By

Giuseppe Lorusso

A DISSERTATION

Submitted to
Michigan State University
in partial fulfillment of the requirements
for the degree of

DOCTOR OF PHILOSOPHY

Physics

2010

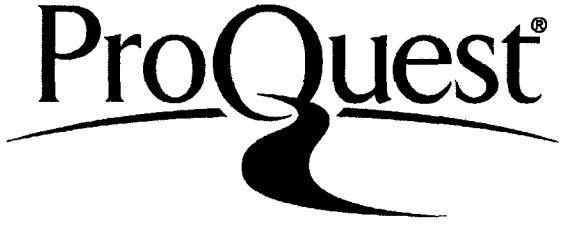

ProQuest LLC
789 East Eisenhower Parkway
P.O. Box 1346
Ann Arbor, MI 48106-1346

ABSTRACT

β-DELAYED PROTON EMISSION IN THE ^{100}SN REGION

By

Giuseppe Lorusso

The β-delayed proton (βp)- emission from nuclides in the neighborhood of ^{100}Sn has been studied at the National Superconducting Cyclotron Laboratory (NSCL). The nuclei were produced by fragmentation of a 120 MeV/u ^{112}Sn primary beam in a Be target, and separated using the A1900 Fragment Separator and the Radio Frequency Fragment Separator (RFFS). After production and separation, the nuclei of interest were identified and their decay mode have been studied with the NSCL Beta Counting System (BCS) in conjunction with the Segmented Germanium Array (SeGA).

This dissertation presents the identification of two new proton emitters: ^{96}Cd and ^{98}In, and the measurement of the βp-emission-branching ratio for all the nuclei studied: ^{92}Rh, ^{93,94}Pd, ^{95,96}Ag, ^{96,97,98}Cd, ^{98,99,100}In, and ^{101}Sn. In addition, nuclear structure data such as half-lives and the $p\gamma$ coincidences that can offer tests of nuclear structure theory. In particular, we report the first measure of the ground state of ^{97}Cd (1.1 sec) relevant for rp-process calculations, and the identification of a high-spin isomer in ^{97}Cd with half-life 3.8(2) sec.

The implications of the βp-emission on the astrophysical rp-process are studied using a single zone X-ray burst calculation. βp-emission in the ^{100}Sn region has an effect on the composition of the X-ray burst ashes and slightly alters the burning condition at a late stage. The newly measure ^{97}Cd half-life has also an impact on the rp-process calculations. The half-life –shorter than expected–affects the final isobaric composition of mass A=97 and, via βp-emission, also affects the final isobaric composition of A=96.

TABLE OF CONTENTS

LIST OF TABLES

LIST OF FIGURES

Chapter 1

Introduction

1.1 Motivation Overview

1.1.1 Nuclear physics motivation

Nuclei located on the Segre Chart around the classical doubly magic nucleus ^{100}Sn are a unique testing ground for the understanding of nuclear structure far from stability. The vicinity to a doubly magic core makes shell model calculations feasible, which can then be compared with experimental data to address specific nuclear structure questions [1–5]. The strong influence of the relatively high-spin $g_{9/2}$ shell on the valence nucleon or hole structure leads to a broad range of spin and seniority effects [6], including isomers. As $N \approx Z$ in this region, valence protons and neutrons occupy the same shell, thus enhancing the role of proton-neutron interactions. In addition, the large Q-values for β-decay enable the use of a particularly rich set of experimental tools to work with the relatively low production rates of these exotic nuclei. These tools include β-delayed γ and proton spectroscopy, and detection of direct proton emission. α-decay from the $Z > 50$ region offers an additional opportunity to probe the nuclear structure with high-detection efficiency [7].

One important question concerning the ^{100}Sn region is the existence of spin-gap isomers (see Section 2.2.1). Such isomers are sensitive probes of the proton-neutron interaction employed in shell model calculations. After the discovery of a $21/2^+$ β-decaying isomer in ^{95}Pd [8], it was demonstrated in [1] that shell model calculations can indeed explain the existence of this isomer, and similar spin-gap isomers were predicted to exist in ^{95}Ag ($23/2^+$), ^{96}Cd (16^+) and ^{97}Cd ($25/2^+$). As [1] also pointed out, the special order of states that makes ^{95}Pd isomeric is very sensitive to the details of the interaction. If for instance, the matrix element $\langle g^2_{9/2}|\ V_{pn}\ |\ g^2_{9/2}\ \rangle_{J=9}$ is changed by 40 keV, then ^{95}Pd would not be isomeric anymore. Since the predictions of [1], many more high-spin isomers with configurations generated by core excitations beyond the limited shell model space employed by [1] have been identified experimentally in this region, $^{94-97}$Ag, ^{94,96}Pd, and ^{98}Cd [4]. The subset of isomers predicted by [1] are of a particular importance as they can be used to test shell model calculations without additional complications such as core excitations. Among them, only the $23/2^+$ isomer in ^{95}Ag has been discovered experimentally so far [9, 10]. However, the isomer was observed by detecting its γ decay, and the lifetime turned out to be considerably shorter than originally predicted, making the existence of a significant β-decay branch unlikely. This work reports on first evidence for the existence of the predicted β-decaying $25/2^+$ isomer in ^{97}Cd. Our unsuccessful search for the remaining isomer predicted in ^{96}Cd was published before [11]. The ^{97}Cd isomer has the highest spin of the isomers predicted by [1] and is therefore of particular interest. While its existence probes the regular shell model space, its β-decay probes the presence of core breaking states in the daughter. In addition, nuclear structure data on a wide range of isotopes are presented, including ^{101}Sn, whose ground state spin is important to determine the single particle level ordering as probed by the single neutron outside the ^{100}Sn

core [12]. These nuclear data could constrain nuclear models.

1.1.2 Astrophysical motivation

Nuclei in the region below ^{100}Sn are also of interest for the understanding of the astrophysical rapid proton capture process (rp-process [13]) in type I X-ray bursts [14, 15]. Such bursts are the most frequently observed thermonuclear explosions. They are powered by the explosive nuclear burning of hydrogen and helium in a thin layer of fuel accumulated on the surface of an accreting neutron star (see Section 2.2.1). Models indicate that, under some conditions, proton captures and β decays drive the energy generating reaction sequence into the ^{100}Sn region, with α-unbound Te isotopes providing natural endpoints. Such an extended rp-process provides an explanation for sometimes observed very long bursts that can last for hundreds of seconds.

The lifetimes of the slower β-decaying isotopes in the rp-process, the so called waiting points, need to be known to predict the composition of the burst ashes. The composition is an important input parameter for neutron star crust models related to a number of observable phenomena [16]. With the recently reported measurement of the half-life of the ground state of ^{96}Cd [11] and the improved measurement of the half-life of ^{84}Mo [17], in principle, the ground state half-lives of all waiting points are now known experimentally. However, a remaining question is the existence of the predicted β-decaying high-spin isomer in ^{97}Cd, which could be an important waiting point. While such a high-spin isomer is unlikely to be populated in the rp-process, there is the possibility that the previously reported experimental ^{97}Cd half-life [2] is a mixture of ground state and isomer decays. The present work shows that this is indeed the case, and it reports for the first time the astrophysically relevant ground state half-life. In addition, β-delayed

proton emission further alters the composition of the burst ashes, which results from chains of β-decays, originating from the nuclei near the proton drip line that are synthesized during the explosive phase of the X-ray burst. If any of the nuclei in such a decay chain, with mass number A decay through βp-emission, the contribution of this particular chain to the first stable isobar of mass A will be reduced by a fraction equal to its βp-branching ratio. Similarly, the abundance in the neighboring decay chain with mass A-1 is increased especially if the chain with mass A is more abundant. X-ray burst models therefore, have to take this decay mode into account to predict realistically the ashes composition that of the X-ray burst ashes. Moreover, through the release of protons at late times in the burst, βp-emission has the potential to further alter burning conditions during an X-ray burst. βp-emission was also indicated as a possible factor to explain the outstanding question of the origin of the nuclei ^{92,94}Mo and ^{96,98}Ru, found in unexpectedly large amount in the solar system [18].

With the current experiment, a number of new β-delayed proton emission branching ratios along the rp-process were experimentally measured. This allows one to quantify the impact of βp-branching ratios on the rp-process, in the mass A=92—101 region.

1.2 β-delayed proton emission

1.2.1 Introduction to β-delayed proton emission

When the β-decay process populates excited states in the daughter nucleus that are above the proton separation energy S_p (the energy required to remove the last proton to infinity), these states can be de-excited via proton emission, provided that this decay mode occurs faster than the competing γ-decay. The whole process,

schematically represented in Figure 1.1, occurs with the half-life of the β-decay, which is orders of magnitudes slower than the proton emission. In most cases, the

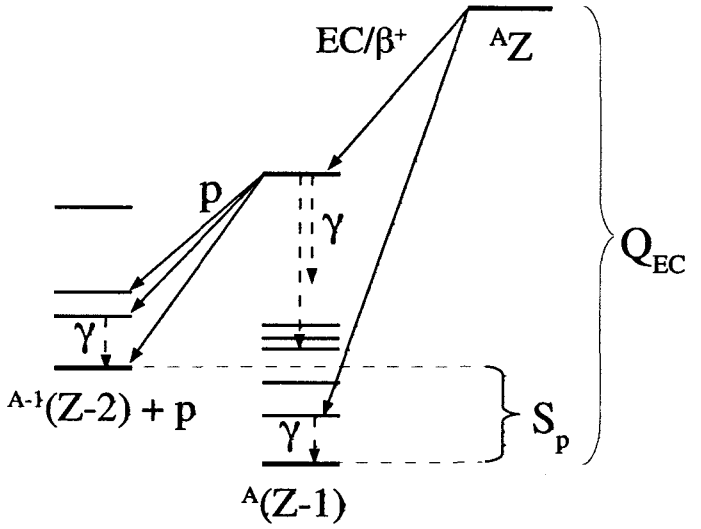

Figure 1.1: Schematic decay scheme illustrating the βp-emission process. β-decays into daughter excited states above S_p can result in a subsequent proton decay. Competing γ-decays are labeled with dashed arrows.

β-decay mode of a nucleus ^{A}Z populates multiple states in the daughter nucleus ^{A}(Z-1) each having different probabilities for a proton decay into several final states, in the $^{A-1}$(Z-2) nucleus. The fraction of proton decays observed per β-decay defines a quantity, the β-delayed proton emission branching ratio $P_{\beta p}$, which is directly observable. The half-life of the proton emission depends strongly on energy and angular momentum carried by the proton, which has to tunnel through Coulomb and centrifugal barriers. Details of the nuclear interior are important as well, and are described by spectroscopic factors defined as the overlap between the wave function of the parent and daughter nuclei. All these factors are contained in the proton width Γ_p (see App. A) related to the proton emission lifetime simply as $\tau=\hbar/\Gamma_p$. A similar quantity, Γ_γ, is defined for γ-decay. The competition between proton and gamma decay is then described in terms of the magnitudes of Γ_p and

Γ_γ.

The first prerequisite for βp-emission is a large energy window for a proton decay defined as the difference between the Q-value of electron-capture decay Q_{EC} and the proton separation energy S_p in the daughter nucleus. Q_{EC} is equal to the atomic mass difference between parent and daughter nuclei. The two quantities, Q_{EC} and S_p, are illustrated in Figure 1.1. It is useful to look at the behavior of these two quantities along isotopic chains because they can help us to interpret the trends in βp-emission strength. The trends shown in Figure 1.2(a) and Figure 1.2(b) for Q_{EC} and S_p, respectively are limited to the neutron deficient region around Z=50, but they are found to be similar elsewhere on the nuclear chart. Q_{EC} increases systematically with decreasing number of neutrons N. On the other hand, along the same chains, S_p decreases with decreasing N. The same figures also show a sudden increase of Q_{EC} and drop of S_p after specific magic numbers of protons and neutrons, in this case Z=50. The described trends of Q_{EC} and S_p lead to a broadening of the energy window Q_{EC}–S_p available to βp-emission as one moves towards the proton drip line (see Figure ??), and consequently to an increased probability of β-delayed proton emission.

β-delayed proton emission manifests itself in quite different ways in light and heavy nuclei. In light nuclei protons are emitted from well separated levels so that individual transitions can be identified in the proton energy spectra (see for example Figure 1.4). In medium and heavy nuclei, on the other hand, the relevant region of excitation energy tends to have too high of a level density to make observations of singular transitions possible. Instead, proton spectra exhibit a several MeV wide bell-shaped distribution dependent on average properties of excited states in the proton emitter (see for example Figure 1.5(a) and Figure 1.5(b)). In most cases a peak structure on top of the average smooth behavior is not due to single

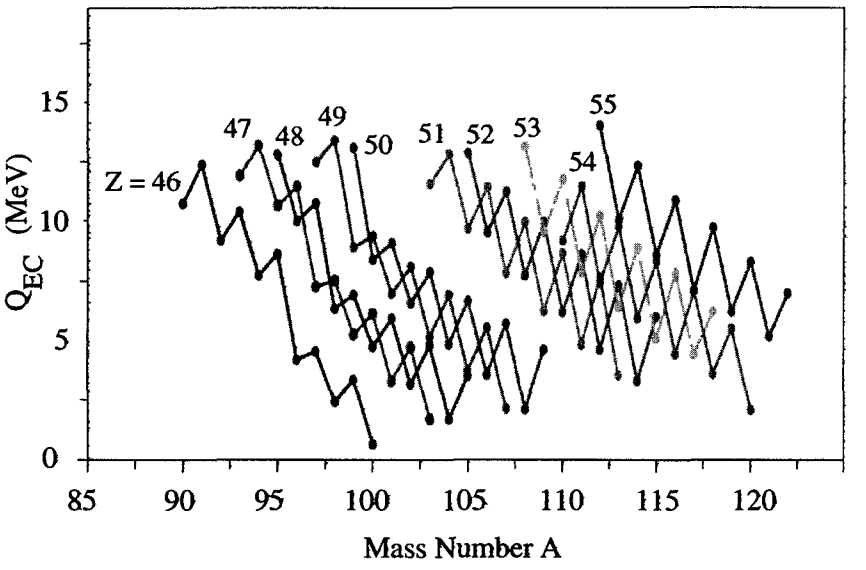

(a)

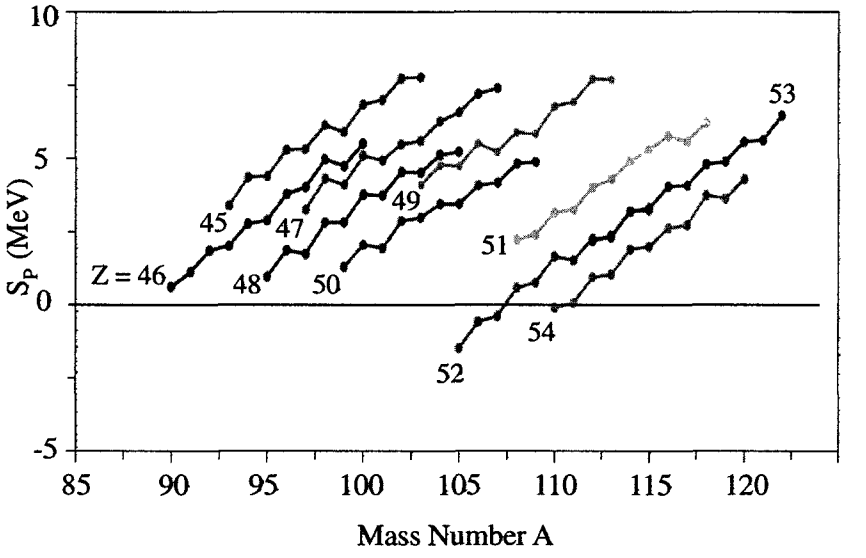

(b)

Figure 1.2: a) Q_{EC} values for isotopic chains near Z=50 and b) S_p for the same isotopic chains.

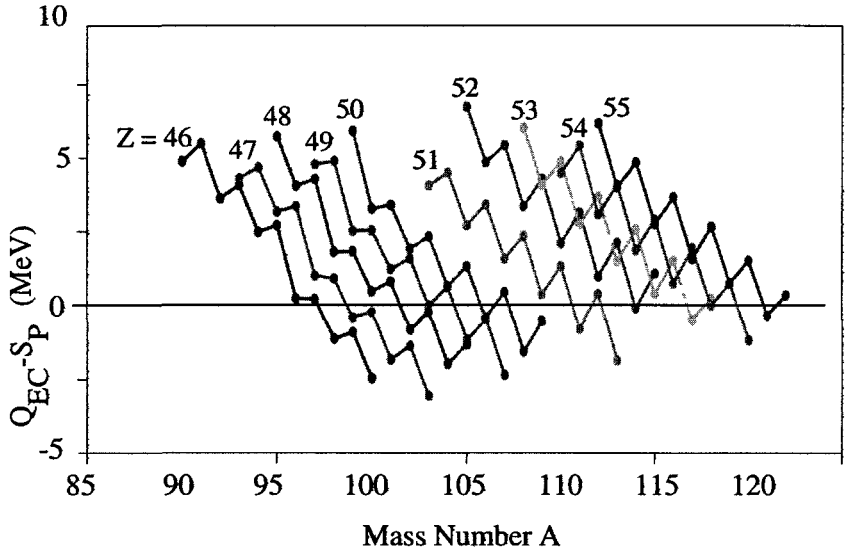

Figure 1.3: Q_{EC}-S_p window near Z = 50.

strong transitions, but rather due to clusters of transitions. These peak structures are described as fluctuations in the transition probability and they follow the Porter-Thomas law [20].

The bell-shaped proton spectra in medium and heavy nuclei, result from the competition of two factors. The low-energy part of the spectrum reflects the increasing probability Γ_p for protons to tunnel through the Coulomb barrier with increasing proton energy:

$$\Gamma_p = 2P_l(k)\gamma^2 \tag{1.1}$$

where γ^2 is the reduced width (see App. A) describing the effects of the nuclear interior. The energy dependence of Γ_p is contained in the penetrability factor $P_l(k)$ (see App. A),

$$P_l = R\left(\frac{k}{F_l^2 + G_l^2}\right)_{r=R} \tag{1.2}$$

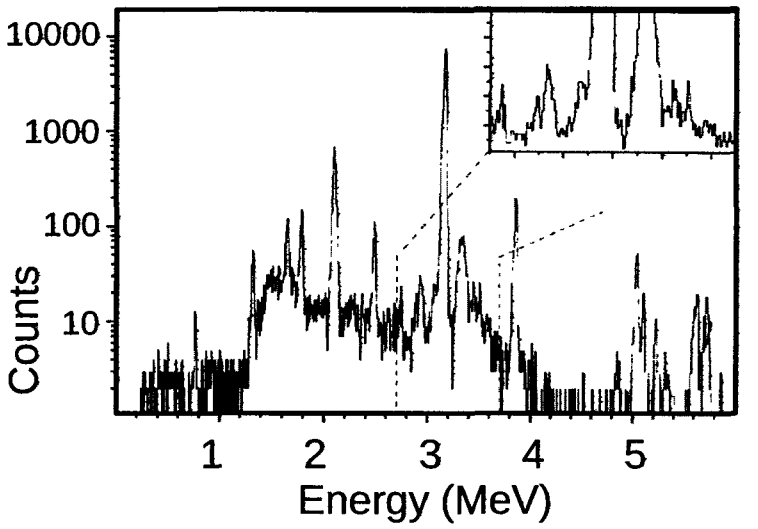

Figure 1.4: β-delayed proton emission spectra for ^{33}Ar. Peaks corresponding to transitions from states in ^{33}Cl into states of ^{32}S are identifiable [19].

where k is the proton wave number $p/\hbar$, and F_l and G_l are the Bessel and Newman functions. The higher-energy part of the proton spectra receives contributions from high-excited states in the proton emitter. For these states, $\Gamma_p \gg \Gamma_\gamma$, and hence the proton intensity is determined by the feeding from the β-decay. At high energy the proton spectrum decreases because of the decreasing density of final states in the phase space accessible to β-decay described by the following expression:

$$\frac{dN_f}{dE} = \frac{1}{4\pi^4\hbar^6c^5}p_e^2\left(Q - \sqrt{p_e^2 + m_e^2}\right)^2 dp_e \tag{1.3}$$

where dN_f/dE is the density of final states per unit energy in the β-decay daughter nucleus, Q is the β-decay Q-value ($Q=Q_{EC}-2m_e$), and p_e is the electron momentum. Equation 1.3 shows that for small electron momentum (β-decay into high-excited states of the proton emitter) the phase space is proportional to p_e^2 and eventually vanishes at $p_e = 0$.

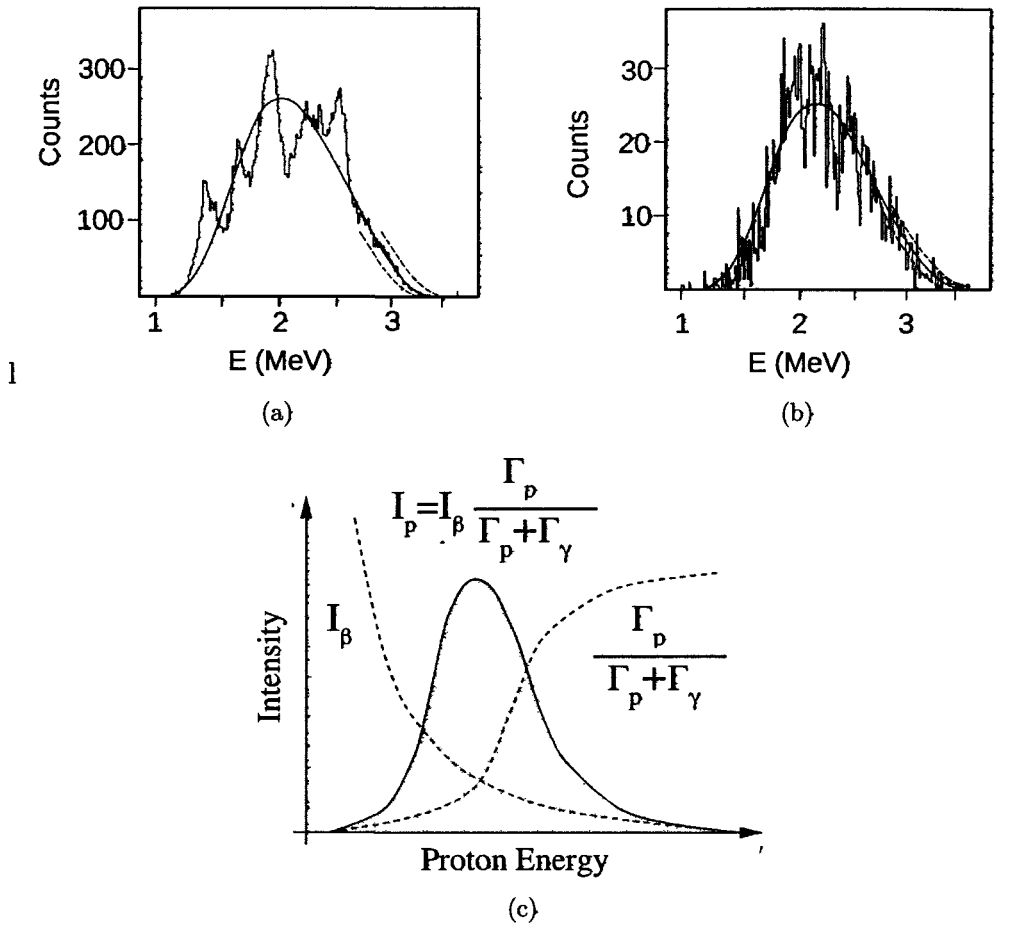

Figure 1.5: β-delayed proton emission spectra for a) ^{77}Sr and b) ^{69}Se. A bell shaped curve calculated using a statistical model is superimposed to the experimental spectra [21]. Panel c) shows the qualitative explanation of the shape of the βp-energy spectrum resulting from folding β-decay intensity and proton branching ratio.

Taking both effects into account, the proton energy distribution can be expressed as a function of the β-decay intensity I_β^i to populate a state i in the emitter ^{A}(Z-1), and the branching for proton-emission into a final state f of the nucleus $^{A-1}$(Z-1).

$$I(E_p) = \sum_{i,f} I_\beta^i \times \frac{\Gamma_p^{if}}{\Gamma_p^i + \Gamma_\gamma^i} \tag{1.4}$$

with

$$\Gamma_p^i = \sum_{f'} \Gamma^{if'} \tag{1.5}$$

Equation 1.4 is shown qualitatively in Figure 1.5(c).

In lighter nuclei, due to the lower level density, the average behavior is less evident, and the bell curve shape of the proton spectrum is less evident. However, the low energy cut-off, and the tapering off at high energy are due to the bell like tails in the energy dependent proton intensity.

It is interesting to note that proton energy spectra carry some signature of the odd-even staggering of nuclear masses. Odd-odd precursors have high Q_{EC}, and they β-decay in even-even nuclei that have high S_p. Therefore, protons are emitted from states that have high excitation energy and where the density of states is high, resulting in a smoother spectrum than in the case of even-odd precursors. In the latter case, indeed, Q_{EC} and S_p are smaller, the level density is lower, resulting in more pronounced structure in the proton energy spectrum.

It has been shown in [21, 22] that statistical model calculations can reproduce the average features of the bell-shaped spectra (see Figure 1.5) and that the difference Q_{EC}–S_p can be extracted from a fit of the calculated energy spectra to the experimental energy spectra. The uncertainty reported by [21] range between 50—200 keV. Although the results are model dependent, a certain insensitivity to the details of the calculation (β-decay strength and density of states) has been observed [21].

1.2.2 Historical background

The application of isobaric invariance principles led Goldansky, Baz, and Zeldovich in 1959 to the following relation between the proton separation energy in the

nucleus ${}^{A}_{Z}X_{N}$, and the neutron separation energy in the mirror nucleus ${}^{A}_{N}Y_{Z}$ [23]:

$$E_n({}_{N}Y^{A}_{Z}) - E_p({}_{Z}X^{A}_{N}) \approx 1.2\frac{Z-1}{(2Z-1)^{1/3}} \tag{1.6}$$

This allowed [23] to calculate masses for about 20 experimentally unknown neutron-deficient nuclei up to Z=34. Moreover, it follows from Equation 1.6 that,

$$E_{\beta+}(\Delta T = 0) \approx 1.2\frac{Z}{A^{1/3}} - 1.8 \text{ MeV} \tag{1.7}$$

Equation 1.7 states that if the energy of the β-decay exceeds the threshold for superallowed β-decay $\left(1.2\frac{Z}{A^{1/3}} - 1.8\right)$ MeV, these β-decay to excited states occurring without isospin change (ΔT=0) is possible, and thus a significant fraction of β-decays is expected to populate excited states that can be deexcited by β-delayed photons and/or proton emission. Based on Equation 1.7, [23] predicted the existence of nuclei that decay by β-delayed one- and two-proton emission, and nuclei that decay by one- and two-proton emission.

Given the uncertainties in the mass model (Equation 1.6) of about 1 MeV for the proton binding energies, [23] could estimate the location in the nuclear chart where protons are no longer bound (proton drip line) within 3-4 nuclei. However, [23] predicted that whenever the proton drip line was crossed, the lifetime of the nuclei would decrease rapidly down to picoseconds within a small number of isotopes. In light nuclei the lifetime would decrease faster because of the lower Coulomb barrier. In many cases the direct proton emission is predicted to be too short to be observable [23]; in these cases, β-delayed proton emission would be the decay mode of the lightest observable isotope with a given Z.

β-delayed proton emission was first identified in Dubna by Karnauklov and collaborators [24]. However, the identification of the precursor was not possible.

The first identification of a proton emitter was ^{25}Si in 1963 [25]. Further research on light nuclei (Z>N) led to the realization that a simple qualitative systematics can be drawn for the size of beta-delayed proton emission branching, based on the value of T_z=(Z-A)/2 and taking into account pairing effects (see review [26]). For example, even-odd nuclei with T_z=-3/2 from ^{9}C to ^{65}Ge are all strong β-delayed proton emitters, with β-delayed branching ratios ($P_{\beta p}$) ranging from 12% to 100% [25]. Odd-even nuclei with T_z=-3/2 are instead much weaker emitters, with $P_{\beta p}$ usually <1% [27]. These two groups of nuclei form the (A=4n+1, T_z=-3/2) and (A=4n+3, T_z=-3/2) series, respectively (where n=1,2.....).

Despite nuclei with T_z=-2 being more proton rich than nuclei with T_z=-3/2, they are not stronger proton emitters (see App. C). This is because they are either even-even or odd-odd nuclei. However, it is clear that in this group, odd-odd nuclei are stronger β-delayed proton emitters than the even-even ones.

There are only four known β-delayed proton emitters in the T_z=-5/2 group: ^{23}Si, ^{31}Ar, ^{35}Ca, ^{43}Cr. They can be directly compared with the T_z=-3/2 group because they have the same parity features, and hence proton excess is the only main difference. These T_z=-5/2 nuclei are very strong emitters, with $P_{\beta p}$ that ranges between 65% and 100% (see App.C) and $\beta 2p$-branching ratios of about 5%. The weakest series (A=4n, T_z=-1) starts at ^{24}Al with $P_{\beta p}$<1%. Odd-even T_z=-1 nuclei are not proton emitters. Therefore, nuclei with T_z=-1 are the first ones in the nuclear chart that show β-delayed emission.

β-delayed proton emission in this light region has been used to measure the energy of excited states in the proton emitting daughter nucleus, their β feeding, to make spin assignments, and to identify isobaric analog states (see for example [28, 29] or review [30]). An remarkable application is related to measurements of isospin mixing of excited states in the emitters. For example, the β-decay study

of ^{33}Ar [19] revealed that the T=3/2 state in ^{33}Cl undergoes proton decay into a T=0 state in ^{32}S. Because the proton itself has T=1/2, this decay is possible only if the T=3/2 state in ^{33}Cl is mixed with some neighboring state with T=1/2. The isospin purity of a state can be deduced by comparing the value of the super-allowed transition branch intensity, or log ft value, to the one expected from theory between perfect T=3/2 analog states.

Among light nuclei, the predicted [23] β-delayed two-proton emission has been observed in ^{6}Be, ^{12}O, ^{22}Al, ^{26}P, ^{35}Ca, ^{23}Si, ^{27}S, ^{31}Ar, ^{43}Cr and ^{35}Ca [31]. This phenomenon has attracted interest since it was hoped that its study would provide some information on correlations inside nuclei. In cases of multiple particle emission, there usually are three emission mechanisms. In sequential emission, an intermediate state is populated after the first proton emission, which then proton decays emitting the second proton. In the simultaneous emission and the ^{2}He emission. Experiments have shown that in the βp-emission process, the sequential emission is the dominant mechanism [32].

For heavier nuclei (Z>30), the situation is rather different, and as will be explained in the next section, βp-emission as a direct spectroscopic tool is not useful. However, from the end-points of the βp-energy spectra some information has been extracted about the beta decay Q value [21,22]. β-delayed proton emission, in particular $\beta p\gamma$-spectroscopy, is still an important tool for nuclear structure studies. For example, in cases where isomeric states are present that β-decay, the first signature of such isomeric states is a different half-life for β- and βp-decay [2,3]. Many βp-emitter have been identified, but their β-delayed proton emission branching ratio ($P_{\beta p}$) is still not measured (see App. C), so in most cases extended systematic trends beyond Z>30 can not be studied. The only such systematics observed are A=4n+1, T_z=+1/2 nuclei from ^{65}Ge to ^{85}Mo [33,34]. In this range $P_{\beta p}$ are small,

of the order of 0.1%. One aim of this work is to extend this series up to ^{101}Sn.

1.3 Previous measurements

The ^{100}Sn region has become accessible for study in the last 30 years. Experiments have been performed mostly using the fusion-evaporation technique. All the experiments (unless specifically mentioned) discussed in this section have been performed using beams provided by the GSI UNILAC (typically ^{40}Ca and ^{58}Ni beams) and were separated at the GSI on-line mass separator. While very high production rates can be achieved, this technique encounters a fundamental limitation when it is used to measure $P_{\beta p}$. Due to the low energy of the radioactive beams upstream detectors to count the number of incoming nuclei for a specie cannot be used. β p-branching can only be determined when the βp-intensity can be compared to the β-intensity inferred for example from characteristic β-delayed gamma radiation. The projectile fragmentation method used here is complementary. While production rates are much lower, individual incoming beam particles can be identified, counted and correlated to the detected individual decays thereby allowing for a much more efficient $P_{\beta p}$ determination even for very weakly produced isotopes.

An important experiment in which β-delayed protons were observed from progenitors in the ^{100}Sn region was performed in 1982 at the Munich MP tandem; nuclei of ^{95}Pd were produced through the reaction ^{58}Ni(^{40}Ca,n2p). Protons were observed stemming following the β-decay of the $J^{\pi}=(21/2^{+})$ isomeric state. In the same year a βp-decay study in this region was performed by [35], which identified the ground state proton precursors ^{96}Ag, ^{97}Cd and ^{100}In. The study also reported half-life determinations for ^{96}Ag and ^{97}Cd, finding 5.1(4) and 3^{+4}_{-2} s, respectively.

For ^{96}Ag $P_{\beta p}$=8.0(23)% was determined. This study exemplifies the challenging measurements in this region. In fact, 15 years after this experiment, evidence was found for the existence of a ^{96}Ag isomeric state, which along with the ground state undergoes β- and βp-decay [2]. This implies that the half-life and $P_{\beta p}$ measured were mixture of activities. Five yeas later, the individual determination of half-life and $P_{\beta p}$ of the ground state and the isomeric state finally succeeded [3]. ^{97}Cd is a similar case in that a half-life measurement exist that would not be sensitive to the presence of two components. Indeed, the present work confirm the existence of a predicted β-decaying isomer and provides separate half-lives and $P_{\beta p}$ for ground state and isomeric states for the first time. The half-life inferred by [35] is revised in the current work.

Another important study of βp-emission in the region was reported by [2], who studied ^{95,96}Ag and ^{97}Cd, and reported a proton energy spectrum for ^{97}Cd for the first time. However, they were not able to determine $P_{\beta p}$ for ^{97}Cd. Two experiments [36, 37] were dedicated to the study of ^{93}Pd motivated by the special role of ^{93}Pd as waiting point in the rp-process. These experiments allowed for a half-life determination and spectroscopic details of the β- and βp-daughters ^{92}Rh, ^{93}Ru. However, no $P_{\beta p}$ was obtained. The nucleus ^{100}In was studied in [38] motivated by its proximity to ^{100}Sn. The study also detected βp-decays and measured $P_{\beta p}$=1.6(3)%. The latter value is the only reasonably precise one in the region that can be compare to our work as a test of the method. The βp-decay of ^{101}Sn was studied in [39] who recorded the spectrum and determined $P_{\beta p}=14^{+15}_{-10}$%. These results were later used by [40] to show that the shape of the proton spectrum has some sensitivity to the ground-state spin of ^{101}Sn, however the results were somehow inconclusive due to the large uncertainty in the nuclear physics parameter such as masses and level densities, which enter the shell model calculations used

to connect the proton spectrum with the structure of ^{101}Sn.

1.4 This work

This dissertation details a study of the β-delayed proton emission properties of a wide range of nuclei in the ^{100}Sn region: ^{92}Rh, ^{93,94}Pd, ^{95,96}Ag, ^{96,97,98}Cd, ^{98,99,100}In, and ^{101}Sn. The study had several goals: a) measure β-delayed proton emission branching ratios particularly of nuclei along the rp-process path, b) identify new β-delayed proton emitters, c) search for β-decaying isomeric states, in particular the predicted 16^+ state in ^{96}Cd, and $25/2^+$ in ^{97}Cd, and d) using $\beta p\gamma$ coincidences to reveal new nuclear states.

To achieve these research goals, an experiment was run at the National Superconducting Cyclotron Laboratory, at Michigan State University using the new RF Fragment Separator system. A mixed beam containing the nuclei of interest was produced by fragmenting a heavy ion beam on a light target. The products o fragmentation were selected, identified, and implanted in a stack of silicon detectors. The nuclei implanted were observed to decay emitting positrons and protons that were detected by the stack itself. γ rays emitted in the decay process were detected by 16 germanium detectors surrounding the silicon stack. A detailed description of this is given in Chapter 3. The following Chapter 2 provides a more detailed motivation for studying the ^{100}Sn region, and provides a more detailed introduction to the nuclear physics and astrophysics of these nuclei. Chapter 4 and Chapter 5 report the analysis of the raw data and its results, respectively. In Chapter 6, the impact of new measurements on the astrophysical rp-process is discussed. Finally, Chapter 7 provide a summary and outlook.

Chapter 2

Nuclear physics and astrophysics of the ^{100}Sn region

2.1 Topical subjects in the ^{100}Sn region

This section aims to highlight some special features of nuclei in the ^{100}Sn region, and it is divided in two parts. The first part is dedicated to some interesting manifestations of the residual interaction between protons and neutrons occupying the same shell. The second part is dedicated to different kinds of isomers occurring specifically in this region as a result of the occupancy of the $g_{9/2}$ shell.

2.1.1 Singular features of the N~Z nuclei

Neutrons and protons can couple in either the isovector (T=1) or the isoscalar mode (T=0). Away from the N=Z line, neutrons and protons have a poor spatial overlap, thus the T=1 interaction dominates. For N~Z, however, protons and neutrons fill identical orbits and apart from Coulomb effects their wave functions should have nearly complete spatial overlap; consequently the T=0 interaction,

which is empirically known to be about twice as strong as the T=1 interaction, can dominate. To date, it is not clear in which way the isoscalar component manifest itself and how important it is. Predictions are that T=1 dominates up to mass A=80 and then T=0 starts becoming more important [41]. The isoscalar interaction is important because it is thought to play a role in effects like single particle configuration mixing, the onset of collectivity, and deformation. In the following, some of these effects are summarized.

p-n pairing effects

In nuclei just below ^{100}Sn, protons and neutrons are filling the same shell and, as mentioned above, the residual interaction between non-identical valence nucleons is particularly strong. This interaction is attractive, and its strength depends on the alignment of particle-particle or hole-hole configurations as it becomes stronger for nearly maximum aligned configurations. It is for these reasons that high-spin states may receive an extra binding compare to low-energy states. Consequently, in odd-odd N=Z nuclei, the state with J=2 j resulting from the coupling of the unpaired proton to the unpaired neutron may become the ground state and there could even be a significant *pairing gap* between the ground state and the first excited state despite this being an odd-odd nucleus.

Also, if a nucleus is non spherical and rotates, the Coriolis force would not affect the two unpaired nucleons differently, in contrast to even-even nuclei where force tends to break J=0 nucleon pairs, hence any backbending might be delayed to high spin.

Another manifestation of the T=0 interaction is in the binding energy. In light nuclei, there is a large difference in binding energy between a N=Z nucleus and its neighbors; however, this energy difference decreases with increasing A. This is

interpreted as the fact that in heavier nuclei protons and neutrons are filling orbits with smaller overlap and their wave functions are also spread out to larger volumes. Therefore, short range interactions will be weaker. However, it is not understood if this is the only reason or there is also a p-n interaction orbit sensitivity [42].

The isoscalar interaction is also expected to give a larger contribution to the single-particle-configuration mixing than the isovector interaction. Consider for example two particles in two different orbits. Unless the two orbits are close in energy, the T=1 configurations of identical nucleons will be less mixed than the T=0 of non-identical nucleons simply because in the T=1 case, the Pauli principle restricts the number of possible total spin states allowed, and the matrix elements that are not null may be small.

Another effect maximized in N=Z nuclei is the mixing of states with different isospin. Indeed, for N=Z nuclei, the number of allowed isospin values, ranging from |N-Z|/2 to (N+Z)/2, is maximized for a given A. Moreover, the level density is higher in N$\sim$Z nuclei because some of these states do not exist in the neighboring nuclei (e.g. states with T=0), so states are closer in energy ans isospin mixing is more easily achieved. Owing to the fact that ^{100}Sn is the heavier N=Z nuclear isospin mixing due to the Coulomb field is expected to be particularly strong in the ^{100}Sn region. HFB calculation plus RPA show for example that in the case of ^{56}Ni this effect is 1%, and that increase approximately as Z^2 for heavier masses, hence it is about 5% in ^{100}Sn [43]. It is also interesting to understand which other interactions contribute to the break-down of isospin purity as one moves toward heavier masses. There are some evidence that the nuclear force may not be isospin independent [44]. This effect of isospin mixing can be detected experimentally because they can affect both the β- and γ-decay. For example in N=Z nuclei, Fermi β-decay as well as E1 transitions are forbidden unless isospin mixing is

present. Detecting such decays can indicate the degree of mixing.

Enhanced collective behavior

The shape of the nucleus as one of the fundamental nuclear properties is determined by both microscopic feature and macroscopic liquid-drop-like properties. In nuclei with partially filled shells, the valence nucleons tend to polarize the core towards a deformed mass distribution. The deformation can be described by a multipole expansion with the quadrupole deformation being the most important deviation from the spherical shape. An axially deformed quadrupole shape can be either elongated (prolate) or flattened (oblate). A deformation can be triaxial with different elongation along the three different axes of the system (triaxial shape). In some regions of the nuclear chart, the shape is very sensitive to proton or neutron number and changes from one nucleus to another. It can also change with the excitation energy or the angular momentum within the same nucleus. Interestingly, in light nuclei prolate and oblate shapes occur more or less equally, while in heavier nuclei (Z>50) where the shell structure changes from a harmonic oscillator type to a Meyer-Jensen type with intruder orbitals, a dominance of prolate shapes has been observed. This has been related to the strength of the spin-orbit interaction relative to the radial term in the nuclear interaction. For a high degree of collectivity the energy of the first 2^+ state will be low, while is expected to be maximum at shell closure for nuclei exhibiting pure single particle degrees of freedom.

The recent study [45] of $^{110}_{52}$Xe (4 valence protons and 6 valence neutrons outside the ^{100}Sn core) has extended the energy systematics of the first 2^+ excited state $E(2_1^+)$ and first 4^+ excited state $E(4_1^+)$ along the isotopic chain $^{110-136}$Xe. Such energy are valuable indicators of the nuclear deformation and collectivity in even-even nuclei [46, 47]. For a high level of collectivity, E(2+) and E(4+) will be low

whereas they are expected to be maximum at closed shell for spherical nuclei. the ratio $E(4^+)/E(2+)$ is also important as it is small for spherical nuclei and increase with collectivity. Considering the energy E(2) and E(4) is similar to consider the transition strength $B(E2,2^+\rightarrow 0^+)$ and $B(E2,4^+\rightarrow 2^+)$ as the two are related by a systematics relationship [46, 47].

^{136}Xe with high $E(2^+)$ and small $E(4^+)/E(2+)$ ratio exhibits characteristics of a rigid sphere. As the neutron number decreases, the collectivity signature become stronger with $E(2^+)$ being minimum and $E(4^+)/E(2^+)$ reaching maximum at around the midshell N=66. As the neutron number is decreased further, the trend of decreasing E(2+) and increasing E(4+)/E(2+) is initially inverted, until N$\approx$58 where a different pattern start to emerge with a $E2_1^+$ and $E4^+$ not increasing. At N=56 not only $E2^+$ does not increase, but $E4^+$ starts decreasing, indicating a collectivity nature much stronger then expected, given the vicinity of the N=Z=50 double shell closure.

Similar features have also been observed recently in the neutron deficient ^{106}Te (2 valence proton and 4 valence neutron outside the ^{100}Sn core) [48]. The isotopic chain $^{106-134}$Sn also shows signature of deformation [49]. The $B(E2,2^+\rightarrow 0^+)$ trend between $^{106-112}$Sn is in fact constant with A, in a significant disagreement with shell model calculations [50] predicting a gradual decrease of $B(E2,2^+\rightarrow 0^+)$, and hence a typical spherical shape approaching ^{100}Sn. These unusual features suggest an enhanced collectivity behavior possibly raising from the isoscalar np-interaction that becomes increasingly important near the N=Z line [49].

There are regions of the chart of nuclei where the deformed shapes (prolate, oblate, and spherical), seem to coexist in the same nucleus at similar energies. In same cases such us ^{68}Se two distinct bands have been observed [?], but if the two bands have levels that come close in energy, for the same spin and parity they can

be mixed in the wave function and cause a distortion of the rotational bands. For the ^{100}Sn region, the existence of the spherical shell gap at nucleon number 50lead to the expectation that also nuclei with N$\sim$Z could show shape co-existence [51].

2.1.2 Nuclear isomerism

Spin-gap isomerism

In nuclei just below ^{100}Sn, a strong interaction between protons and neutrons filling identical orbitals is expected to exist and to be attractive, and stronger in higher spin state configurations. For this reason, high-spin states gain some extra binding, which may lead to an inversion with higher-spin states shifting below states with lower spin. This results in gamma decays that correspond to transitions between states with large spin difference, and consequently the halftimes of these decays are long because transitions between states with large spin differences require high multipolarity such us M3, E4 or E6. For example, in ^{95}Pd, the first $21/2^+$ state has lower energy than the first $15/2^+$ and $17/2^+$ states. This inversion would create a spin gap isomer, since the $21/2^+$ state could be deexcited only by β-decay competing with E4 γ-decay to the first $13/2^+$ state. This case was first explained by [1] using shell model calculation in the $\pi\nu$ ($p_{1/2}$, $g_{9/2}$) valence space and based on the hole-hole configuration $\pi g_{9/2}^{-2}$ $\nu g_{9/2}^{-1}$. Using the same model space [1] also predicted the states $23/2^+$ in ^{95}Ag, 16^+ in ^{96}Cd [1], and $25/2^+$ in ^{97}Cd to be isomeric. The $23/2^+$ isomer in ^{95}Ag has been already established [9] while the other two so far have not been found experimentally. The discovery of the ^{97}Cd isomer is the subject of this work. large scale shell model calculations in the *gd*-space also predict the existance of isomeric states such as in ^{98}Cd, ^{96}Ag, ^{96}Pd, ^{97}Ag, ^{99}In, and ^{100}Sn [4]. In only one case, ^{98}Cd, the excitation of a neutron in

the configuration $g_{9/2}^{-1}(g_{9/2}^{-1}g_{7/2})^1$ is predicted to be isomeric. However this has not been observed yet. All known or predicted isomers in this region are represented in Table 2.1. Finally, the recent discovery of a 21^+ isomeric state in ^{94}Ag has shown that to reproduce the 21^+–19^+ leading to the formation of an isomer one has to account for up to 4p-4h (4 particle 4 hole) excitation. The same mechanism is predicted to create a 6^+ isomer in ^{100}Sn [4].

Low-energy J=1/2$^-$ isomers in odd-A nuclei

The odd-A nuclei in the ^{100}Sn region have a configuration in which protons and neutrons fill partially the $g_{9/2}$ shell, with one nucleon (either a proton or a neutron) unpaired, resulting in a J=9/2$^+$ ground state spin. However, a hole excitation from the $p_{1/2}$ into the $g_{9/2}$ shell would result in a configuration with all $g_{9/2}$ nucleons coupled to J=0$^+$ and a hole left in the $p_{1/2}$ shell resulting in a J=1/2$^-$ state [2]. Detailed properties of such a state depend crucially on its excitation energy which is not well constrained within the shell model. However, because the $p_{1/2}$ and $g_{9/2}$ shells are close in energy, this state is likely to be the first excited state and hence can only decay into the $9/2^+$ ground state via an M4 transition. Since the M4 transitions are usually slow, J=1/2+ state can turn to be an isomeric state with a competing β-decay branch. A detailed discussion about the properties of this state in the case of ^{97}Cd are summarized in section 5.1.3, and serves as a good example for other J=1/2$^-$ isomers in the ^{100}Sn region.

[1]The 96Cd isomer is particularly interesting because isomer in even-even nuclei are very rare. To date, only three of them have been confirmed experimentally (J=12+ in 52Fe, J=16+ in 178Hf, and J=(16)+ in 212Po).

Seniority isomers

Near magic nuclei where there are only few nucleons outside the core, single particle excitations may dominate over collective nuclear behavior. In particular, in even-even nuclei, a two particle ground state band (0^+, 2^+, 4^+ ..... (2j-1)) can emerge when a pair of nucleons in a j shell, that are coupled to J=0^+ in the ground state, breaks. In these cases the seniority, defined as the number of particles that are not in pairs coupled to spin J=0^+, is a good quantum number, and the description of the band in terms of a seniority scheme provides a simple yet successful interpretation [52]. In such a scheme, meaningful when the nuclear interaction is dominated by the J=0 pairing interaction, a pair-coupled basis that diagonalizes the interaction is chosen. Seniority numbers are eigenstates of this basis. A two particle system coupled to J=0+ has seniority ν=0 and ν=2 otherwise. A three-particle system has seniority 1 or two. In comparison with the rotational band, the behavior of the B(E2; $2^+ \rightarrow 0^+$) values along an isobaric chain are very similar, being parabolic as j fills in, with a maximum at mid-j shell. However, and interestingly, the behavior of the B(E2; $J \rightarrow J-2$; $J \geq 2$) values is also parabolic, but downward, with a minimum value at middle-j shell. This very different behavior is due to the fact that the transition $2^+ \rightarrow 0^+$ changes seniority, while every other ones ($J \rightarrow J-2$; $J \geq 2$) do not. Calculations show that the value B(E2; $8_1^+ \rightarrow 6_1^+$) is often very small [53], making the transition forbidden and the 8_1^+ state isomeric. It is also very interesting that the same seniority scheme also explains the disappearance of certain 8_1^+ isomers. Sometimes, the ν=4 6_2^+ state has a lower energy than 8_1^+ state and because the seniority is not exactly a good quantum number, the transition $8_1^+ \rightarrow 6_2^+$ is possible, and the 8_1^+ is not isomeric anymore. Seniority-spin isomers are known also in the ^{100}Sn region along the isotonic chain N=50. The isotonic chain N=51, and the isotopic Z=50 on the left of ^{100}Sn are

also predicted to have good seniority thus isomers can be discovered [54]. These predictions rely, however, on the assumption that far from stability magic numbers are not altered.

2.2 Type-I X-ray bursts

Nuclei in the ^{100}Sn are also important to understand type-I X-ray bursts occurring in a layer of fuel accumulated on the surface of an accreting neutron star. In this section, some basic features of the astrophysical site of the X-ray bursts, their main observational properties, and the nuclear burning mechanism are summarized. A particular type of burst, the Photospheric Radial Expansion (PRE), is also described as the most likely mechanism for ejection of X-ray burst nuclear ashes into the stellar surrounding.

2.2.1 X-ray binaries

An X-ray binary system is one in which a collapsed star (a neutron star, or black hole) orbits a normal star so closely that matter falls from the normal star onto the compact stellar object, is heated, and emits X-rays. The amount of gravitational energy converted to X-rays is such that these systems are among the brightest extra-solar objects in the sky. The matter accretion can occur in two ways. In the *Roche lobe overflow* case (see Fig.2.1(a)), the donor normal star primary expands to fill its Roche lobe, and material flows through the gravitational potential saddle point between the two stars. This material will possess too much angular momentum to fall directly on the compact star, and will form an accretion disk instead. In the *stellar wind* case (see Fig.2.1(b)), the primary star's luminosity exceeds the Eddington limit, matter is lost via a stellar wind, and a small fraction (0.1%) of

Table 2.1: Known and predicted isomers in the ^{100}Sn region

Nucleus	J^π	Configuration	Decay mode	Ref.
^{94}Pd	14^+	$\pi g_{9/2}^{-4}\ \nu g_{9/2}^{-2}$	γ(E2)	ex
	19^-	$\pi g_{9/2}^{-4}\ \nu g_{9/2}^{-2}$	γ(E3)	
^{95}Pd	$21/2^+$	$\pi g_{9/2}^{-4}\ \nu g_{9/2}^{-1}$	$\beta\gamma$, $\beta p\gamma$, γ(E4)	
	$1/2^-$	$\pi p_{1/2}^{-1}$	γ(M4)	
^{96}Pd	8^+	$\pi g_{9/2}^{-4}$	γ(E2)	
	(15^+)	$\pi g_{9/2}^{-4}\ \nu g_{9/2}^{-1} d_{5/2}$	γ(E2)	
^{94}Ag	21^+	$\pi g_{9/2}^{-3}\ \nu g_{9/2}^{-3}$	$\beta\gamma$	
	7^+	$\pi g_{9/2}^{-2}\ \nu g_{9/2}^{-1}$	$\beta\gamma$, $\beta p\gamma$	
^{95}Ag	$23/2^+$	$\pi g_{9/2}^{-2}\ \nu g_{9/2}^{-2}$	γ(E2)	
	$(37/2^+)$	$\pi g_{9/2}^{-3}\ \nu g_{9/2}^{-2}$	γ(E2)	
	$1/2^-$	$\pi p_{1/2}^{-1}$	γ(M4)	
^{96}Ag	2^+	$\pi g_{9/2}^{-1}\ \nu g_{9/2}^{-1}$	$\beta\gamma$, $\beta p\gamma$, γ(E6)	
	19^+	$\pi g_{9/2}^{-2}\ \nu g_{9/2}^{-1}$	$\beta\gamma$, $\beta p\gamma$, γ(E2)	
	15^+	$\pi g_{9/2}^{-2}\ \nu g_{9/2}^{-1}$	γ(E2)	
	13^-	$\pi g_{9/2}^{-1}\ \nu g_{9/2}^{-1}$	γ(E3), γ(M2)	
^{96}Cd	16^+	$\pi g_{9/2}^{-2}\ \nu g_{9/2}^{-2}$	$\beta\gamma$, $\beta p\gamma$	
^{97}Cd	$25/2^+$	$\pi g_{9/2}^{-2}\ \nu g_{9/2}^{-1}$	$\beta\gamma$, $\beta p\gamma$	
	$1/2^-$	$\pi p_{1/2}^{-1}$	γ(M4)	
^{98}Cd	(12^+)	$\pi g_{9/2}^{-2}\ \nu g_{9/2}^{-1} d_{5/2}$	γ(E2)	
	8^+	$\pi g_{9/2}^{-2}$	γ(E4)	
^{98}In	9^+	$\pi g_{9/2}^{-1}\ \nu g_{9/2}^{-1}$	$\beta\gamma$, $\beta p\gamma$, γ (E9)	
	4^-	$\pi p_{1/2}^{-1}\ \nu g_{9/2}^{-1}$	γ(E3), γ(M2)	
^{99}In	$1/2^-$	$\pi p_{1/2}^{-1}$	γ(M4)	sm
	$(17/2^+)$	$\pi g_{9/2}^{-4}\ \nu g_{9/2}^{-1} d_{5/2}$	γ(E4)	sm
^{100}Sn	6^+	$\pi g_{9/2}^{-n}\ \nu\ (d_{5/2},\ g_{7/2})^n$	γ(E2)	sm

the plasma ejected is captured by the compact companion an obstacle to the wind stream. In this case, material may have not enough angular momentum to form an accretion disk, and accretion is more or less spherical. The latter case is relevant probably only for massive donor stars. A major difference between the two accreting mechanisms is the different mass accretion rate: $3\times10^{-4} - 3\times10^{-8}M_{\odot}yr^{-1}$ in the first case, and $10^{-7} - 3\times10^{-6}M_{\odot}yr^{-1}$ in the second.

2.2.2 Observations of type I X-ray bursts

X-ray bursts are thermonuclear flashes on the surface of a neutron star which is accreting material from a low mass companion. These are periodic (hours to days) rapid increases in luminosity (1−10 sec) peaked in the X-ray range of the electromagnetic spectrum with a duration of 10−100 sec. The peak luminosity of a typical burst is of the order of 10^5 times the Sun's luminosity. The rapid increase of luminosity indicates an explosive event, while the spectral softening during the subsequent luminosity decrease is a property of the black body radiation related to the cooling of the neutron star photosphere. The burst energetics is characterized by an integrated flux of about typically 10^{39}–10^{40} erg/s, on top of the more persistent accretion-powered luminosity of the order 10^{37} erg/s for accretion onto a neutron star. There is a variety of burst profiles (see for example Fig.2.2) depending on the particular source, and sometimes even bursts from the same source show different profiles. The recurrence pattern of X-ray bursts may be extremely regular (see. Fig.2.3). In this case, seven X-ray bursts were observed in 20 hours of observation, with recurrence time of about 193 min, with scatter of only ±3 min [55]. Most X-ray bursting systems, however, show irregular behavior.

Observations at optical wavelengths have also been carried out, reveling the existence of simultaneous optical/X-ray bursts [56, 57]. The optical fluence was

orders of magnitude higher than the expected optical emission form black-body X-ray bursts. Also, these optical bursts appear to be delayed by a few seconds relative to the X-ray burst. These observations indicate that optical emission form X-ray sources is due reprocessing of the X-ray burst in material within a few light

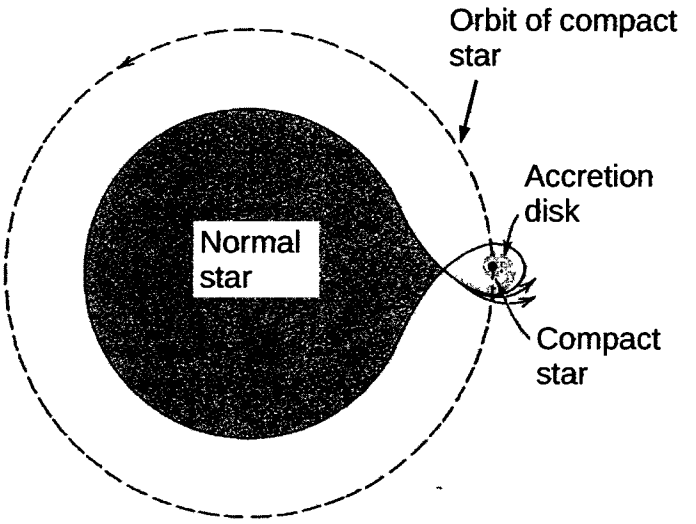

(a) accretion by Roche overflow

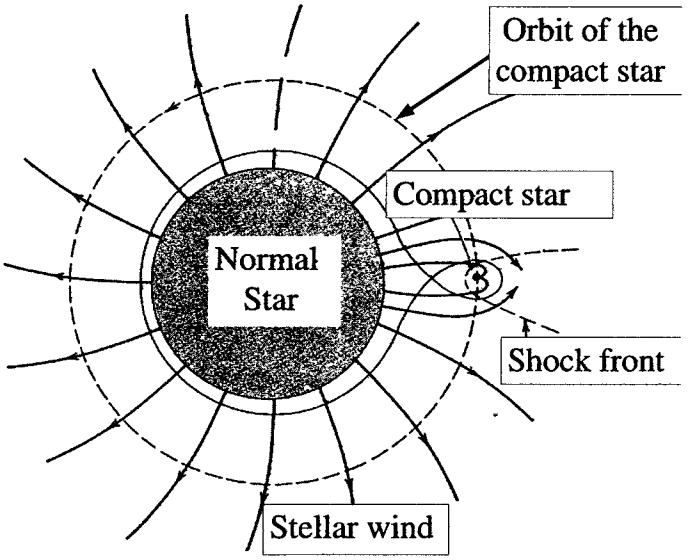

(b) accretion by Star Wind

Figure 2.1: Two possible gas accretion mechanisms on the surface of the neutron star.

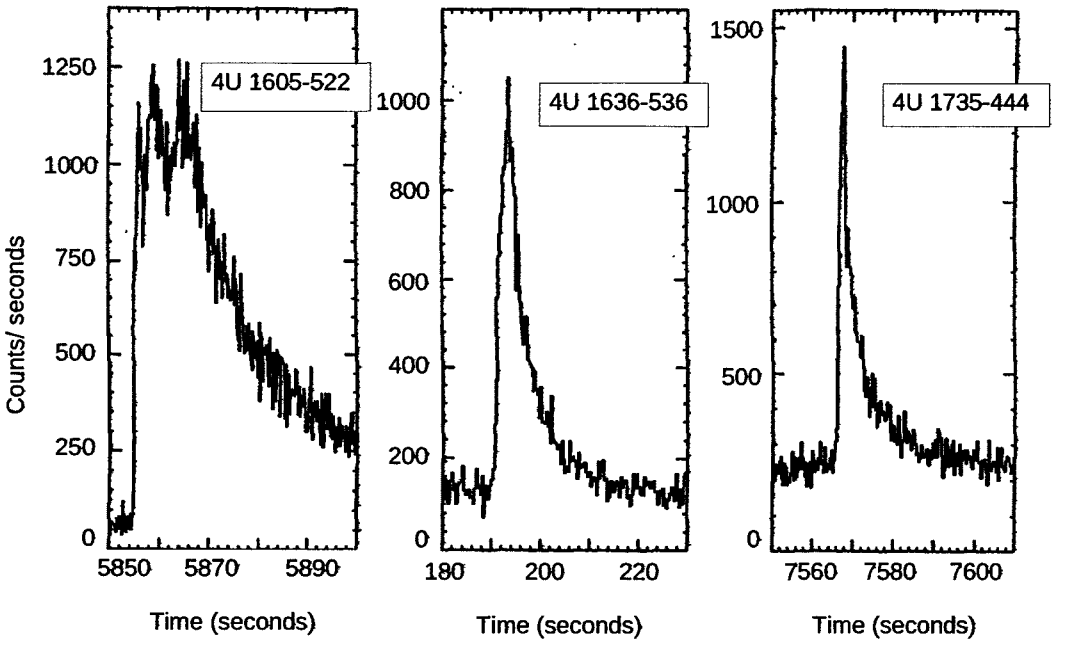

Figure 2.2: Examples of three different X-ray burst profiles observed with EXOSAT in the 1-20 keV energy band.

seconds from the X-ray burster [58]. Possible sites for optical emission are the accretion disk and the hemisphere of the normal companion facing the neutron star. In this sense, the X-ray burst can be considered a probe of the neutron star surrounding. With a detailed analysis of optical bursts it has been possible for instance to put limits on the size of the accretion disk [59].

The history of infrared and radio observations of X-ray bursts is more controversial, as different groups observing the same systems have reported opposite conclusions [60]. Based on the most recent radio and infrared survey, [61] concluded that previous radio observation are unlikely to be real and infrared are also highly questionable.

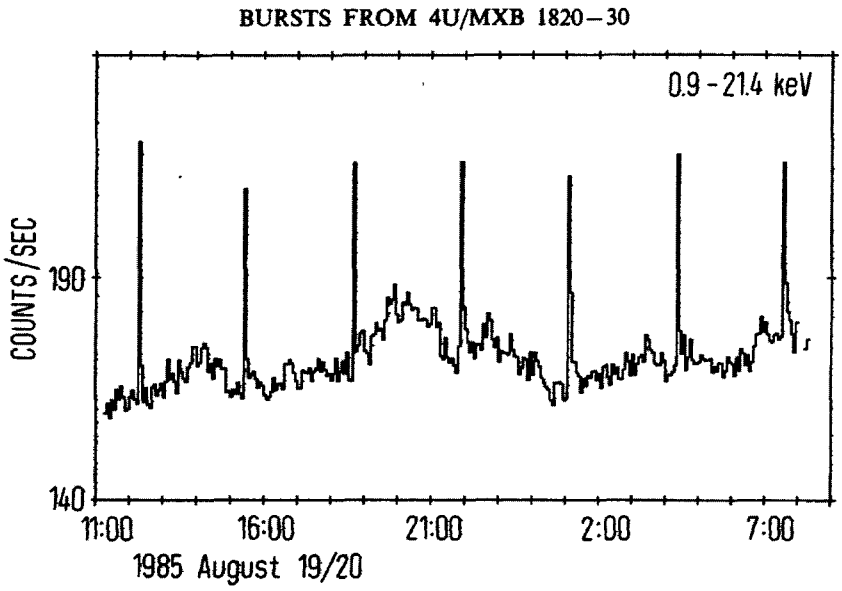

Figure 2.3: 0.9-21.4 keV light curve of the star 4U/MXB 1820-30 for the whole observation of 20 hours with 7 spikes corresponding to 7 X-ray bursts. Bursts are spaced of 193±3 min.

2.2.3 Nuclear processes in accreating layer of a neutron stars

Depending on the density, composition, and temperature of the material accreted on the surface of a neutron star, several burning scenarios are possible. Typically, Hydrogen and Helium burning would be ignited first via the 3α-process and the CNO cycle. The burning can be stable or can ignite a thermonuclear runaway that lead to an X-ray burst. This section is a summary of different scenarios and conditions for processing of accreted material.

Hydrogen burning

Hydrogen burning at low temperature ($T \leq 10^6$K) is ignited at density of about $1.4\times\ 10^7$ gr/cm^3 and proceeds via the pp-chain. The energy generation is limited

by the reaction p(p,$e^+\nu$)^{2}H which is allowed by the weak interaction. The energy generation rate is hence low, and not very temperature sensitive ($\propto T^4$) and so the burning remains stable. This regime is, however, not very important because the temperature exceeds 10^7K in most of the accreting atmosphere. At higher temperature ($T \geq 10^7$K), the CNO cycle is ignited and the energy generation is faster and highly temperature sensitive ($\propto T^{16}$). In this phase hydrogen burning is thermally unstable and it may trigger an X-ray burst. This condition is verified if for accretion rate $\dot{m}$ <900 gr/cm^{-2}s^{-1}. At even higher temperatures of about T$\sim 10^8$K the energy generated by the CNO (hot CNO) is limited by the β-decay of ^{14}O and ^{15}O and it is no longer temperature dependent. This eventually stabilizes the burning. However, the energy generated in this process is crucial for the burst because it heats the accreted material to temperature that are sufficient to ignite the Helium burning.

Helium burning

The material accreted on the surface of a neutron star can be very helium-rich if, for example, the donor star is evolving from its main sequence to a helium star or a white dwarf. A Helium-rich layer would also result from stable burning of Hydrogen layers. In contrast to hydrogen burning, Helium burning is not governed by weak interactions and so it can became unstable. Helium burning is ignited via the 3α reaction. At high densities and temperatures below the Debye temperature ($T_D = 10^8(\rho/10^9)^{(1/2)}K$), helium nuclei are bound in a lattice structure and fusion happens in the pycnonuclear regime with the main contribution coming from slowly moving nuclei. In this regime reactions happen at a rate $\propto$exp(-C $\rho^{-1/6}$) that is density but not temperature dependent and thus the burning is stable. On the other hand, low densities and high temperatures (T>TD), the burning happens

in thermonuclear regime and with the rate that is highly temperature sensitive ($\approx T^{30}$). In this regime the burning is likely to be thermally unstable. At even higher temperatures ($T\sim10^9$), 3α reaction rate saturates and the reactions $^{12}C(\alpha,\gamma)^{16}O(\alpha,\gamma)^{20}Ne(\alpha,\gamma)^{24}Mg(\alpha,\gamma)^{28}Si$ etc. are the primary source of energy. The build up of heavier elements, however, is limited by the helium abundance and the pressure at the moment on which the instability is quenched by the expansion of the layer.

Hydrogen-Helium combined burning: the rp-process

One unique feature of accreating compact objects like neutron stars, is that Helium burning can happen in the presence of Hydrogen in contrast to Helium burning in a normal star.

Under typical conditions, the envelope of a neutron star can reach temperatures of about 5×10^8 K at which the HCNO-cycles breaks out via the reactions $^{14}O(\alpha,p)$ and $^{15}O(\alpha,\gamma)$. Material leaks out of the HCNO cycle, and a series of alpha and proton capture reactions (αp-process), rapidly convert $^{14,15}O$ into heavier elements all the way up to the Sc region (αp-process). At this point (α ,p) reactions start to be inhibited by the Coulomb barrier and a series of proton captures and subsequent β-decays drive material up to ^{56}Ni. The rp-process up to this point is illustrated in Figure 2.4. The nucleus of ^{56}Ni has a remarkable role in the rp-process: despite bifurcations due to the competition between p-capture,β-decay, and (α,p) reactions, all the flows converge to this nucleus and tend to stagnate there. This is because although the β-decay of ^{56}Ni is energetically possible ($Q_{\beta+}$=1113.5 keV), it is forbidden by selection rules and the decay via electron capture has a half-life of about 6 days in the laboratory (but it is even longer in astrophysical environment due to ionization). Proton capture is strongly suppressed by photodisintegration

($Q_{p,\gamma}$=694 keV), so the effective half-life is strongly temperature dependent. Single zone models predict that by the time the flow reaches ^{56}Ni, the temperatures is as high as 1.5×10^9 K, and the corresponding effective half-life of ^{56}Ni becomes about $\approx$100 s. Other models, however, predict lower temperatures, making ^{56}Ni a less pronounced bottleneck.

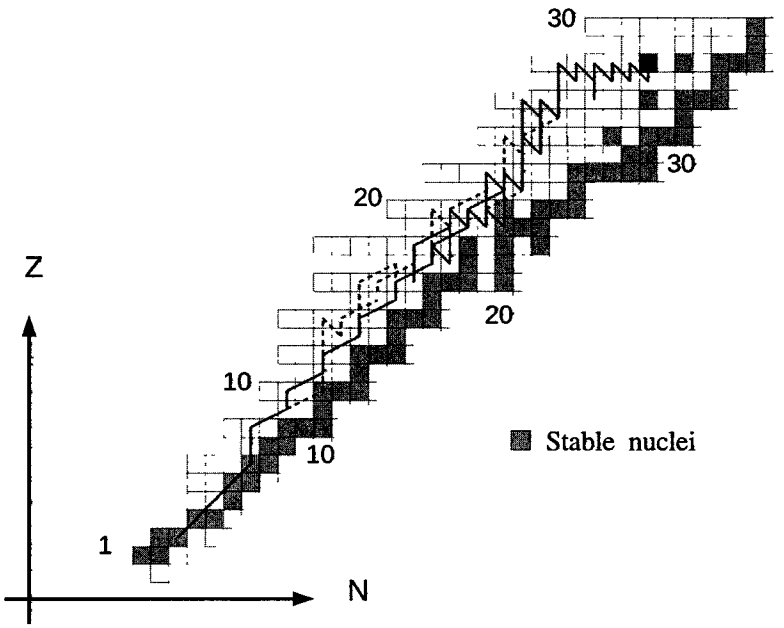

Figure 2.4: The dominant nuclear reaction flow during the early stage of the thermonuclear runaway in a H- and He-rich fuel layer on an accreting neutron star.

At this point most of the helium has been burned and converted into ^{56}Ni, and the energy generation rate drops rapidly. The energy generation drop causes, in turn, a temperature drop and a density increase. under these conditions, the effective half-life of ^{56}Ni decreases to fraction of second, allowing the rp-process to proceed beyond ^{56}Ni. A series of proton captures and β-decays drives the matter toward heavier nuclei and this slow burning is responsible for a tail in the energy generation.

X-ray bursts duration is limited mostly by the initial Hydrogen abundance, and bursts lasting as long as 100 s have been observed [62].

The rp-process end-point is limited not only by the initial Hydrogen abundance. Calculations [63] show that long lasting bursts can reach ^{99}Sn and then proceed along the Sn isotopic chain toward stability. Proton captures, not possible on isotopes $^{99-104}$Sn became allowed on ^{105,106}Sn. Most of the flux then proceed through a p-capture producing 105Te that is α-unbound, while causes the material to fall back on ^{103}Sn (see Fig.2.5). A small fraction of the flow also reaches 106Sn and a similar cycle ending in 104Sn takes place. Because isotopes $^{106-109}$Te are all known to be α emitters, the existance of the Sn-Sb-Te cycles is not under question. However, the uncertainties in the proton separation energies affects the relative strength of the Sn-Sb-Te subcycles.

Calculations with different ignition conditions confirm that the rp-process cannot proceed beyond A$\approx$107. A pulsed rp-process, where a burst ignites the ashes of a previous burst, could in principle bypass the region. However, this would require some unburned hydrogen mixed with ashes which is typically not found in long bursts.

2.2.4 Heating in accreting neutron star crust

The neutron star crust is a layer about 1 km thick below the neutron star atmosphere formed by the accreted Hydrogen and Helium. The density of the crust ranges (top to bottom) from 10^4 to 10^{14} g/cm^3 and consists of a layer of nuclei and degenerate electrons (outer crust).

The extreme density and ongoing accretion drive electron captures and pycnonuclear reactions. The latter are fusion reactions of nuclei at low energy due to quantum tunneling owing to the zero point motion of nuclei in a very dense

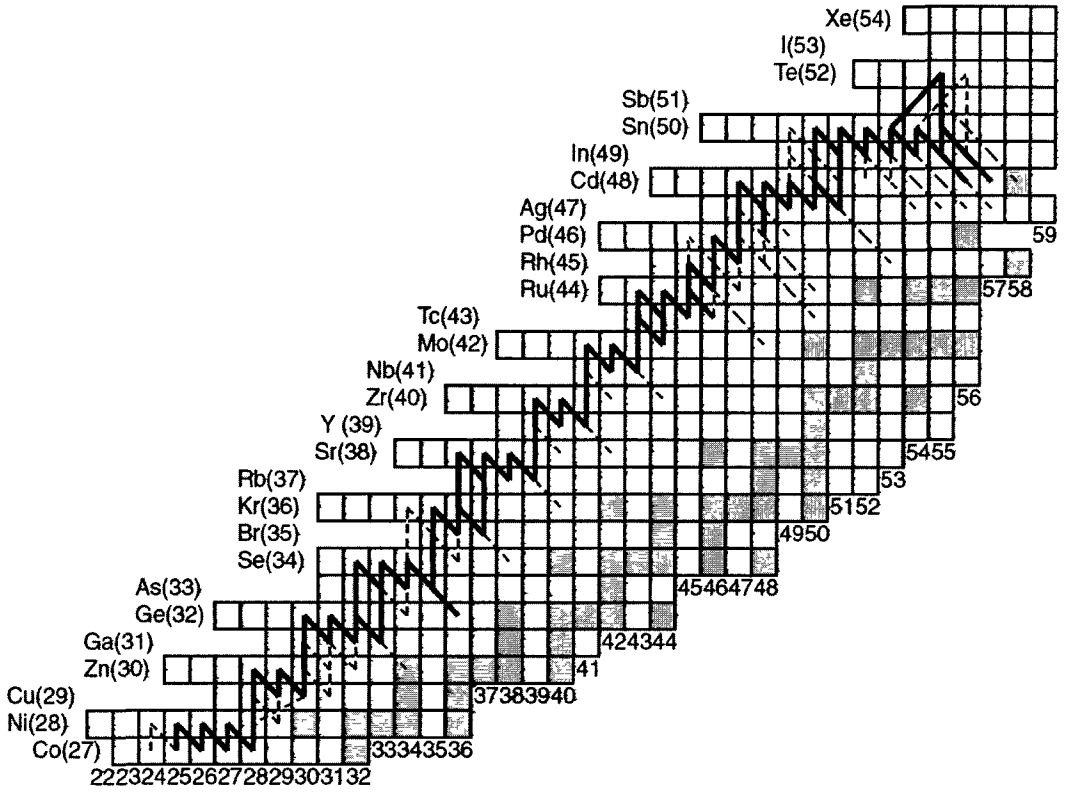

Figure 2.5: Nuclear reaction flow during the rp-process beyond ^{56}Ni. This flow occurs in the slow energy generation phase, responsible for the tail of particularly long the X-ray Bursts.

lattice. All these processes are probable sources of heat in the crust. Such heat sources are important to understand for example the decay curve of the observed luminosity of transiently accreting neutron star. These are neutron stars that have been observed to exhibit alternating periods of accretion (outburst) and periods when the accretion is shut down. The decay curve of the luminosity can probe the internal of the neutron star.

A recent study [16] modeled the electron capture processes in the neutron star crust and it revised previous calculations that only considered electron capture on

the ground state realizing that the amount of heat deposited in the crust from the deexcitation of higher states can be significant. The energy generated by electron capture reactions depends on the structure of the nuclei that capture the electron. This introduces a dependency of the heat deposited in the crust on its detailed composition set by the ashes of the X-ray bursts that gravity rapidly incorporate in the neutron start crust. In order to accurately calculate this composition, quantities like half-lives and bp-emission branching ratios along the path of the rp-process are needed.

2.2.5 Light p-nuclei ^{92,94}Mo, ^{96,98}Ru and photospheric radius expansion type I X-rays burst

Most of the stable nuclei heavier than iron are believed to be produced by neutron capture reactions: a) the slow (s-) neutron capture process occurring mainly in low-mass asymptotic giant branch stars and massive red giant stars, and b) the rapid (r-) capture process which might occur in Type-II supernovae. There are, however, 35 nuclei between ^{74}Se and ^{196}Hg that are shielded from production by neutron capture processes by their more neutron rich β-stable isobars. These nuclei are called p-nuclei and their origin is attributed to the γ-process, i.e. to the photodisintegration (γ,p), (p,γ), and (γ,n) reactions of nuclei previously synthesized by the s- and r-process. The proposed sites for the γ-process to happens is the front shock in type-II supernovae, or the deflagration flame in type-I supernova detonations. These models reproduce the abundance of p-nuclei in the solar system within a factor of 3 with the exception of the light p-nuclei ^{92,94}Mo and ^{96,98}Ru that are under-produced by factors of 10-100. The underproduction of these nuclei is an outstanding problem in nuclear astrophysics. The rp-process could offer a

possible solution to this puzzling case because there are some X-ray bursts that can produce light p-nuclei. However, the estimated number of these bursts is not sufficiently high, and it is also unclear whether material enriched in these nuclei can be ejected in X-ray bursts (see next sub-section).

The nucleosynthesis due to the X-ray burst would be relevant to the composition of universe, only if ashes resulting from the nuclear burning could escape from the extreme gravity of the neutron star. A possible mechanism for ejection of material was studied in [64] where it was concluded that there are X-ray bursts capable of generating a stellar wind that could eject up to 1% of the accreating material. When the luminosity of an X-ray burst exceeds the Eddington limit, the excess energy goes into expanding the atmospheric layer of the neutron star rather than emission of radiation. This layer can expand to a region of low pressure for which a fraction of the atmosphere, that also contains nuclear burning ashes, is blown away. These bursts are called radius expansion (RE) bursts, and they have very specific observational features such as a significant increase of the black-body radius with an associated decrease in temperature, and a variation of the bolometrix flux (check this!!!).

The observed PRE X-ray burst profile often shows a double peaked energy dependent structure (see for example the left panel of Fig.2.2 from the star 1608-522) that is explained as due to X-rays radiated before reaching the Eddington limit (first peak) and radiated after the luminosity has decreased below such a limit. However, not all the double peaked burst are RE, with some reflecting a real energy generation irregularity. The rising time of these PRE burst is also a distinctive feature, being particularly short $\sim$1 sec.

The ejection of heavy ashes and hence of light p-nuclei present however some complications. In order to produce p-nuclei the accreted material has to be H-

rich, while most PRE bursts, especially the ones that develop extended convective zones that transport ashes to the surface, occur with He-rich accreting material. On the other hand, the ejection of ashes during a RE burst, produced in a previous non RE burst can be difficult because these ashes might likely have been already incorporated in the crust by gravity, and hence lie in a layer deeper than the ignition of the new burst. Recently however [65], some evidence for heavy-element ashes in the photosphere of a neutron star have been collected during a more extreme case than the one described above, so called photospheric superexpansion burst. In these cases (estimate no more than few tenth of the bursts) the luminosity decreases to less than 1% of the peak value, and the radius expansion factor is of 100 or more.

Chapter 3

Experiment

3.1 Introduction

The experiment to study the β-delayed proton emission of neutron deficient isotopes around ^{100}Sn was run at the National Superconducting Cyclotron Laboratory (NSCL), at Michigan State University, as NSCL experiment number 07034.

3.2 Experiment overview

Rare nuclides are produced at NSCL using the in-flight fragmentation technique. A primary beam of heavy nuclei collides with a target and undergoes fragmentation. The fragments of interest are selected, while nuclei of the unreacting primary beam and the unwanted fragments are filtered out by the fragment separator A1900 and by the RFFS fragment separator. In our experiment, the resulting secondary beam of mixed fragments was delivered to the experimental area where they were identified and stopped in a stack of silicon detectors surrounded by an array of germanium detectors. This detector setup allowed to detect the implantations and

their subsequent emission of positrons, protons, and photons.

3.3 Experimental setup

3.3.1 Fragment production

The neutron deficient nucleus ^{100}Sn and its neighbors were produced by fragmentation of a 120MeV/u ^{112}Sn beam in a 195mg/cm^2 ^{9}Be target. The primary beam was produced in the NSCL Coupled Cyclotrons at an average intensity of 10.7 pnA. The cross section measurements for the production of the N=Z nuclei ^{100}Sn, ^{98}In and ^{96}Cd, and the N=Z+1 nuclei, ^{99}In and ^{97}Cd, are reported in [66], along with a comparison to the EPAX predictions. [66] also gives a brief review of the production cross section of ^{100}Sn in previous experiments.

3.3.2 Fragment separation and identification

A1900 fragment separator

The A1900 is the projectile fragment separator used at the NSCL to separate reaction products using a combination of magnetic rigidity and energy loss selection known as the Bρ-δE-Bρ technique [67] (a schematic diagram of A1900 is shown in Figure 3.1). Bρ is the magnetic rigidity, defined as:

$$B\rho = \frac{mv}{q} \tag{3.1}$$

where ρ is the radius of curvature of the particle traveling though the magnetic field of strength B; and m, v, and q are the mass, velocity and charge of a particular nucleus that travels through the separator, respectively.

Nuclei produced in the fragmentation process have different Bρ because they have different mass to charge ratio m/q, and similar velocities [68] (the velocity similar to the ^{112}Sn primary beam, somewhat reduced and broadened by energy loss effects and reaction kinematics). During the first step of separation –between the production target and image 2 of the A1900–the beam is dispersed by two dipole magnets ($B\rho_{1,2}$ = 2.8802 Tm). A set of slits, limiting the momentum acceptance of the separator (dp/p) to 1%, stopped most of the unwanted particles. A larger value of dp/p would not have allowed a mass separation by time-of-flight measurement without tracking the transverse position of the beam (momentum tracking[1]), which was not possible because the intensity of the secondary beam at the dispersive focal plane was too high (larger than 2 MHz). These rates would have damaged the plastic scintillator that was available for the momentum tracking.

Ions with the selected Bρ, pass through an energy degrading wedge emerging with different momenta depending on the nuclear charge Z and hence with a different Bρ for different Z. The degrader material was a 40.6 mg/cm^2 thick Kapton and was wedge-shaped to keep the achromatic condition for the isotopes of interest.

The second stage of the A1900 (set to $B\rho_{3,4}$=2.7710 Tm) remove the dispersion produced in the first stage and, given the effect of the wedge, also provide isotopic selection.

Identification of particles during this phase was performed in flight at the A1900 focal plane using the standard A1900 detector setup for particle identification: silicon PIN detectors for energy loss measurement, a plastic scintillator for time-of-flight measurement (TOF), and a HPGe for γ-rays detection. Fragments were

[1]As it will be explained in Section 3.3.2 the time-of-flight (momentum) of particle along the beam line identifies the ratio m/q. If dp/p were larger than 1%, the time resolution would not have been good enough for a proper identification. In this case, a measurement of the momentum was necessary to improve the time-of-flight resolution

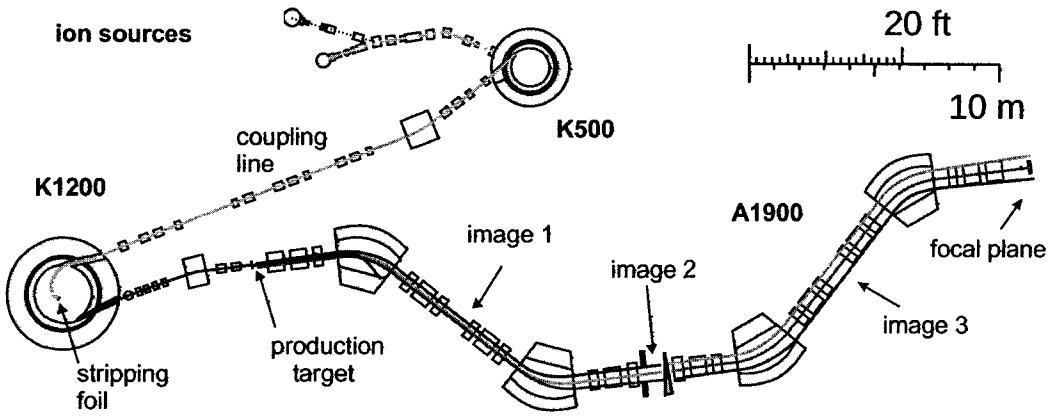

Figure 3.1: A schematic diagram of the coupled cyclotron facility and the A1900 fragment separator.

stopped in a stack of silicon PIN detectors and identified based on their location on a ΔE vs. TOF plot (see Section) relative to the nuclei microsecond isomers ^{90}Mo, ^{93}Ru, and ^{96}Pd that were unambiguously identified though their characteristic γ-decay [69].

The settings chosen for the production of ^{100}Sn were obtained by scaling magnetic rigidity settings that were observed to maximize the production rate of the fragments $^{101-104}$Sn during Bρ scanning. The $^{101-104}$Sn settings are reported in Table 3.1.

Table 3.1: Bρ settings for the A1900 during the Bρ scanning phase with a 376 mg/cm^2 target. Notice that the actual Bρ settings used during the experiment and reported in the text are different because of the 188 mg/cm^2 used for those runs.

Centered Fragment	B$\rho_{1,2}$	B$\rho_{3,4}$
^{104}Sn	2.46890	2.35270
^{103}Sn	2.43700	2.31870
^{102}Sn	2.40480	2.28440
^{101}Sn	2.37310	2.25050
^{100}Sn	2.35510	2.15450

Radio frequency fragment separator

The momentum distribution of nuclei produced by projectile fragmentation at intermediate-energy (50-200MeV/u) is asymmetric, with low momentum exponential tails corresponding to collisions in which a large fraction of the projectile's kinetic energy is dissipated in the target. In a magnetic separator like the A1900, the exotic neutron-deficient nuclei are found at low magnetic rigidity, along with the tails of more stable fragments. Therefore, the magnetic rigidity selection obtained in the A1900 fragment separator was not sufficient to perform a decay spectroscopy experiment in this region. This situation is illustrated in Figure 3.2, which shows the simulated $B\rho$ distribution of the main nuclei produced in this experiment, using the code LISE++ [70]. Additional beam purification was then needed.

At the NSCL this further stage of purification is based on the velocity selection of the fragments and is achieved by means of the Radio Frequency Fragment Separator (RFFS) [11], located 52 m downstream from the production target (see Figure. 3.3).

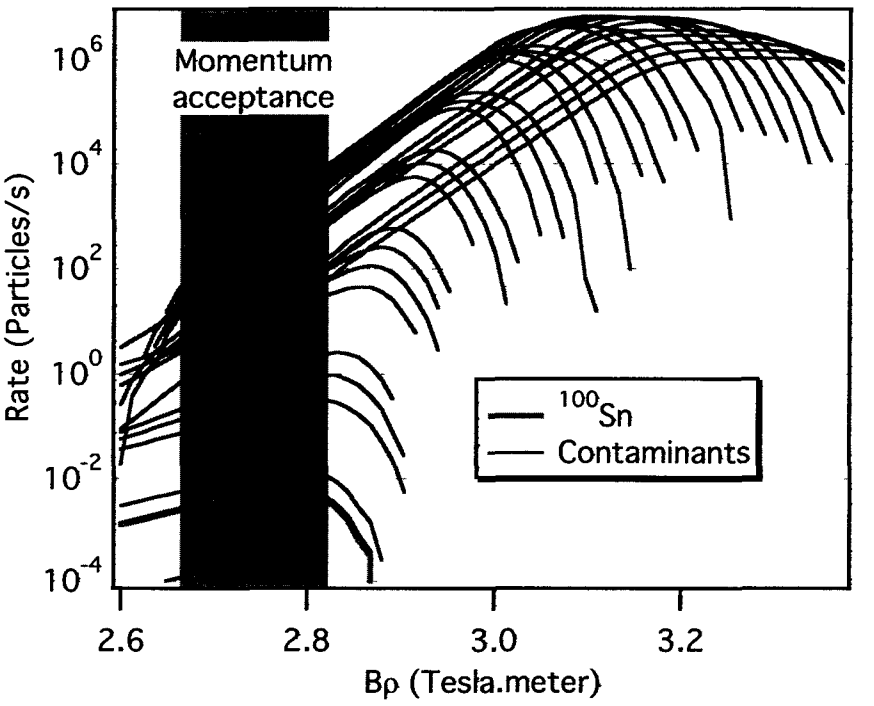

Figure 3.2: Simulation of the yield as a function of magnetic rigidity for ^{100}Sn and the principal contaminants produced in this experiment.

The RFFS applies a sinusoidal electric field transversely to the direction of the beam, synchronized with the K1200 cyclotron frequency, which for this specific experiment was 21.815 MHz. Different nuclei are produced in a single beam bunch in phase with each other, but arrive at the RFFS with different phases due to their different velocities. They therefore encounter different electric fields in the RFFS, resulting in different vertical deflections. Particles can then be selected based on their deflection (corresponding to their velocity) by a set of vertical slits placed 6 m downstream from the device. Figure 3.4 shows the effect of this selection. The vertical position of the fragments is monitored by two retractable parallel-plane avalanche counters (PPAC) placed along the beam line, one upstream of the slit and one downstream. Particles were identified in this stage using the same techniques as at the focal plane of A1900. After separation, the nuclei of interest

were transported to the experimental area.

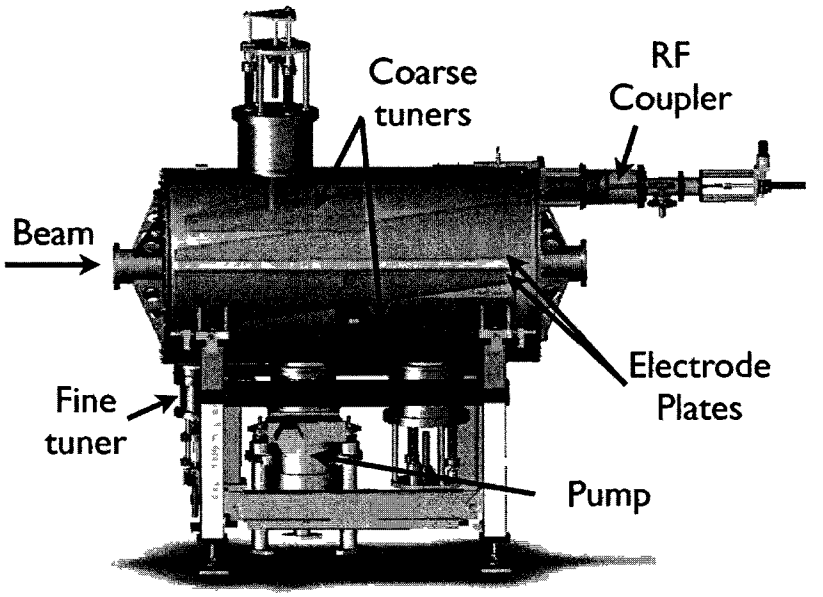

(a)

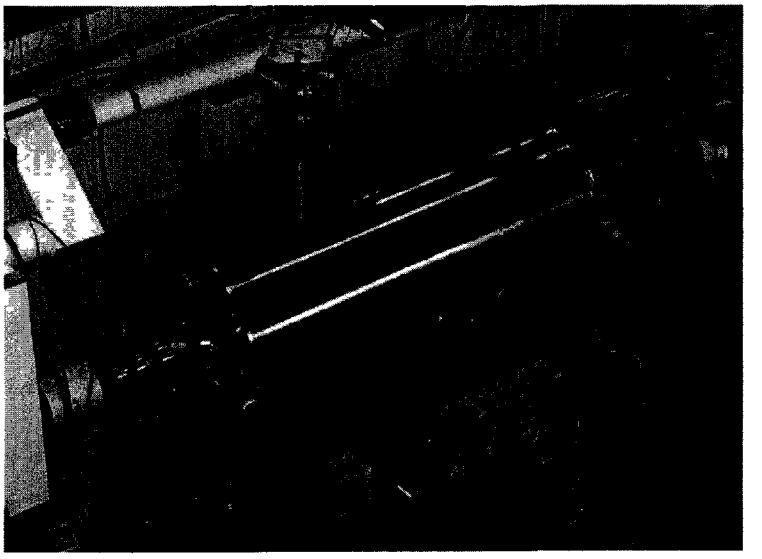

(b)

Figure 3.3: a) Schematic diagram of the RFFS and b)Photography of the RFFS. Beam comes from the left.

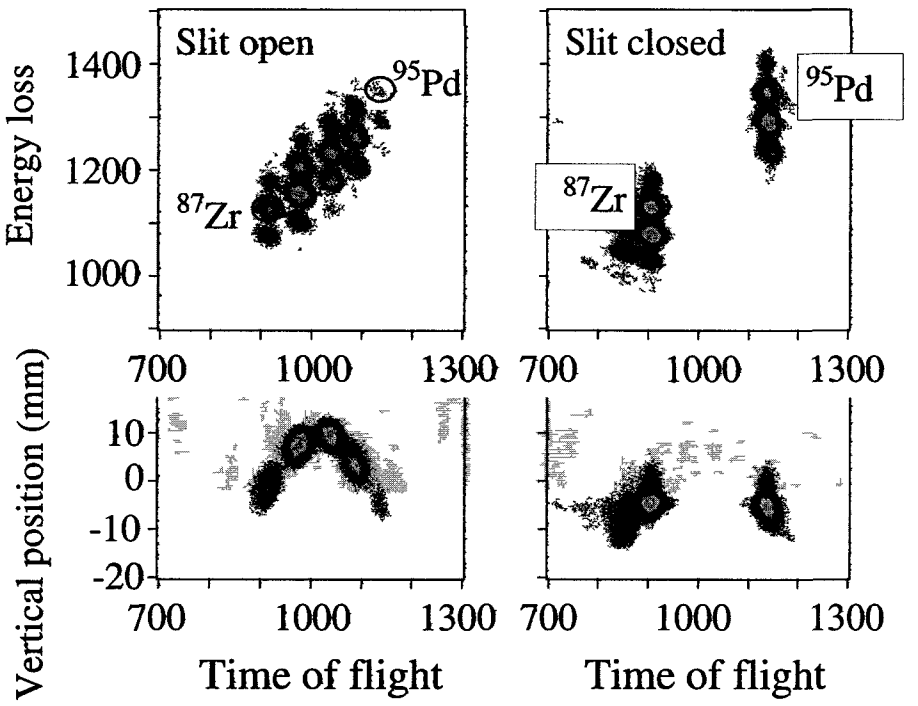

Figure 3.4: Identification plot (above, energy loss vs. time-of-flight) and vertical deflection (below) as a function of time-of-flight before the RFFS slits (left) and after (right). The left and right plots are not normalized to the same number of incoming primary beam particles (the identification plot is explained in Section 3.3.2).

Different nuclei passing through a layer of a given material lose different amounts of energy depending on their nuclear charge. According to the Bethe formula:

$$-\frac{dE}{dx} = \frac{4\pi e^2 Z^2}{m_e v^2 A} \rho N_A \, z \left[\ln\left(\frac{2m_e c^2 \beta^2}{I(1-\beta^2)} \right) - \beta^2 \right] \tag{3.2}$$

where v and Z are the velocity and atomic number of the projectile; ρ, A, z are the mass density, atomic weight, and atomic number of the material, respectively. Thus, for a given velocity, the energy loss uniquely identifies the atomic number Z.

The time of flight is essentially a measurement of the nuclear mass to charge ratio m/q. Particles selected by the A1900 have a specific Bρ, and hence, the time of flight is proportional to the mass to charge ratio,

$$tof = \frac{L}{v} = \frac{L}{c} \sqrt{1 + \left(\frac{mc}{qB\rho} \right)^2} \tag{3.3}$$

where L is the particles path length. In the present experiment, the energy loss was measured with PIN detectors upstream of the DSSD (see Sec. 3.3.3). The time of flight was measured in two ways: (i) as time difference between a start signal provided by PIN1 and a stop signal provided by the cyclotron RF, and (ii) as time difference between PIN1 and a plastic scintillator located in the A1900 focal plane (XFP-scintillator).

3.3.3 Experimental station

Beta counting system

Identified fragments were implanted in a double-sided-strip detector (DSSD) that was the central detector of the β counting system (BCS). The DSSD used in this experiment was a single Si crystal 985 μm thick and segmented into 40 1-mm strips in both the x and y dimension, for a total of 1600 virtual pixels. To realize the condition of minimum implantation rate per pixel (minimum background), the beam was defocused over the surface of the DSSD. Three PIN detectors located upstream of the DSSD were used to degrade the beam. They also provided beam diagnostics, energy loss information for particle identification, and the time signal (stop) used to measure the time-of-flight; the other time signal (start) came from a plastic scintillator, located at the A1900 focal plane (XFP scintillator). The DSSD was also used to detect the β- and the β-delayed particles emitted by the implanted species. Implantations and decays were correlated based on location and time, allowing the measurement of lifetimes and other decay properties, such as branching ratio and decay energies (these measurements are reported in detail in Section 5.1). Six single-sided silicon strip detectors (SSSD) and a planar Ge detector located downstream of the implantation detector constituted the β calorimeter, which allowed the measurement of the total energy of β-particles emitted in the downstream direction with energies up to 14 MeV. The calorimeter also vetoed the light particles whose energy in the DSSD is comparable to that of the β-particles.

Figure ?? shows a diagram of the DSSD electronics for the experiment. The electronic trigger is provided by both the implantation and the decay signals from the DSSD. Signals from each DSSD and SSSD strip were processed by dual gain

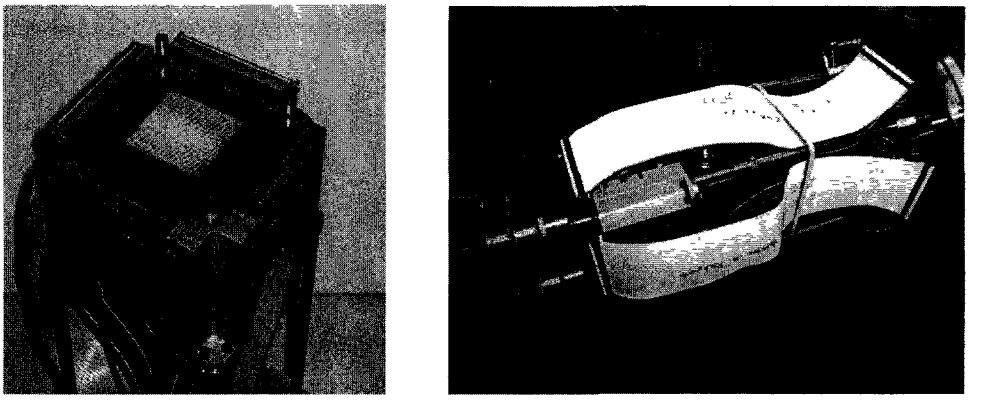

(a) (b)

Figure 3.5: (a) up-stream view of the DSSD with its downstream SSSDs. (b) view of the entire silicon stock including the three PIN detectors, and the Ge detector which is hold in place by the copper frame clearly distinguishable in the piture.

preamplifiers, with high and low gain defined on a scale of 100 MeV and 3 GeV, respectively. In either case, a coincidence between at least one strip in the front and one in the back is required to reduce high trigger rate that would be otherwise generated by random electronic noise. The low-gain signals were input to the analog-to-digital converters (ADCs) with no additional processing. The 80 high-gain signals (40-front strips and 40-back strips) were processed by six 16-channel shaper/discriminator modules. These modules (shaper function) amplified and time-shaped each input signal to improve the following ADC amplitude (energy) reading. One ADC was dedicated to read the 16 channels of output from each shaper module. The shaper/discriminator module also provided 16-logic signals triggered by any shaped-amplified output whose amplitude was above a set threshold (discriminator function). The logic OR of these output signals provided the master trigger of the β-decay events, and it was also recorded in a coincidence register module that provided a Boolean signal for the readout software, to determine which ADC had to be read. The ADCs were, in fact, the major contributors to the data acquisition dead time. The master live trigger was the logic AND of the mas-

ter trigger and the computer-NOT-busy signal. This trigger opened a 20 μs time gate during which the SeGA signals were recorded (see following Section 3.3.3), allowing for the measurement of prompt γ radiation, as well as β-delayed, and βp-delayed γ radiation.

Segmented germanium array

The high resolution segmented germanium array (SeGA) in its configuration for β-decay studies consists of 16 cylindrical Ge crystals, each of which is a single-crystal with 75% relative-efficiency germanium. Each crystal is electronically segmented in 81-cm disks, and each disk is similarly segmented in 4 quadrants, for 32 total segments. The segmentation provides improved position resolution to reduce the uncertainty in the Doppler correction necessary for in-beam experiments, and hence it is not needed in experiments with stopped beams, such as ours. those of the present work. Therefore, we used the logic-OR of the 32 segments as output signal.

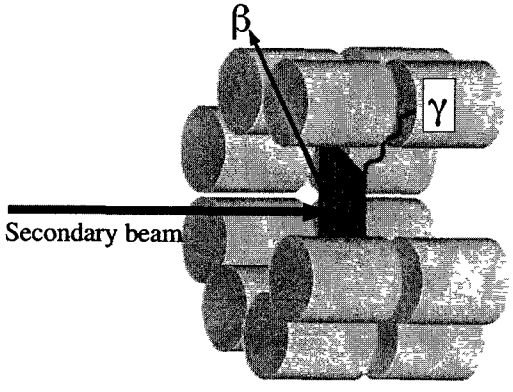

Figure 3.6: Schematic diagram of the detector setup. 16 germanium detectors of the SeGA array surrounding the DSSD.

As shown in Figure 3.6, the detectors were arranged in a two 8-detector rings, one upstream of the DSSD, and another downstream. The two rings were separated

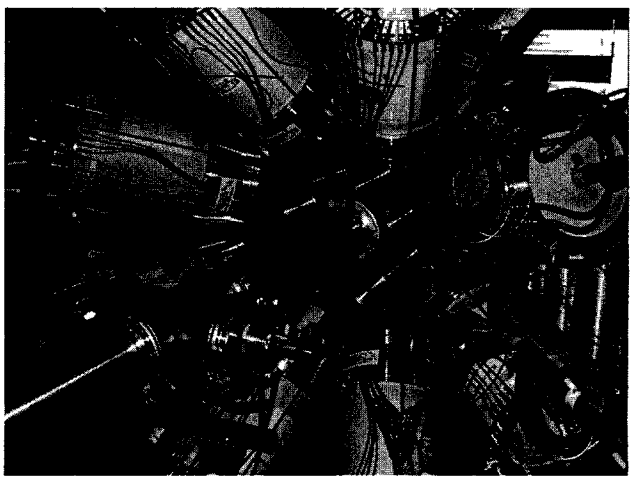

Figure 3.7: View of the Experimental setup. Eight detectors of the SeGA array upstream of the DSSD.

from each other by only a few mm. Figure 3.7 shows a photograph of the actual set up. Besides the main goal of γ-spectroscopy, SeGA also served to identify isomers used as reference in the PID.

Chapter 4

Data Analysis

This chapter is structured in four sections. Section 4.1 describes the analysis of the data for particle identification. Section 4.2 details the detectors' calibrations. Section 4.3.1 depicts the analysis of the β-delayed proton events. Section 4.4 describes the half-life and $P_{\beta p}$ measurements. Finally, Section 4.5 reports our unsuccessful attempt to perform measurements of β-decay end-point energies.

4.1 Particle Identification

Chapter 3 described how a beam containing a mix of wanted and unwanted exotic nuclear species was produced and transmitted to the experimental area, where it was stopped in a position sensitive silicon detector. The production of isotopically pure beams using projectile fragmentation is not feasible and not necessary. To perform β-decay studies each implanted nucleus arriving at the experiment has to be identified in its implantation location and arrival time. The particle identification (PID) turns the original disadvantage of beam impurity contamination into an advantage, because it allows one to study multiple species at the same time.

Each implanted nucleus is identified in-flight, based on the energy loss in set of beam-line detectors and on their measured time of flight as described in Section 3.3.3. The energy loss identifies the atomic number Z, and the time of flight identifies the mass to charge ratio (A/Q) when the momentum is sufficiently constrained. As the particles of interest in our experiment were fully stripped (this is the charge state we chose to transmit) this identifies A when Z is known.

This section describes the analysis of the energy loss and time of flight signals that was necessary to reach the best identification. Since the separation of nuclei is more difficult in heavy nuclei, this experiment required a special effort in order to achieve the necessary selectivity.

4.1.1 Energy loss signal

The implantation station was equipped with three PIN detectors a few centimeters upstream of the DSSD (see Section 3.3.3). Each PIN provided a redundant energy loss measurement. The particle identification plot (PID plot) obtained using the three PINs is shown in Figure 4.1. The best resolution was achieved using PIN1, while PIN2 and PIN3 showed a rather poor resolution. There was a problem with PIN3. The energy response from the PIN3 detector was found to be position dependent. This can be seen when mapping the response of PIN3 for a specific nuclear species as a function of implantation position measured with the DSSD. A correction factor was calculated for every DSSD pixel using the ratio of the average PIN3 response in that pixel to the average response over the entire DSSD. Figure 4.2 shows the correction factor for each pixel in the DSSD. The detector response to ions implanted in the center of the DSSD which are assumed to pass through the center of PIN3 showed a problem. The pattern of the correction factor suggests damage in that area of the detector, perhaps a failure to properly

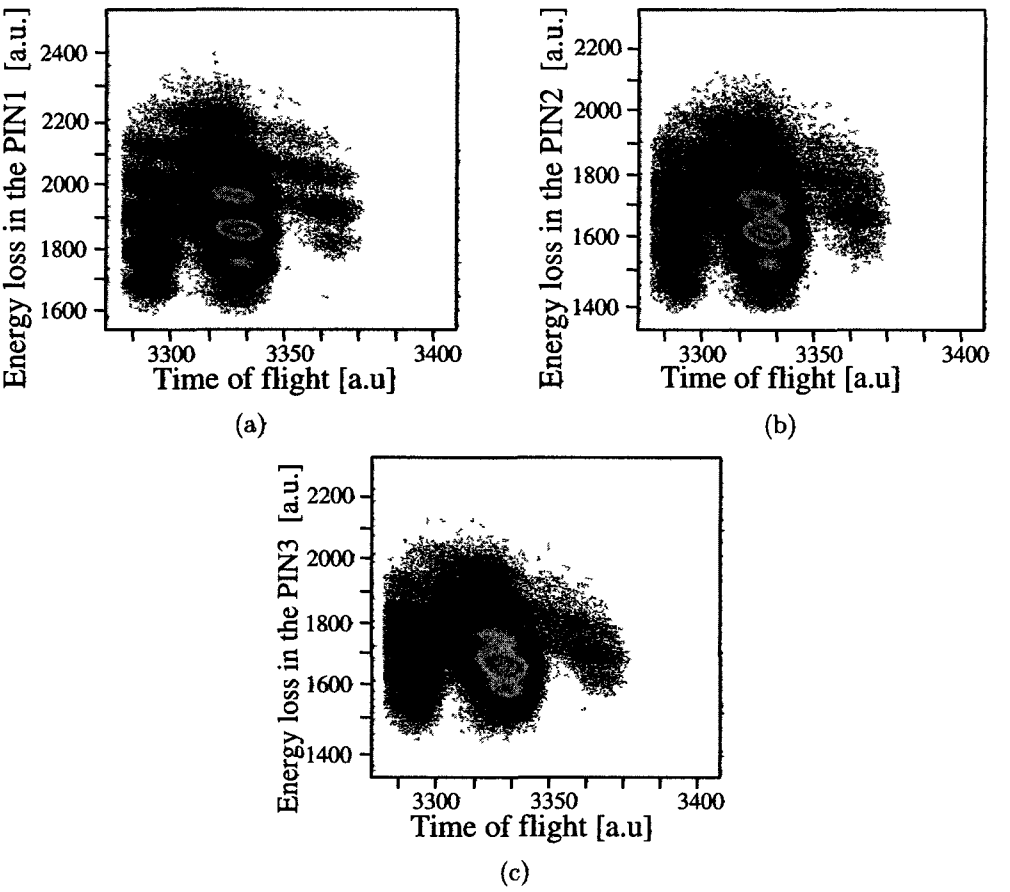

Figure 4.1: PID plots obtained using energy loss signals provided by PIN1 (panel a) PIN2 (panel b) and PIN3 (panel c).

collect charges (since the energy response was lower). The improvement of the resolution of the PID after the correction is shown in Figure 4.3. This problem was not found neither in PIN1 nor in PIN2. After the correction, the resolution of PIN3 was comparable with the resolution of PIN1. We therefore chose to use the sum of PIN1 and the corrected PIN3 energies as energy loss measurement for the particle identification. As Figure 4.4 shows, using this combination of energy loss measurements improved the resolution compared to what can be achieved with individual detectors.

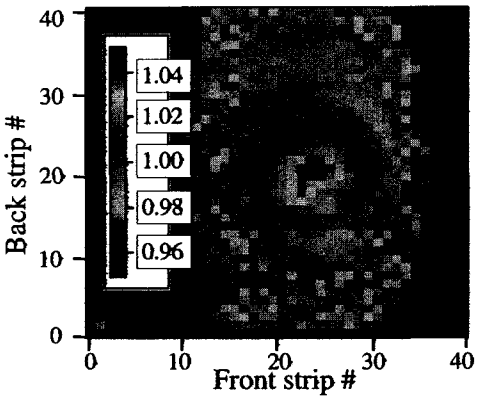

Figure 4.2: Correction factor for the PIN3 energy response as a function of pixel position in DSSD

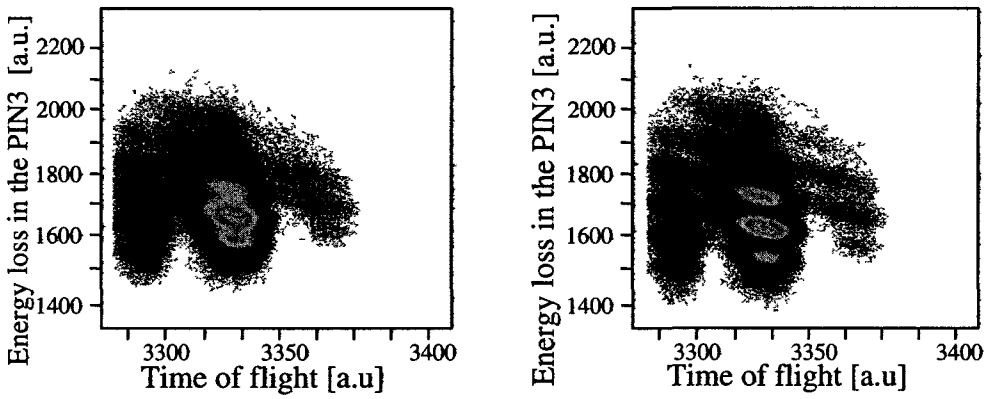

Figure 4.3: PIN3 resolution before (left panel) and after correction (right panel)

4.1.2 Cleaning gates

The time of flight and energy loss used for particle identification were measured in multiple ways because the selection of events that show consistency across different measurements of the same parameter improves the quality of the PID. The time of flight measured using the cyclotron RF and the time of flight measured using the XFP scintillator are expected to be proportional. Figure 4.5 shows that some particles did not fulfill the expected relationship, and thus, were rejected to improve the reliability of the particle identification. A similar approach was applied to the energy-loss measured with PIN1, PIN2 and PIN3. Figure 4.6 shows the

proportional relationship between the three quantities and the rejection criteria.

4.1.3 Total kinetic energy

In the particle identification plot discussed in Figure 4.4, the limited mass separation is mostly due to the large 1% momentum acceptance of the fragment separator system, which allows nuclei of different velocities –and thus, different time of flights–to reach the experimental station. Because the time of flight is related to the total kinetic energy, the possibility of using the total kinetic energy for an additional A/Q discrimination was explored. In order to measure the total kinetic energy of the fragments implanted, the energy deposited in each PIN detector had to be added to the energy deposited in the DSSD. Before this could be done, a problem illustrated in Figure 4.7(a) had to be solved. In this figure the response (in channels) of two adjacent back strips of the DSSD are plotted versus each other for the subset of implantation events of ^{96}Ag that only deposited energy in these two strips. Because the two strips share the energy deposited by the implantation, the plot is expected to be a straight line with slope -1. The recorded response shown

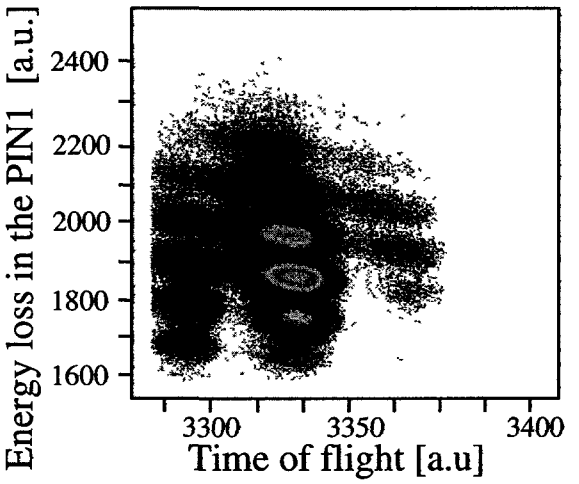

Figure 4.4: PID using the sum of energy loss in PIN1 and PIN3

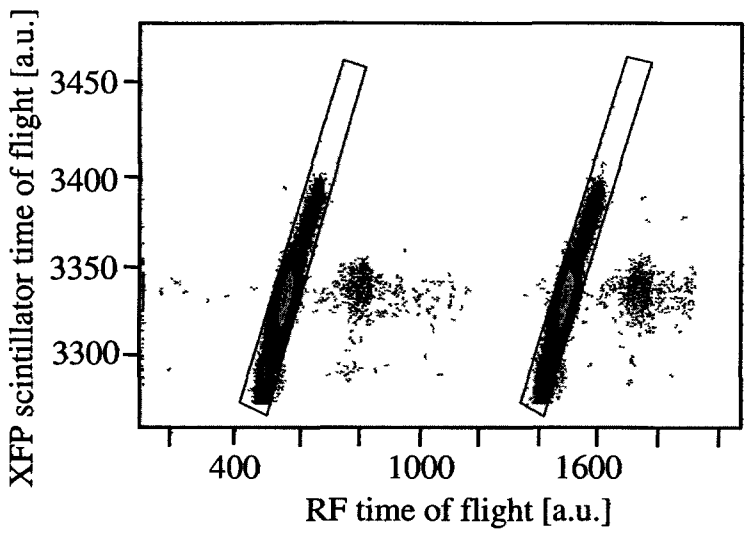

Figure 4.5: Time-of-flight measured using the focal plane scintillator vs. the time-of-flight measured using the cyclotron-RF signal. Because the RF-tof was double, two gates had to be defined.

in red clearly deviates from the expected behavior, indicating a saturation effect in the preamplifier. For the front strips, the effect is even more severe. However, this effect can be corrected using an appropriate correction function. This function has to be linear for small signals (when there is no saturation), and have an asymptote to simulate the saturation. The tangent function fulfills these requirements. Given a raw response of a back strip of DSSD in channels, the corrected response, is given by:

$$E_{corrected} = 650 \times E_{raw} \times \tan\left(\frac{E_{raw}}{1200}\right) \tag{4.1}$$

This correction function is shown in Figure 4.7(b). Using this correction function, the plot of two adjacent back strips (one versus the other) shows now the expected behavior (blue data in Figure 4.7(a)). The coefficients 650 and 1200 in the relation 4.1 were obtained simply by trial-and-error. The first coefficient is only a re-scaling factor, while 1200 could be interpreted as the raw channel at which the saturation

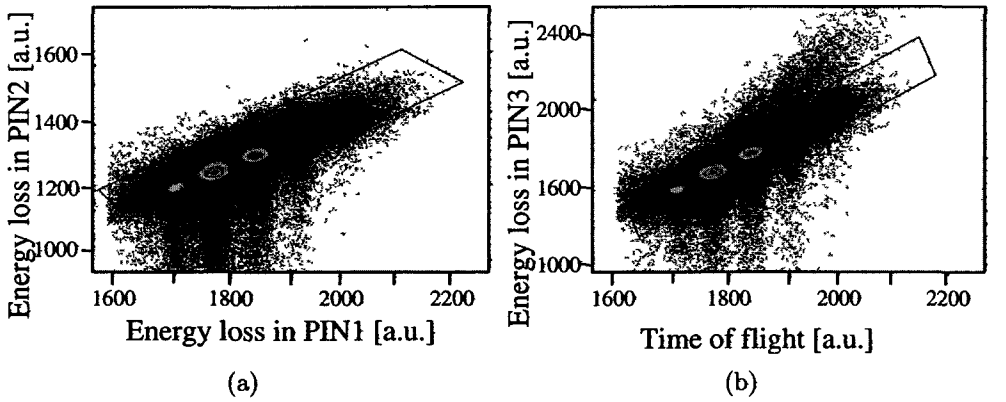

Figure 4.6: Plot of the energy loss in a) PIN1 vs PIN2 and b) PIN1 vs PIN3.

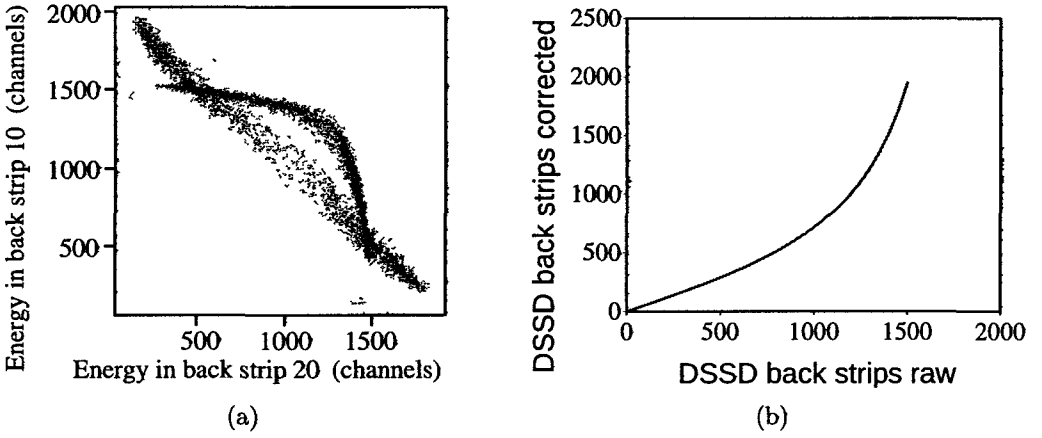

Figure 4.7: (a) Implantation energy of two adjacent strips plotted versus each other for the subset of implantations of ^{96}Ag that only deposited energy in the two strips. The red data shows a saturation in the preamplifier (see Section 4.1.3 for details). After correcting the strip responses using the correcting function illustrated in panel (b), the blue data are obtained.

starts. Figure 4.8 shows the effect of this correction on the DSSD energy resolution. The figure shows the energy deposited in two adjacent strips before and after the correction is applied. The last step before summing the three PINs and the DSSD energy loss to obtain the fragment's TKE was to energy calibrate the four detectors. This was done using the whole range of contaminants implanted in runs with the RFFS slits open, comparing the individual detector responses in channel with the

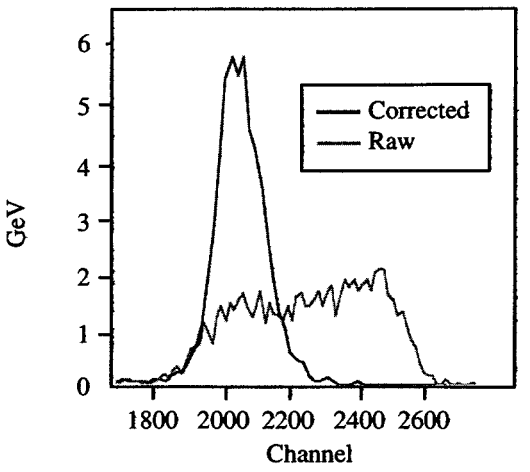

Figure 4.8: Implantation energy of two adjacent strips. The effect of the re-scaling factor 650 is to move the centroid of the two distribution relatively to each other. Ultimately the meaningful quantity in this figure is the width of the two distributions.

expected energy deposition simulated with the LISE++ code [70].

Figure 4.9(a) show the plot of the XFP time-of-flight versus the DSSD back energy (sum over all strips) for the fragment ^{96}Ag. However, the width of the distribution is larger than the 2% change that corresponds to the 1% momentum acceptance (dE/E= 2dp/p). Figure 4.9(b) shows the total kinetic energy of ^{96}Ag fragments plotted versus time-of-flight. This dependence is not stronger than DSSD energy vs. TOF. This is in part due to the low resolution of PIN2 who worsens the overall resolution. Either way, however, one finds that the TKE dependence of the TOF in relation to the resolution is not sufficient to provide additional A/Q discrimination. Nevertheless, a plot of TKE vs. TOF for all isotopes can be used to reject events that have the wrong TKE TOF relationship (see Figure 4.10) possibly because of reactions in the Si telescope where lighter reaction products can escape.

Figure 4.11 shows the particle identification plot resulting from the best deter-

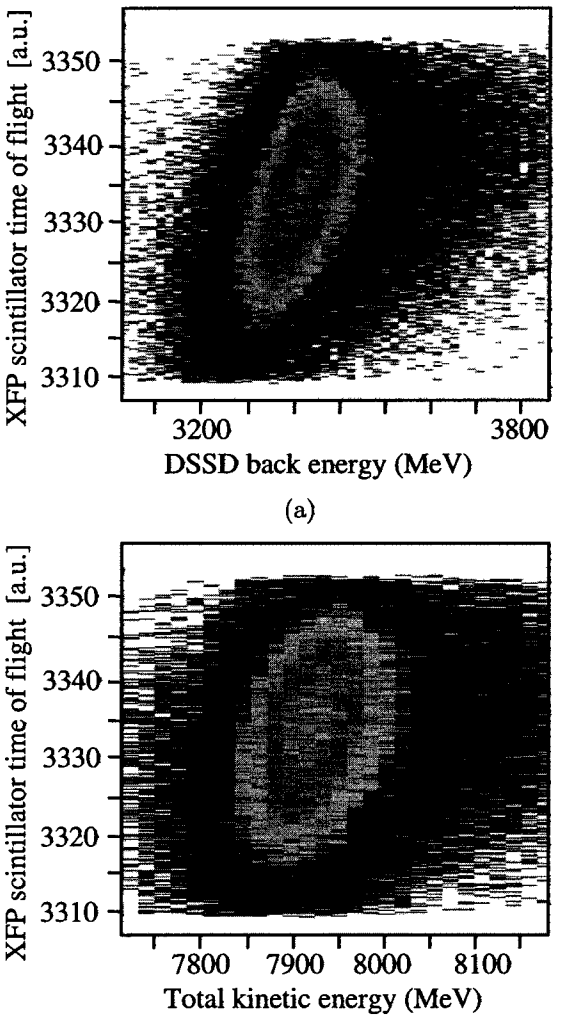

Figure 4.9: XFP tof plotted vs. (a) DSSD energy summed over all strips, and (b) TKE for the whole set of fragment

mination of energy loss and time of flight as discussed previously.

PID confidence level for each event

Figure 4.1.3 shows a plot of the Z (related to energy loss) spectrum for Z=46,47,48 obtained from a 1-hour run. The distribution can be fitted using three Gaussian functions with centroids fixed to the values 46, 47, 48. The heights of each peak are

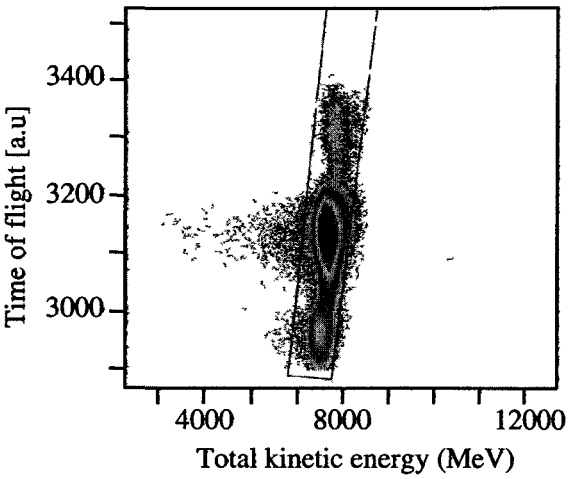

Figure 4.10: XFP tof plotted vs. the total kinetic energy for all isotopes.

free parameters in the fit. The one width common to the three functions is also a free parameter, with the best fit giving FWHM=0.53. The separation in Z is satisfactory and a gate can easily by applied to eliminate most contamination without significant loss in statistics. The situation in terms of A separation is shown in

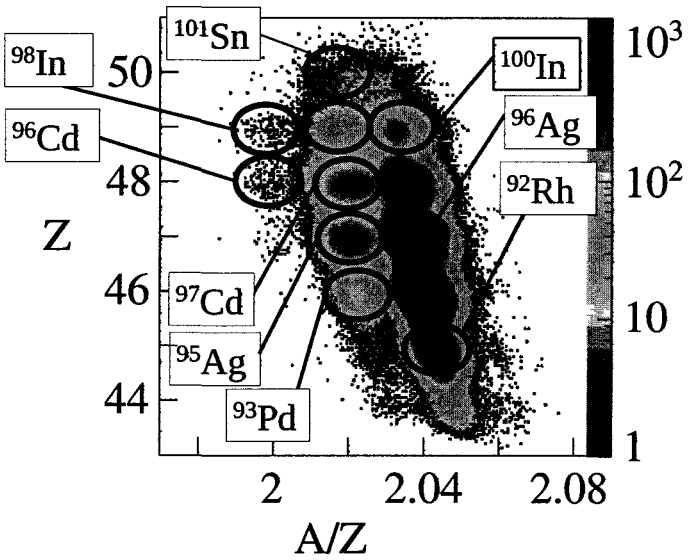

Figure 4.11: Particle identification plot obtained as described in the text. The lightest isotopes have higher time of flight (small A/Z). Each blob in the figure indicates one of the nuclei discussed in this work.

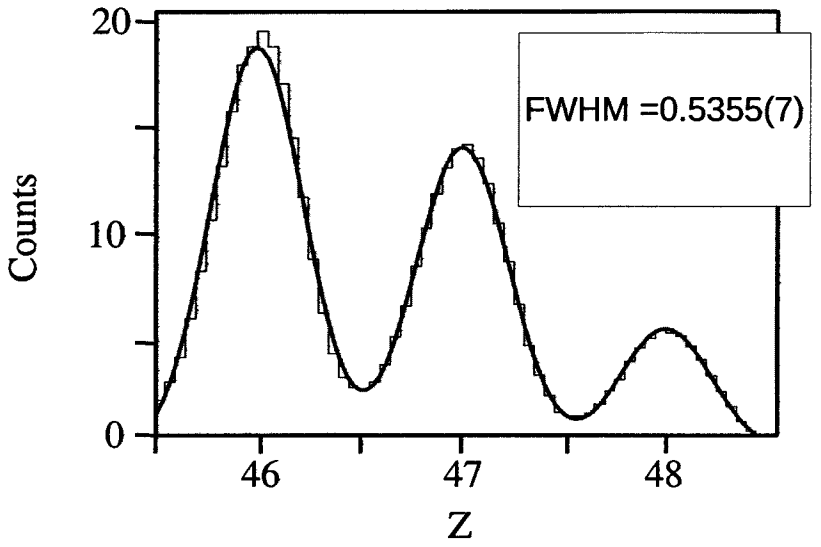

Figure 4.12: Fit of the charge peaks (energy loss) in PIN1. The overlap between different distribution is small.

Figure 4.1.3. In this case the fitting functions are a superposition of Gaussian and box functions that simulate the 1% acceptance of the fragment separator. The A separation is clearly more difficult than the Z separation. A gate can still be applied that eliminates contamination, but the loss of statistics would be relevant. In the case of the N=Z nuclei, which are produced with low rates, larger gates that did not exclude any events were used. The analysis then quantitatively took into account contamination from neighboring less exotic isotopes calculated using the mass-fitting curves shown.

4.2 Calibration of the experimental station

The β counting system has been introduced in Section 3.3.3. The current section provides details about the calibration of the detectors of the silicon stack including

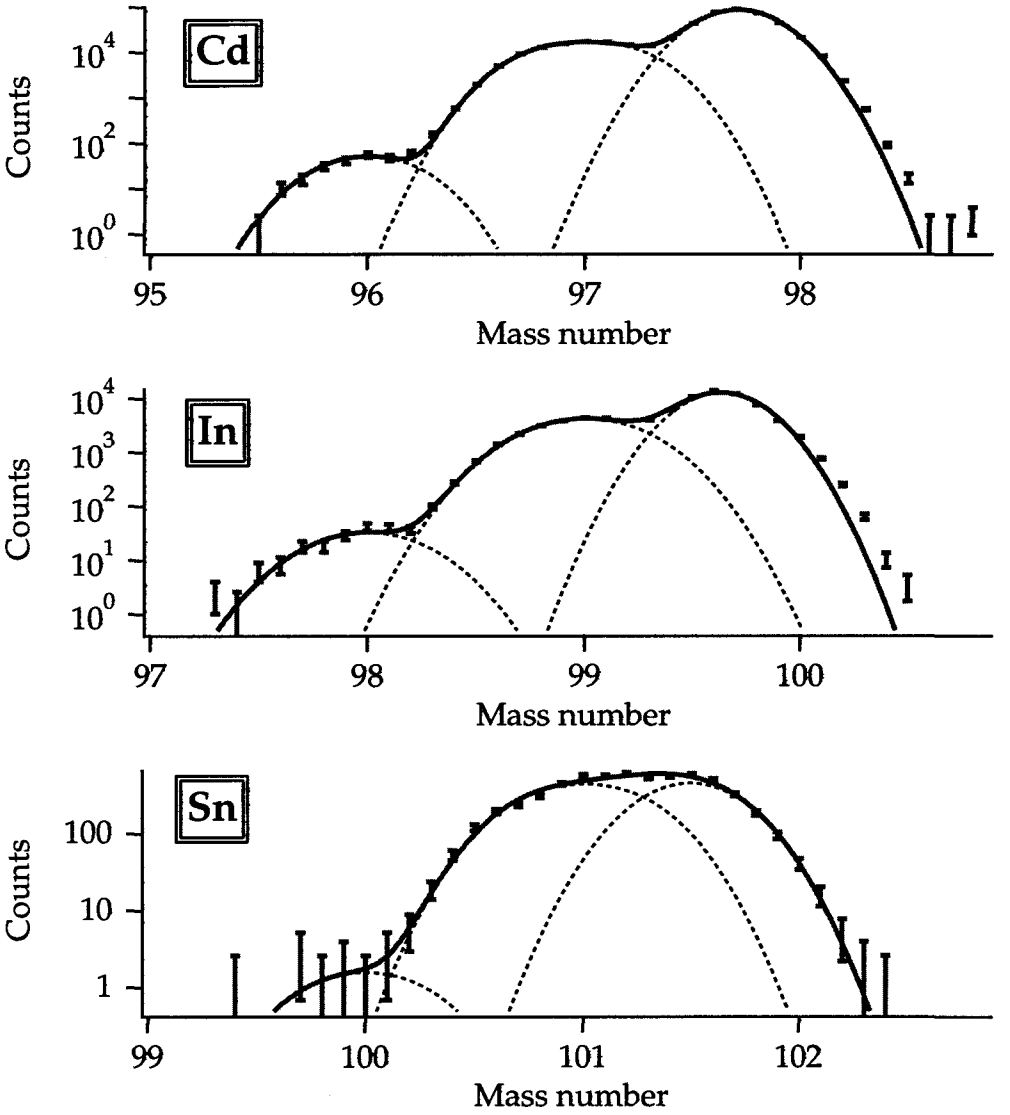

Figure 4.13: Fit of the mass peaks using a convolution between a Gaussian and a square function.

the final Ge-detector and the calibration of the SeGA detectors. Also, it reports the study of the DSSD response to protons.

4.2.1 BCS gain match, threshold setting, and energy calibration

The DSSD electronics for the detection of light charged particles like β-particles and protons was set up and calibrated in several steps. A standard ^{228}Th α-source was used to set the coarse hardware gains of the shaper-amplifier modules. The decay chain of ^{228}Th provides seven alpha particles of different energies that are recorded as 5 resolved peaks in our detector. The shaper-amplifier gains were set to position the 6.089 MeV peak at the limit of the range of the ADCs. In addition, a ^{90}Sr/^{90}Y source was used to set conservative hardware thresholds based on count rate. The thresholds were set just above the electronic noise of the detector, giving a tolerable count rate in terms of random coincidences between front and back strips. This aspect is important because random coincidences contribute to the data acquisition dead time. To further minimize the background and to maximize the efficiency, adjustable software thresholds eliminating the electronic noise were also applied. Figure 4.14 shows a typical software threshold. The figure also shows the offset that was applied in order to have the spectrum starting at channel zero. Then, the DSSD and SSSD's strips were software gain-matched for the ^{228}Th source so that a given alpha-peak appeared in the same channel in each strip. The alpha-spectra after the gain match of representative DSSD strips are shown in Figure 4.15. For each spectrum, the peak channels were extracted from a Gaussian fit and related to their known peak energies, thus providing the channel-to-energy calibration. These calibrations are linear in the region covered by the ^{228}Th source and their examples are also shown in Figure 4.15.

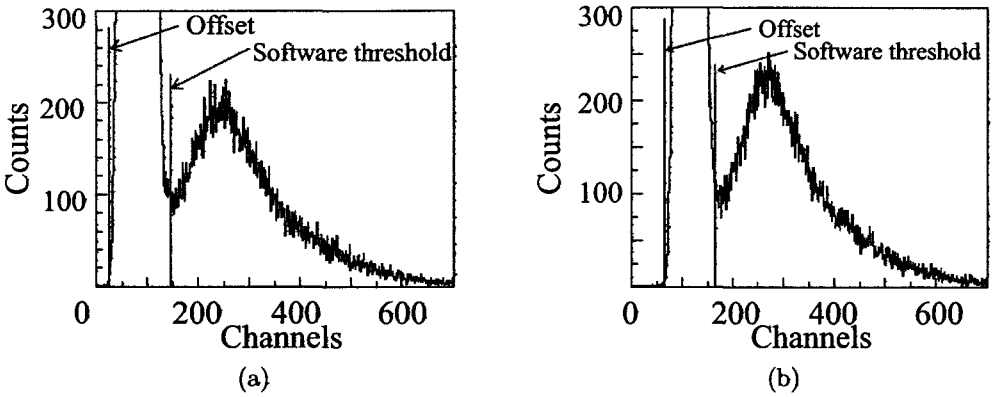

Figure 4.14: Spectra of the energy deposited by β-particles from the decay of the $^{90}Sr/^{90}Y$ source recorded by the front strip #21 of the DSSD (a) and by the back strip #21 of the DSSD (b). The spectra are gain-matched.

4.2.2 Calibration of the Ge-detector

The last detector of the stack was calibrated with a γ-source of ^{207}Bi. This source has two γ lines at 569.7 and 1063 keV and its γ-spectrum observed by the Ge-detector is shown in Figure 4.16. The corresponding linear calibration of the detector is:

$$E(\text{keV}) = 0.7569 \times channel - 35.505 \tag{4.2}$$

The detector was calibrated after the experiment, and the calibration highlighted a problem illustrated in Figure 4.17, which shows a γ-spectrum recorded by the detector in coincidence with β-decay events of ^{96}Ag. The amplifier gain was set too high for energies above 3 MeV causing overflows in the ADC.

4.2.3 Calibration of the Segmented Germanium Array

The SeGA detectors were calibrated twice, once before and after the experiment. These detectors were calibrated with a ^{56}Co radioactive source and a mixed source (SRM) containing ^{125}Sb, ^{152}Eu, ^{154}Eu, and ^{155}Eu [71]; the corresponding γ-line

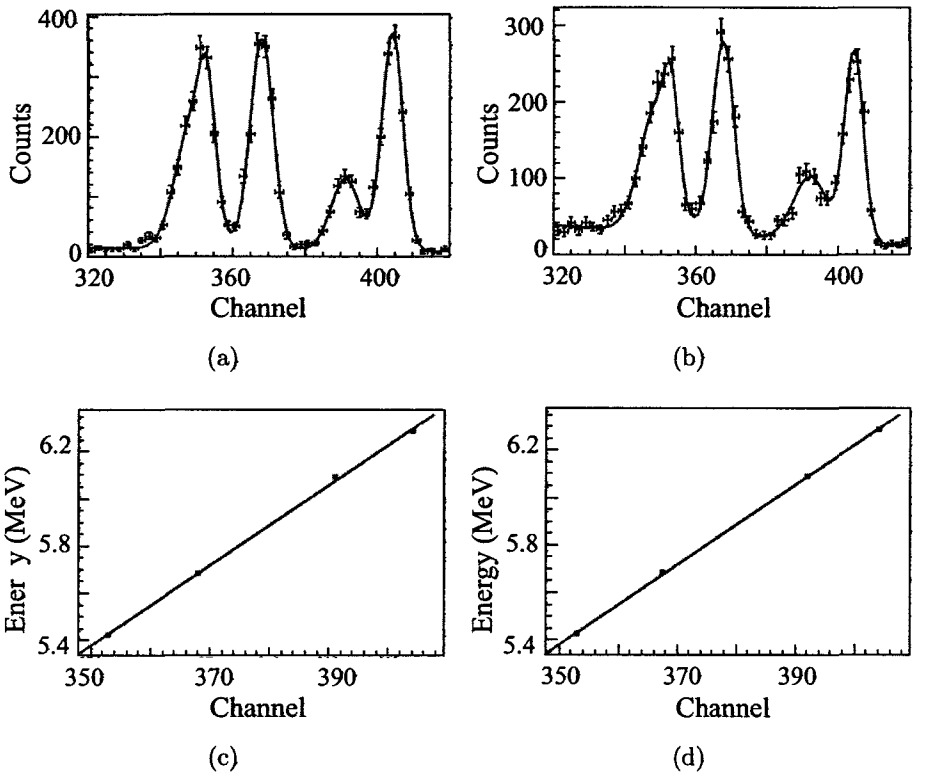

Figure 4.15: Spectra of α-particles emitted by the ^{228}Th source recorded by the front strip #14 of the DSSD (a) and by the back strip #14 of the same detector (b). Gaussian fits of the spectra are also shown. Channel-to-energy calibrations for the front strip #14 and the back strip #14 are presented in (c) and (d), respectively.

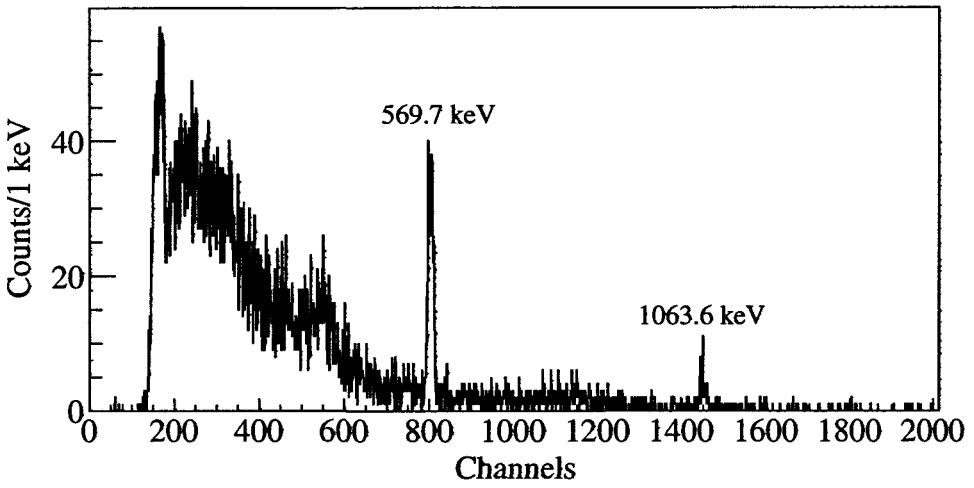

Figure 4.16: γ-spectrum of the ^{207}Bi source observed by the Ge-detector. The two highlighted lines were used to calibrate the detector.

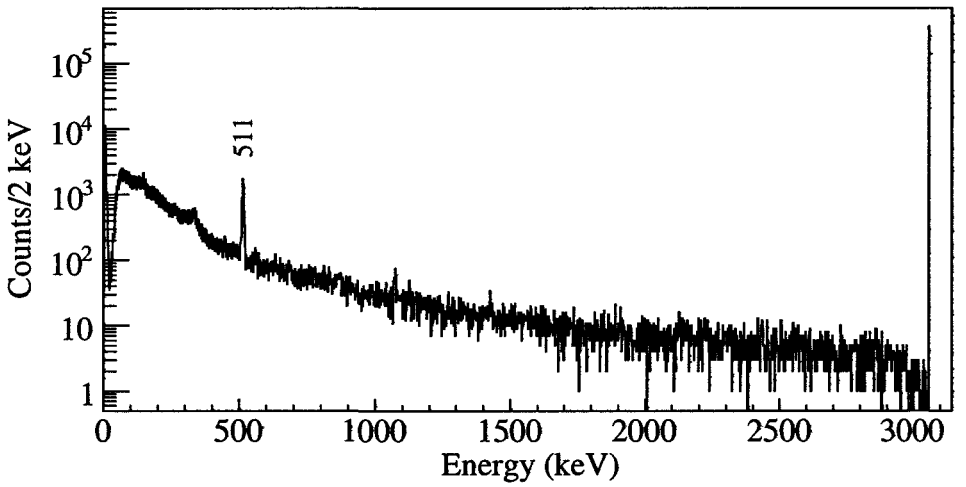

Figure 4.17: Calibrated Ge-detector γ-spectra in coincidence with the β-decay of ^{96}Ag. Besides the 511 keV annihilation peak, the spectra also shows that signals more energetic than 3 MeV overflow the ADC.

energies are listed in Table 4.1. A third-order polynomial function was used for the energy calibration and an error of 1 keV was associated with the resulting calibration. Because of its poor energy resolution and unstable calibration, one detector (the detector number two) was excluded from the data analysis.

Table 4.1: γ-lines from the ^{56}Co and the SRM source used for SeGA calibration.

Isotope in the source	Energy (keV)
^{154}Eu	123
^{154}Eu	247
^{125}Sb	427
^{125}Sb	463
^{154}Eu	591
^{125}Sb	600
^{154}Eu	723
^{154}Eu	846
^{154}Eu	873
^{154}Eu	996
^{154}Eu	1004
^{56}Co	1037
^{56}Co	1238
^{154}Eu	1274
^{154}Eu	1596
^{56}Co	1771
^{56}Co	2015
^{56}Co	2034
^{56}Co	2598
^{56}Co	3201
^{56}Co	3253
^{56}Co	3273

The calibration sources were placed in the beam line at the DSSD position at atmospheric pressure. For efficiency calibrations, the detection rate of SeGA was normalized to the known activity of each isotope in the calibration source, and a dead time correction was included in the analysis. The peak efficiency of the entire array was determined to be 6.1% at 1 MeV. The calibration function resulting from the analysis of the calibration run was:

$$\epsilon_\gamma(E) = A\ (E - C)^{-B} \tag{4.3}$$

where E is the energy in keV and with:

$$A = 24.7246$$

$$B = 0.838566$$

$$C = -194.255$$

4.3 Analysis of β-delayed proton events

This section describes the analysis that enabled to distinguish protons from positrons (Section 4.3.1) and to obtain energy spectra for the βp-decay events (Section 4.3.2).

4.3.1 Identification of the β-delayed proton events

The DSSD energy spectrum of decaying ^{96}Ag is shown in Figure ??. In the decay of ^{96}Ag, either a positron alone or a positron along with a proton are emitted. Since positions can easily escape the detector depositing only a fraction of their energy, pure positron decays contribute mostly to the low energy spectrum. On the other hand, events with the β-decay followed by a p-emission contribute to the higher energy region. In the latter case, the emission of the two particles is basically simultaneous, and so the detector records the full energy of the proton and a fraction of that of the positron. The energy spectra of the two kinds of decay events overlap, however, because a positron alone from a pure β-decay may deposit the same amount of energy as a positron-proton pair originating from a βp-decay.

Figure ?? and Figure ?? show the spectra of decays depositing their energy in only one strip and only one pixel, respectively. The contributions from pure β-decays and βp-decays still overlap in the one-strip spectrum, but they are perfectly

separated in the one-pixel spectrum. As can be inferred from Figure ?? and also from MCNPX simulations (see Section 4.5), the maximum energy deposited by β-particles in a single pixel of the DSSD can not be greater than about 1.3 MeV. β-particles can deposit an amount of energy comparable with that of protons only if they travel trough multiple pixels. On the other hand, the emitted protons do not have energy smaller than about 1 MeV because of the Coulomb barrier. Therefore, we define a βp-emission as an event where the implantation pixel or

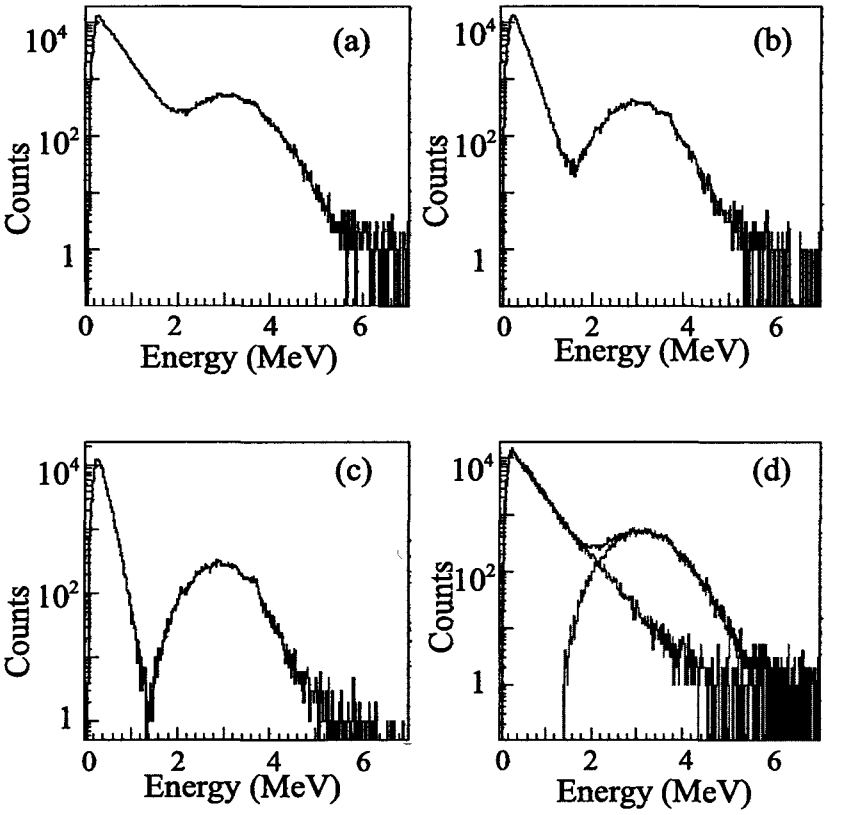

Figure 4.18: Spectra of the energy deposited in the DSSD by the decay events of ^{96}Ag under the following conditions: (a) with no selections, (b) selecting events that deposited their energy in one strip only, (c) selecting events that deposited their energy in one pixel only, and (d) using the selection procedure described in this section. In the last case, each event (black histogram) was classified as a β-decay either followed (blue histogram) or not (red histogram) by a proton emission.

an adjacent pixel records an energy greater than 1 MeV. In principle, protons emitted near the strip boundary with energies smaller than 2 MeV could deposit less than 1 MeV in each of the two adjacent pixels, and such events could escape identification. However, MCNPX simulations results show that these cases are sufficiently rare, and thus they were neglected. MCNPX suggested that the number of those events is only about 1% for protons of 1.5 MeV and dropping to 0.1% for 2 MeV protons and are therefore negligible. In these simulations, a uniform implantation distribution in the plane of the detector and a Gaussian distribution (100 μm FWHM) of implantation depths were assumed following predictions of the code LISE++. Simulated protons were started with a bell-shaped energy

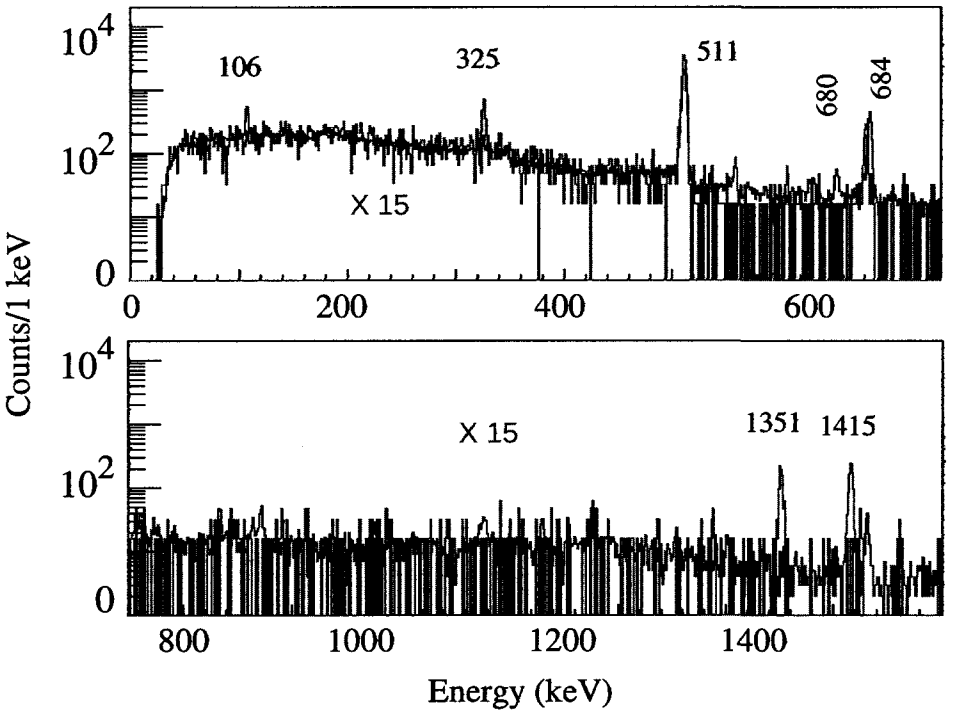

Figure 4.19: γ-spectrum of daughter nuclei of ^{96}Ag gated on β-decays (red) and βp-decays (blue) of ^{96}Ag. The blue histogram was multiplied by a factor of 15 to facilitate the comparison between the two spectra. The fact that the two spectra do not have common peaks shows a satisfactory identification of the βp-events.

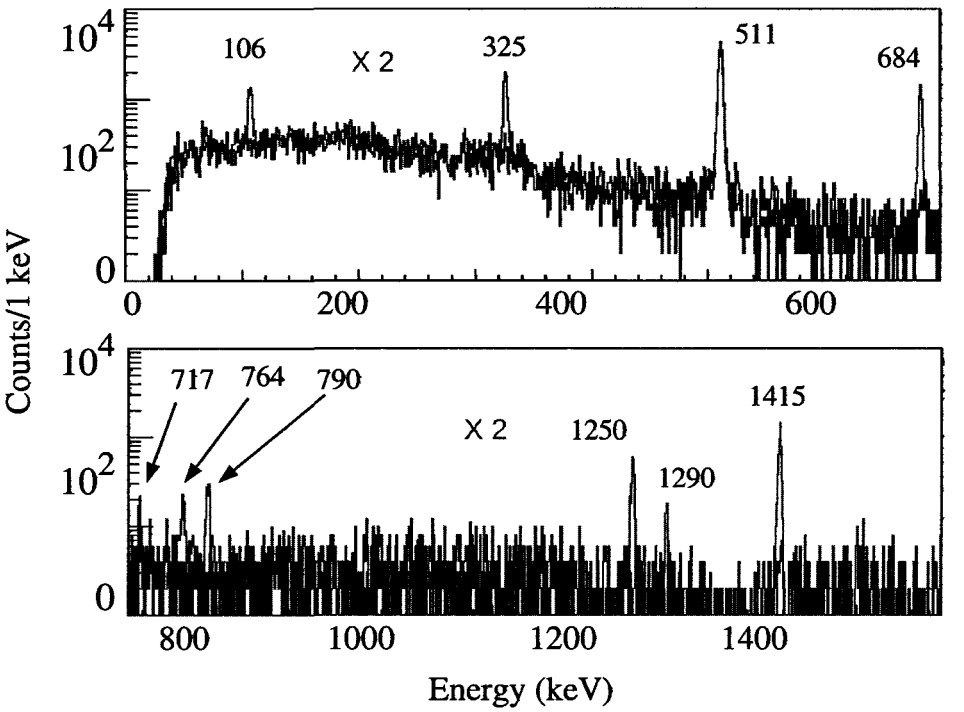

Figure 4.20: γ-spectrum of daughter nuclei of ^{97}Cd gated on β-decays (red) and βp-decays (blue) of ^{97}Cd. The blue histogram was multiplied by a factor of 2 to facilitate the comparison between the two spectra. The fact that the two spectra do not have common peaks shows a satisfactory identification of the βp-events.

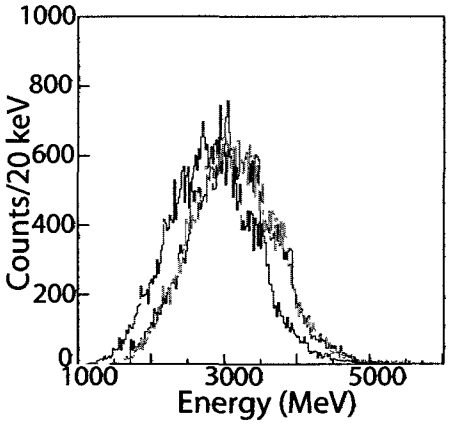

(a) Batist et al. (2003)

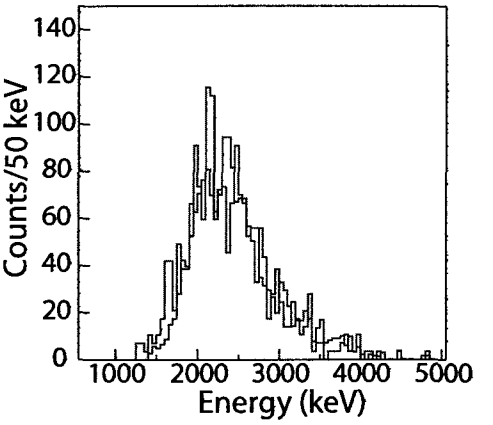

(b) Schmidt et al. (1994)

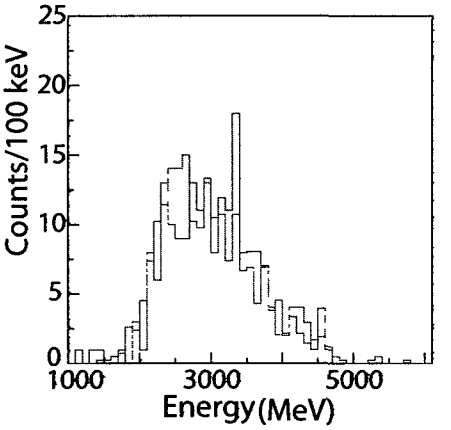

(c) Schmidt et al. (2000)

Figure 4.21: Comparison between the spectra of the energy deposited by the βp-events in this work (blue) and in the literature (red) for ^{96}Ag (a), ^{95}Ag (b), and ^{93}Pd (c). The green histogram in the panel (a) results from shifting the blue spectrum by about 200 keV to match the literature report.

spectrum defined between 0-6 MeV, and centered at around 3 MeV (such a proton spectrum is typical for heavy nuclei as explained in chapter 2). As a reference, typical ranges of protons in Si are: 20μm for 1 MeV protons, 100μm for 3 MeV protons, and 350μm for 6 MeV protons.

As demonstrated in Figure ??, the definition of a βp-decay event introduced above allows one to distinguish these events from pure β-decays. However, such a decomposition does not discriminate between β-particles and protons emitted together in a βp-decay, hence the spectrum of those decays is the sum of the proton's full energy and a small energy loss of about few hundreds keV from the β-particle largely escaping the detector.

The discrimination between β- and βp-events was tested by using β-delayed and βp-delayed γ-rays. The basic idea is that, for a given isotope, a γ-ray from a transition in the β-daughter should not be present in the γ-spectrum gated on βp-emission events. Similarly, γ-peaks characteristic for the βp-daughter should not be observed in the spectra gated on pure positron emission events. The results of such a study for ^{96}Ag and ^{97}Cd are shown in Figure 4.19 and Figure 4.20, respectively. In the case of ^{96}Ag, the β-decay of ^{96}Ag to excited states of ^{96}Pd is followed by the emission of 106, 325, 684, and 1415 keV γ-rays, while the βp-decay of ^{96}Ag to excited states of ^{95}Rh is followed by the emission of 680 and 1350 keV γ-rays. The selecting power of the βp-gate was particularly evident after observing the γ-ray at 680 keV from the βp-decay of ^{96}Ag which was otherwise completely overwhelmed by the much stronger radiation at 684 keV from the β-decay of ^{96}Ag. In the case of ^{97}Cd shown in Figure 4.20, the γ-peaks at 107, 325, 684, 790, 1250, and 1415 keV stem from the deexictation of levels in ^{96}Pd populated by the βp-decay of ^{97}Cd, whereas the peaks at 717, 763, and 1290 keV are transitions in the β-decay daughter nucleus ^{97}Ag. Again, β- and βp-delayed γ-rays are safely

distinguished.

Another test of our discrimination algorithm was performed with nuclei that are known to have no or negligible βp-branchings such as ^{94}Pd, for which having an experimental upper limit of 0.025% for the βp-decay exist [?]. As illustrated in Figure 4.22, our algorithm indeed identified all decay events as β-decays with no βp-decays in agreement with our expectations. The final test of the discrimination algorithm consisted of comparing the βp-energy spectra recorded in this work to those reported in the literature for the precursors ^{95,96}Ag and ^{93}Pd [3, 36, 72]. Besides a possible calibration problem in panel Figure 4.21(a), there is an overall satisfactory agreement in the spectral shapes in Figure 4.21 that reinforces our analysis.

4.3.2 Minimization of the β-summing

As stated in Sec. 4.3.1, for βp-decays the proton energy was collected along with a fraction of the positron energy. This section reports on the effort to minimize the effect of the positron energy, the β-summing effect, in order to obtain the actual proton energy as close as possible.

We considered two different methods to collect the energy of the βp-decay event. In the first method, the energy deposited in the entire detector was assigned to the event. In the second method, only the energy from the strip that had recorded the maximum energy was assigned to the βp-event.

To compare the two methods, we used MCNPX simulations to calculate the fraction of the proton energy collected in a single strip. A uniform implantation distribution in the plane of the detector was assumed along with a Gaussian distribution (100 μm FWHM) of implantation depths, as predicted by the code LISE++. In these simulations, protons were emitted from implantation locations

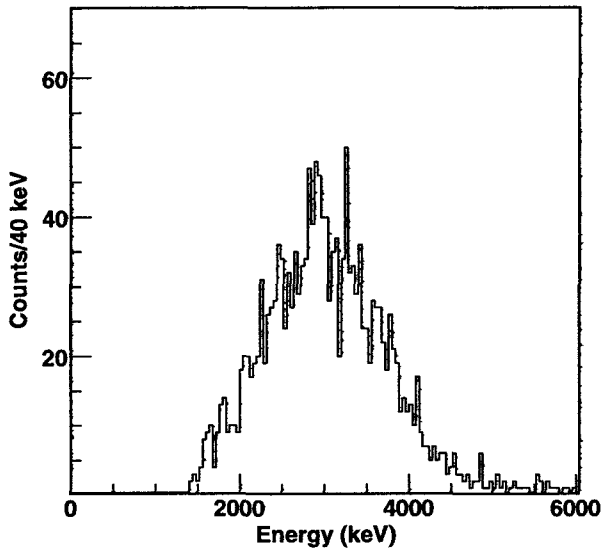

(a)

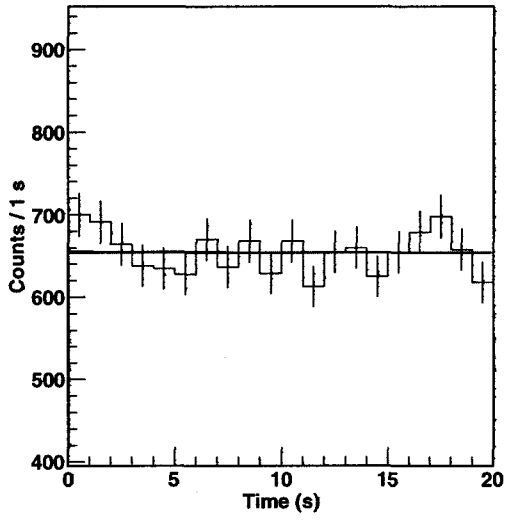

(b)

Figure 4.22: a) Energy spectrum of βp-events correlated in time with the implantations of ^{94}Pd. This nucleus is known to have no proton branching ratio. (b) Decay curve of these events, fit with an exponential component and a background component. The decay curve shows no evidence for a 9 s half-life of ^{94}Pd demonstrating that these events are due to random coincidences rather than βp-decay of ^{94}Pd.

isotropically and mono-energetically. Figure 4.23 illustrates the results suggesting a low probability (less than 10%) for the protons with energy 0–4 MeV relevant to our work to escape the implantation strip. In addition, Figure 4.24 shows the βp-energy spectra recorded with the two methods along with a βp-spectrum reported in the literature [3] for the case of ^{96}Ag. The spectrum reported in the literature was not affected by β-summing because nuclei were implanted in a foil and the relevant particles from βp-decays were detected outside the foil. Therefore, it was possible to select protons emitted in directions opposite to those of positrons, thus eliminating β-summing. The agreement between the βp-energy spectrum from [3] and that recorded in this work using the second method (see Figure 4.24(a)) confirms conclusions of our simulations that only a negligible fraction of proton's energy is missed when using a single strip to detect protons. To the contrary, the βp-energy spectrum in Figure 4.24(b) recorded using the first method shows a significant contribution from β-summing. Based on these arguments, the second method of energy collection proved to be a better choice for our data analysis because in this method nearly the full energy of the proton is collected while excluding the energy deposited outside of the implantation strip mostly due to positrons.

An effort to estimate the contribution of the β-summing for each βp-event was based on the idea that an electron emitted from the DSSD and also detected in a SSSD could show a correlation between the energy deposited in DSSD and in the SSSD. If this was the case the β-summing could be estimated from the energy loss in the SSSD. Figure 4.25 suggests that there is no correlation between the two energy loss. On the other hand, the lack of correlation could be explained by the fact that for electrons, the energy loss in a Si detector is not directly related to its own energy.

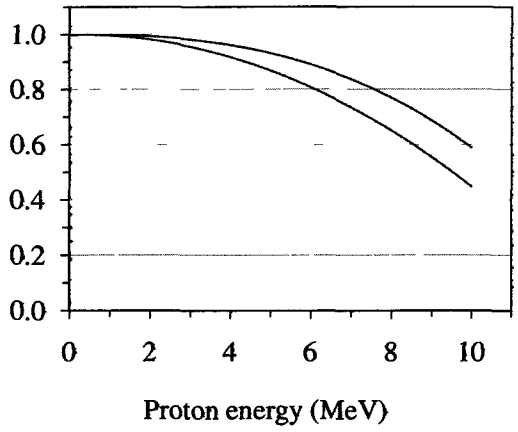

Figure 4.23: Simulation of the fraction of the proton energy deposited in the decay strip (blue line) as a function of the proton energy. The fraction of the proton energy deposited in the decay pixel is represented by the red line.

4.4 Implantation- and decay-event correlations

A low-gain (high-energy) signal in the DSSD was defined as an implantation if it was also recorded in PIN1. A pixel was assigned to each implantation based on the back strip and the front strip that had simultaneously recorded the highest energy. On the other hand, high-gain (low-energy) signals recorded in the DSSD, but not in PIN1 were defined as β-decays. A veto condition for decay events consisted of a signal from any strip of the SSSDs (downstream of the DSSD) that exceeded 1.5 MeV, or a strip-sum signal exceeding 3 MeV.

β-decays were continuously correlated with a preceding heavy ion implantation having occurred within a predefined position and time correlation window. Different position correlation windows were used in this work depending on background conditions, the implantation rate, and the type of measurement (i.e. half-life, $P_{\beta p}$, observation of β-delayed γ-rays). In general, two position correlation windows were employed: (a) a cross-shaped correlation window consisting of the detector

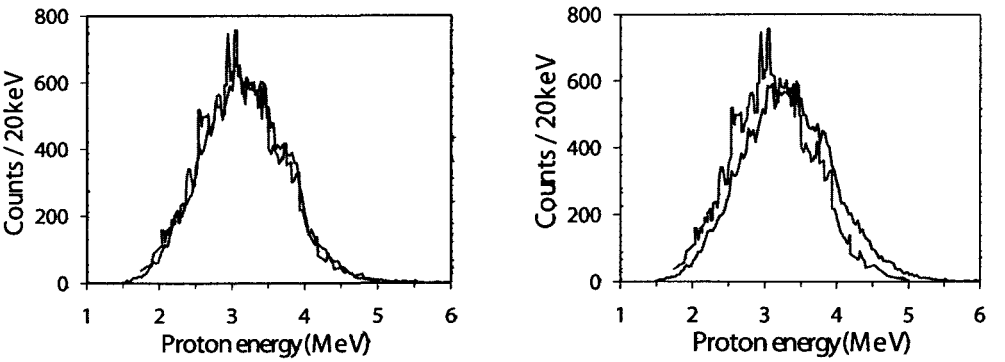

Figure 4.24: Comparison between the proton energy spectrum from [3] (blue histogram) and the spectrum of the energy deposited by βp-events in this work (red histogram). All spectra are for decays of ^{96}Ag. The red histogram was recorded by collecting the energy of βp-events deposited in (a) the implantation strip and (b) the entire detector.

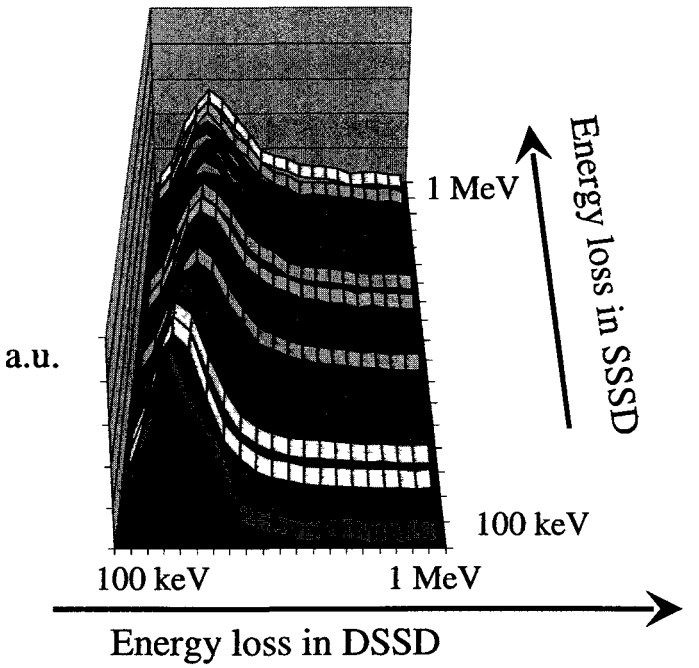

Figure 4.25: Energy loss in the DSSD as a function of the energy loss in the SSSD. This plot suggests that there is no correlation between the two energy loss.

pixel where the decay event occurred, plus the 4 neighboring pixels (two pixels in horizontal and two pixels in vertical directions), and (b) a single-pixel window that only consisted of the decay pixel.

Position-correlated implantantions and decays were then correlated in time. The correlation time window depended on which kind of measurement was required. For half-life measurements, a long correlation time (about 20 times larger than the expected half-life) was chosen since it allows one to best estimate the background and long-lived components such as daughter and granddaughter decays. This improves the accuracy of the resulting half-lives.

The β-detection efficiency for the cross-shaped correlation window was 36(4)% as determined based on decay curves of ^{95}Ag, ^{93}Pd, ^{96}Ag, and ^{100}In having known half-lives $T_{1/2}$. The fit of decay curves allows one to determine the initial detected activity A_0 from which the detection efficiency is computed as $\epsilon_\beta = \frac{A_0 T_{1/2}}{0.693 N_{imp}}$ where N_{imp} is the number of implantations. By the same method, the β-detection efficiency for the single-pixel correlation was determined to be 18(2)%. The cross-correlation window is more suitable when working with high statistics of signals, whereas the single-pixel correlation is better to minimize the background. It is important to note that when going from single to cross correlations, the detection efficiency increases by a factor of 2 while the background increases by a factor of 4. Thus, the single-pixel correlation provides a better signal-to-background ratio.

Given that the proton detection efficiency is close to 100% for a single-pixel correlation, this type of correlation is always the best choice for proton detection. However, it should be noted that if the implantation pixel was not attributed correctly, the single-pixel correlation would fail to identify proton events. This is an aspect important for $P_{\beta p}$ measurements.

4.4.1 Decay curves

Trigger events (either implantations or β-decays) were tagged with an absolute time provided by a continuously counting VME clock module SIS3820 (50 MHz) continuously counting. The decay time for an individual ion was obtained by subtracting the time of the position correlated β-decay from the time of the implantation of the ion. For the most abundant species, decay events were correlated

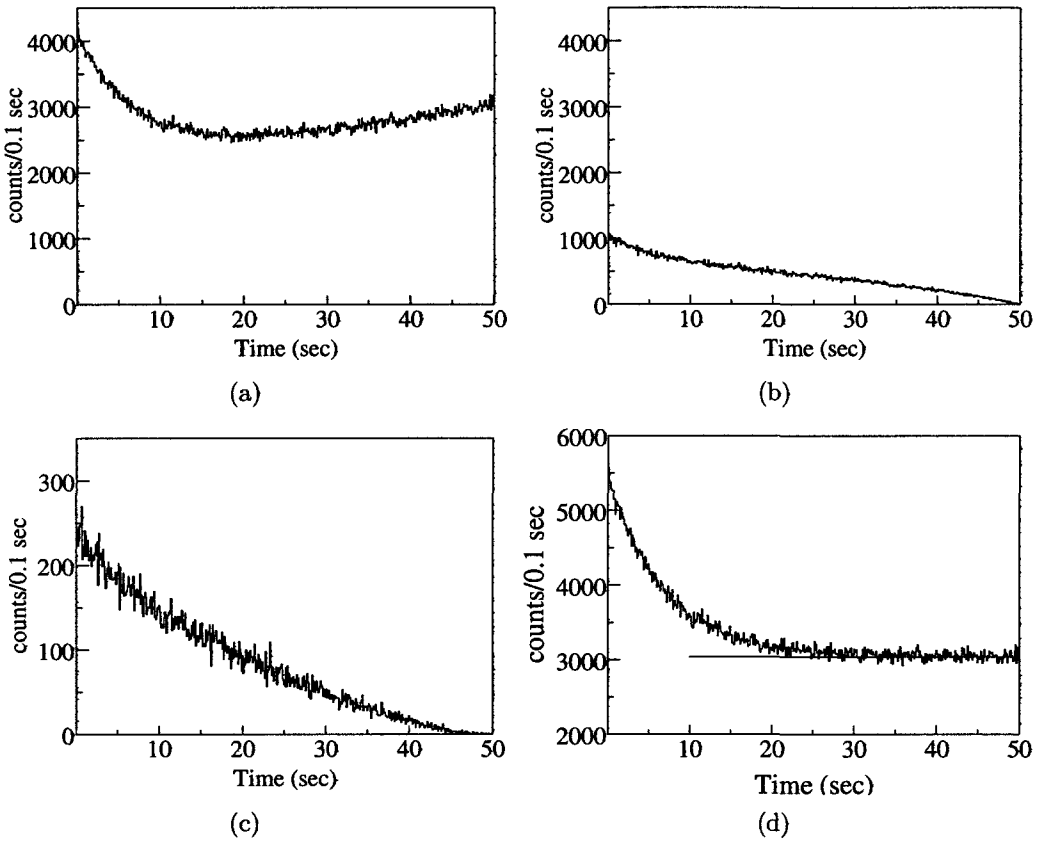

Figure 4.26: β-decay curves of ^{96}Ag obtained by correlating the implantation signal and the subsequent (a) first decay, (b) second decay, (c) third decay, and (d) all decays (1-8). In the last case, the background is not time dependent.

with more than one implant inside the time correlation window equal to 5 times the half-life, which is the shortest correlation time that guarantees precise fits.

In cases where the correlation between a decay and the preceding implantations was not unique, all possible correlations where considered to avoid time dependent background. Figure 4.26 shows that for ^{96}Ag (but the same holds true for the most abundant species) the background was significantly time dependent if β-decay events were correlated only with the implantation closest in time. To the contrary, there is no time dependence when all implants are correlated to a given β-decay (see Figure 4.26(d)).

The extent to which the background is time dependent depends on the implantation rate and on the half-life of the implanted ion. To illustrate the cases in which the correlation between a decay and the preceding implantations was not unique, Table 4.2 shows the average and the maximum implantation rate for all the species discussed in this work. This table does not include low-Z nuclei. The total implantation rate over the entire detector was about 50 counts per second. This rate led to an acceptable background rate of 0.03 counts per second and implant.

4.4.2 Decay Curve fitting

In order to extract half-lives, the distributions of implantation-decay time differences recorded for a particular nuclide were fitted to maximize a Poisson log-likelihood probability function that takes into account exponential decay of the parent nucleus as well as grow-in and decay of daughter and granddaughter nuclei when not gating on γ-rays. A constant background was included in the fit.

To fit decay curves, we employed the method described in [73], which is well suited for nuclear counting decay experiments where data obey a Poisson statistics.

Table 4.2: Implantation rate over the DSSD for nuclei discussed in this work

Nucleus	Implantation rate [sec^{-1}]		half-life
	Avg	Max	sec
^{92}Rh	0.35	1.2	5.3
^{93}Pd	0.21	0.5	1.1
^{94}Pd	0.15	4	9.0
^{95}Ag	0.72	1.5	1.8
^{96}Ag	0.95	4	6.9
^{96}Cd	0.001	0.003	1.0
^{97}Cd	0.063	1.2	3.8
^{98}Cd	0.35	1	9.0
^{98}In	0.001		0.6
^{99}In	0.015	0.04	3.0
^{100}In	0.047	0.015	5.9
^{101}Sn	0.0025	0.008	2.1

In this case, the relevant likelihood function is:

$$\mathcal{L} = \prod_{i=1}^{N} \frac{e^{-\mu_i} \mu_i^{n_i}}{n_i!} \tag{4.5}$$

where if data are binned in a histogram, N is the number of bins, μ_i is the average rate of decays occurring in the period of time corresponding to the i^{th}-bin, n_i is the ith-bin content. $\mathcal{L}$ is a function of the k unknown parameters to estimate θ=$(\theta_1, \theta_2 ....., \theta_k)$ thought $\mu_i(\theta_1, \theta_2, ...\theta_k)$. Since $\mathcal{L}$ and ln$\mathcal{L}$ are maximized by the same parameters, equation 4.9 is equivalent to maximize,

$$ln\mathcal{L} = \sum_{i=1}^{N} \left[\mu_i - n_i + n_i \ln \frac{n_i}{\mu_i} \right] \tag{4.6a}$$

$$= -\frac{1}{2} \chi^2_{ml}. \tag{4.6b}$$

Equation 4.6a is obtained taking the logarithm of equation 4.9 and using the Stirling's formula:

$$\ln n! = n \ln n - n \tag{4.7}$$

Equation 4.6b defines a function, χ^2_{ml}, that is minimized when the log-likelihood is maximized. The best fit parameters $\theta'= (\theta'_1, \theta'_2....\theta'_k)$ can be found solving the likelihood equations:

$$\frac{\partial \chi^2_{ml}}{\partial \theta_i} = 0, \qquad i = 1, 2..., k. \tag{4.8}$$

Because this equation is also satisfied by local maximum the quantities have to be calculated:

$$\alpha_{i,j} = \frac{1}{2} \frac{\partial^2 \chi^2_{ml}}{\partial \theta_i \, \partial \theta_j} > 0 \qquad i, j = 1, 2, ..., k. \tag{4.9}$$

For a decay experiment, the expectation value for the ith-bin content $\mu_i(\theta)$ is calculated based on the contribution of the parent decay $\mu_p(t, \theta)$, daughter decay $\mu_d(t, \theta)$ and granddaughter decay $\mu_{gd}(t, \theta)$ obtained solving the Bateman equations:

$$\lambda_1 \mu_p(t) = \lambda_1 \mu_p(0) e^{-\lambda_1 t} \tag{4.10a}$$

$$\lambda_2 \mu_d(t) = \frac{\lambda_2 \lambda_2}{\lambda_2 - \lambda_1} \mu_p(0) [e^{-\lambda_1 t} - e^{-\lambda_2 t}] \tag{4.10b}$$

$$\begin{aligned} \lambda_3 \mu_{gd}(t) = \lambda_3 \lambda_2 \lambda_1 \mu_p(0) \Bigg[& \frac{e^{-\lambda_1 t}}{(\lambda_2 - \lambda_1)(\lambda_3 - \lambda_1)} \\ & + \frac{e^{-\lambda_2 t}}{(\lambda_1 - \lambda_2)(\lambda_3 - \lambda_2)} + \frac{e^{-\lambda_3 t}}{(\lambda_1 - \lambda_3)(\lambda_2 - \lambda_3)} \Bigg] \end{aligned} \tag{4.10c}$$

where λ_1, λ_2 and λ_3 are the decay constants, $\frac{\ln 2}{t_{1/2}}$, of the parent, daughter and granddaughter nucleus, respectively. The fitting function $\mu_i(\theta)$=$\mu_p(t, \theta)$+$\mu_d(t, \theta)$+$\mu_{gd}(t, \theta)$ has to be modified if more decay components (isomeric states or exponential background components) are present.

Once the best fit values (θ') have been deduced, one can compute the uncertainty on the fit parameters using the matrix $\alpha_{i,j}$ that is related to the covariance matrix elements:

$$\sigma^2_{\theta_i,\theta_k} = \sum_{i=1}^{N} \left[\sigma_i^2 \frac{\partial \theta_j}{\partial n_i} \frac{\partial \theta_k}{\partial n_i} \right] \tag{4.11}$$

by the relation [74]:

$$\sigma^2_{a_j,a_k} \equiv \left[\alpha(\theta') \right]^{-1}_{j,k} \tag{4.12}$$

Equation 4.12 allows for the determination of uncertainties on the best fit parameters.

The advantage of using the Poisson-log-likelihood method compared to the method of the least squares is that the cases of low statistics are treated properly, whether the method of the least squares –based on the assumption that the content of a bin is Gaussian distributed–fails. Also, the methods deals with bins of null content. The limitation of the method is that the Poisson distribution requires events to be independent. This requirement is fulfilled by the β-p decay, but not by the β-decay events where parent, daughter, and granddaughter decays are correlated to each other. However, given the limited β-efficiency, the possibility that both parent and daughter decay are observed together is only 13% for the cross-pixel correlation, and 4.5% for the single-pixel correlation. Thus, in the majority of the cases, the events observed are uncorrelated. To overcome this limitation, a customized log-likelihood function should be defined (see [11, 75]).

4.4.3 Decay curves gated on β-delayed γ and β-delayed protons

The time distribution of correlated βp-emission events can be used to extract half-lives. This is advantageous compared to using all β-decay events in cases where the reduced background compensates for the lower statistics. The fits were performed in a similar way as for β-decay events, although without including daughter and granddaughter decays because their βp-branching ratios were always negligibly small.

γ-gated-β-decay curves are also a very convenient way to extract half-lives. At the expense of reduced statistics, the background is highly reduced, and no daughter and granddaughter decay have to be included in the fit.

4.4.4 Measurements of β-delayed proton branching ratios

The β-delayed proton emission branching ratios $P_{\beta p}$ –the number of protons emitter per β-decay–were extracted from the fit of βp-decay curves discussed in Section 4.4.3, which provides half-life and initial activity of the parent. The advantage of using the decay curve is that the constant background component included in the fit allows one to best estimate the background rate due to random correlations between an implantation and protons due to any other implantations. For an accurate determination of the background, a correlation time t_c longer than 10 half-lives was used.

A second source of background more difficult to estimate was caused by the contamination in the implantation set mostly due to a poor A/Q resolution of the particle identification spectra. The time distribution of this background is exponential with the half-life of the contaminant. The best way to deal with this

background is to restrict the implantation set by drawing a smaller gate in the PID plot. However, this was not possible for N=Z nuclei due to low statistics. In the case of N=Z nuclei an additional background exponential component had to be considered as explained later in this section.

The $P_{\beta p}$ were extracted from the fit of βp decay curves, which allowed to distinguish the protons originated by the random coincidences (first source of background above) from the protons originated by the real βp-decay. An example of this capability is shown in Figure 4.22 where protons where detected in coincidence with ^{94}Pd that is known to have no proton branching. The Decay curve of these events, however, shows a characteristic distribution typical of the background.

The fit of the decay curve provides the initial proton activity A_0, the half-life, and the background level. Therefore, $P_{\beta p}$ was calculated using the equation:

$$P_{\beta p} = \frac{N_{\beta p}}{N_{\beta p - parent}} \tag{4.13}$$

where $N_{\beta p - parent}$ is the number of implanted isotopes, and $N_{\beta p}$ is the number of βp-decay events correlated within t_c. $N_{\beta p}$ was calculated from:

$$N_{\beta p} = \frac{A_0}{\lambda}\left(1 - e^{-\lambda t_c}\right)^{-1} \frac{1}{T_{live}} \tag{4.14}$$

where A_0 and λ are the initial activity and the decay constant of the parent, both obtained from the fit of the decay curve, and t_c is the correlation time chosen. T_{live} was the fraction of time in which the detector system was not inhibited by other events processing. T_{live} was continuously measured using a random pulser, leading to a correction of less than 10%. For the N=Z nuclei ^{96}Cd and ^{98}In, for which the statistics was too low to restrict the implantation set to avoid contamination, a probability was assigned to the contamination level according to the mass

fit in the PID(see Figure 4.1.3). The fit of the βp-decay curve was performed with an additional exponential component whose half-life was fixed to the half-life of the N=Z+1 nucleus, and whose initial activity was determined from the PID confidence level fit (see Sec.4.1.3) and from the $P_{\beta p}$ measured in this work. In these cases, where the statistics is low and the fit is complicated by multiple components, errors were estimated by refitting for all variation of all the fixed parameters in the fit within their respective uncertainties, which defined the upper and lower limits for the free parameters.

When a β-decaying isomeric state was present, the analysis was further complicated by the fact that the decay spectrum was a mix of two exponential decays. If decay rates were sufficiently different and the statistics was sufficiently high to separate the two components in the β- and in the βp-decay spectra, individual βp-branching ratios and the relative production rate of the two states could be extracted. The assumption that the proton detection efficiency was 100% simplified these calculations because of the lack of contributions from βp-events where a proton was not detected. In the following expressions, $N_{\beta p}$ and N_{β}, are the number of detected βp-events, and pure β-events, respectively. They are labeled as "a" and "b" to indicate that they correspond to two different states. x is the relative fraction of state a.

$$N_{\beta p-a} = N_{imp}\ x\ P_{\beta p-a} \tag{4.15a}$$

$$N_{\beta p-b} = N_{imp}\ (1-x)\ P_{\beta p-b} \tag{4.15b}$$

$$N_{\beta-a} = N_{imp}\ x\ (1-P_{\beta p-a})\ \epsilon_{\beta} \tag{4.15c}$$

$$N_{\beta-b} = N_{imp}\ (1-x)\ (1-P_{\beta p-b})\ \epsilon_{\beta} \tag{4.15d}$$

This system of equations can be easily solved, resulting in:

$$P_{\beta p-a} = \frac{N_{\beta p-a}\ \epsilon_\beta}{N_{\beta p-a}\ \epsilon_\beta + N_{\beta-a}} \tag{4.16a}$$

$$P_{\beta p-b} = \frac{N_{\beta p-b}\ \epsilon_\beta}{N_{\beta p-b}\ \epsilon_\beta + N_{\beta-b}} \tag{4.16b}$$

$$x = \left(\frac{P_{\beta p-a}}{P_{\beta p-b}} + \frac{N_{\beta p-a}}{N_{\beta p-b}}\right)^{-1} \tag{4.16c}$$

4.5 MCNP simulations

One of the goals of our experiment was to measure β-decay Q values of the rare isotopes implanted. In order to perform this measurement, we used the simulation code Monte Carlo Neutron Particle transport (MCNP) to calibrate the detectors at low energy, and to study the response of the β-calorimeter. However, as it will be explained, several problems prevented us from reaching this goal.

In addition, simulations were also used for $P_{\beta p}$ measurements to evaluate possible proton detection failures due to wrong discrimination of β and βp-events. This section summarizes the basic algorithms that MCNP uses to simulate electron transport (Sec.4.5.1) and then discusses the setting that was used in this work (Sec.4.5.2). Finally, this section reports the results of the simulations.

4.5.1 Physics of the MCNP electron interaction

Electron transport is a problem of large computational complexity given the large number of small collisions that result from the long-range Coulomb interaction. For instance, a neutron slowing down in aluminum from 0.5 MeV to 0.0625 MeV will undergo about 30 collisions, while a photon in the same circumstances will experience fewer than 10. On the other hand, an electron will experience the same

energy loss only after 10^5 individual interactions. Because of the computational time, the single-collision Monte Carlo approach would not be useful in most of the cases.

To drastically decrease the computational time, MCNP uses a variety of analytic and semi-analytic multiple-scattering theories for the transport of charged particles. These theories rely on fundamental cross sections and the statistical nature of the transport process to predict probability distributions for significant quantities, such as energy loss and angular deflection. The most important of these theories are the Goudsmit-Saunderson theory for angular deflections [76], the Landau theory of energy-loss fluctuations [77], and the Blunck-Leisegang enhancements of the Landau theory [78]. These theories rely on a variety of approximations that restrict their applicability, and therefore, cannot solve the entire transport problem. In particular, it is assumed that the energy loss is small compared to the kinetic energy of the electron.

In MCNP, all cross sections such as those for energy-loss events, energy straggling events, multiple scattering, knock-on electrons, bremsstrahlung, etc are calculated on a fixed energy grid E_n, n=1,2,3... corresponding to the relation $E_n=E_{n-1}\times$EFAC, where EFAC is 0.917. The EFAC value corresponds to steps with a fixed energy loss of 8.3% of the electron's energy at the beginning of the step. For each step, an average energy loss rate based on a non-radiative stopping power is calculated. Then, fluctuations of this average energy-loss are calculated using the Landau and Blunck-Leisegang theory for energy straggling for every step. The angular deflection is computed for each step using the Goudsmith-Saunderson theory, applicable for an arbitrary angular deflection. To improve the accuracy, MCNP divides each major energy step into smaller substeps. The number of substeps depends on the atomic number Z of the material in which the electron travels, and ranges between

2 for Z=3, to 15 for Z>90. For the quality of the simulations, it is important that an electron makes at least ten sub-steps in any material of importance of the transport problem. At the end of each substep, the outgoing direction of the electron depends on the estimated energy loss rate, the energy at the end of the substep, and the substep path length. On the sub-step scale, appropriate probability distributions for the production of secondary particles (including electron-induced fluorescent X-rays, knock-on electrons from electron-impact ionization, and bremsstrahlung photons) are sampled.

In MCNP, electrons and positrons are described by the same physics, distinguishing the two kinds only in terminal processing. A positron will annihilate when at rest to produce two photons, each with energy $mc^2 = 0.511008$ MeV.

4.5.2 Potential problems of MCNP settings

Specific settings were chosen differently from the MCNP default mode in order to assure an appropriate response to the geometrical resolution necessary to describe DSSD strips ($1\times1\times40$ mm^3) and DSSD single pixels ($1\times1\times1$ mm^3). Several reports have pointed out potential problems in the default MCNP settings when simulating electron transport in a thin layer of a material [79,80].

The first problem pointed out in [79,80] is related to how to update the transport parameters at the beginning of each energy step where the energy loss rate (including straggling) needs to be determined. Because in general the fluctuations of the average energy-loss are large, the actual sequence of electron energies can deviate from the simple sequence E_n=$E_{n-1}\times$EFAC described in Sec.4.5.1. If in any substep the electron energy falls outside of step boundary (E_n,E_{n-1}), the default simulation mode (DBN=0) terminates the current step, and starts a new one deciding the new energy bin based on an interpolation. This procedure is an

attempt to keep the electron in the energy bin closest to its own energy. On the other hand, in ITS mode (DBN=1), each step is always completed. In this mode, the new energy step is chosen as the one whose energy boundaries are as close as possible to the electron's energy resulting from the previous step with no interpolation. [79, 80] report a systematic overestimation of the energy deposition when the default mode is used to simulate electron transport in thin layers.

For our DSSD detector setup, the MCNP response for the two simulations modes is shown in Figure 4.27 for electrons of 1 MeV. In agreement with [79, 80] the default mode resulted in larger energy deposition in the detector, although the effect was not substancial. Thus, relying on the work of [79, 80] the ITS mode was used in the present analysis.

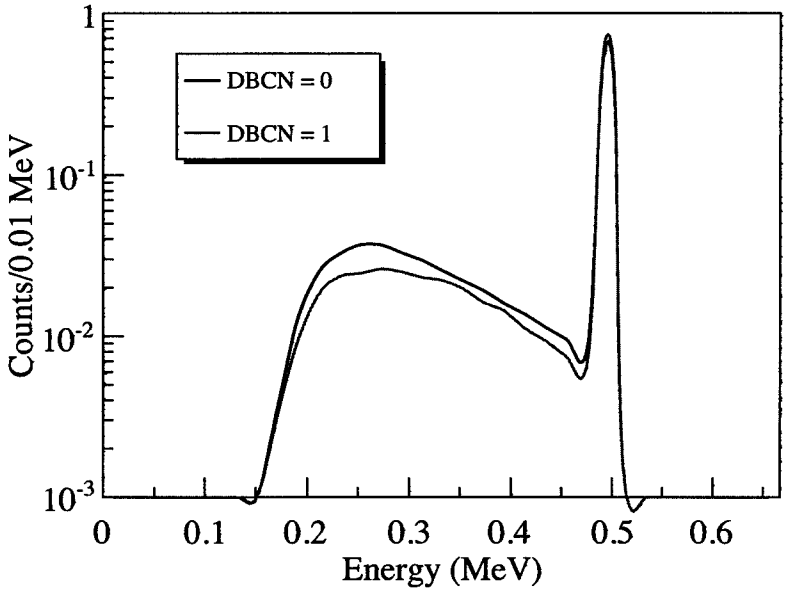

Figure 4.27: Comparison between the energy deposited in the DSSD using the default mode and the ITS mode.

[79] also reported a potential problem in MCNP related to the parameter EFAC, suggesting that the default value (EFAC=0.917) might not be appropriate

for thin layers of material because the number of steps may be too small. For several different values of the EFAC parameter, Figure 4.28 shows the energy deposited by an 1 MeV electron in our DSSD. The MCNP response with EFAC=0.917 is very similar to the one with EFAC=0.93, but a small deviation appears for EFAC larger than 0.95. For our DSSD set-up and EFAC=0.95, an 1 MeV electron makes about 20 substeps[1] during the whole simulation process which is a safe number as argued before. Our simulations did not show a particular sensitivity to the EFAC parameter. Thus, we chose EFAC=0.95 relying on the work of [79]. This choice, increased the computational time compared to the default setting by about a factor of 2.

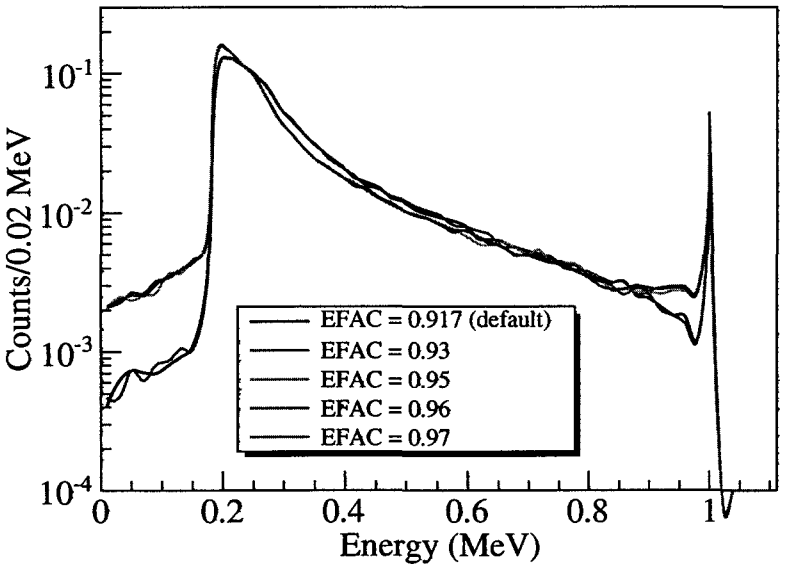

Figure 4.28: Comparison between the energy deposited in the DSSD using the default mode and the ITS mode.

[1]To achieve this we had to set the number of substep per step to 10.

4.5.3 DSSD low-energy calibration

The low-energy calibration of the β-calorimeter detectors is necessary to measure the end-point of the β-energy spectrum (Q_β). This section reports a calibration of the DSSD that extends the ^{228}Th calibration (described in section 4.2.1) towards low energy down to the detector thresholds. The ^{228}Th calibration is not accurate to measure energies deposited by electrons because electrons tend to deposit much less energy than alpha particles (typically less than 1 MeV).

We carried out tests with a DSSD similar to the one used in the BCS (Section 3.3.3) but with a thickness of 500 μm, using electrons from a ^{133}Ba source and low energy β-delayed protons from the decay of ^{20}Mg and ^{23}Si in another NSCL experiment. These tests revealed the presence of a non linearity in the energy calibration of the DSSD at energies below 1 MeV, as shown in Figure 4.29. Therefore, we calibrated our detectors defining two different linear functions, each corresponding to a different energy range. Above 1 MeV (high-energy calibration), we used the linear calibration obtained with the ^{228}Th source, whereas below 1 MeV (low-energy calibration), we used a linear function that crosses the origin and with a slope determined separately for each detector. Figure 4.29 shows that the linear approximation (in red) deviates from the non-linear calibration (in black) by a maximum of 60 keV.

In order to determine the slope of the low-energy linear calibration, we used the following method based on the assumption that for a given detector the low-energy calibration of every strip has the same slope. This assumption is suggested by the high-energy calibrations. After gain match, the slopes of the high-energy linear calibrations of different strips in the same detector deviated from each other by a maximum of 2%. Then, the low-energy calibration slopes were chosen as those minimizing the difference between the experimental and the simulated spectra of

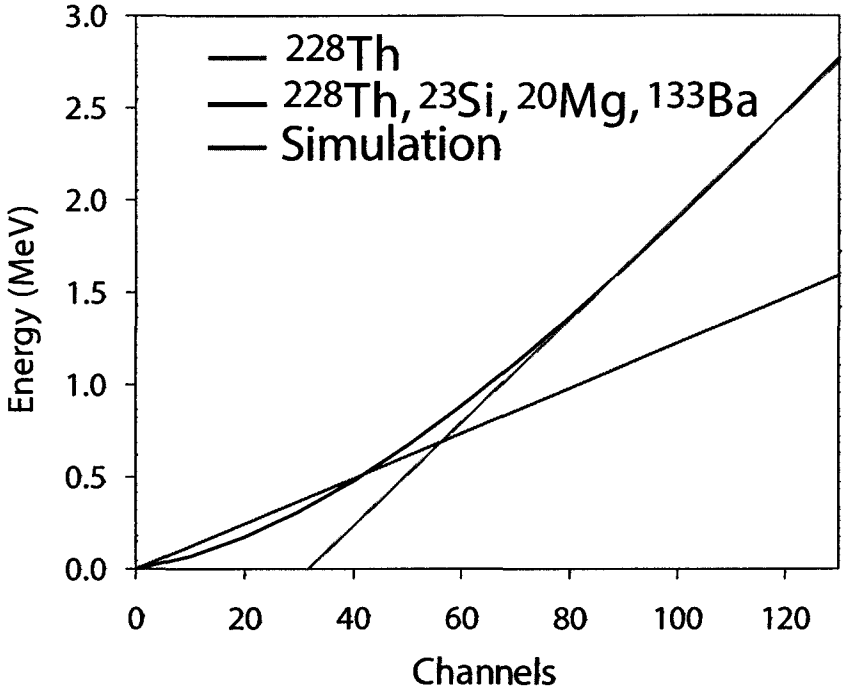

Figure 4.29: Energy calibration of a 500μm DSSD using: a ^{228}Th alpha source (green line), the sources ^{228}Th, ^{133}Ba, ^{23}Si and ^{20}Mg (black curve). The red line is a linear approximation of the black curve for energies below 1 MeV, and it is the calibration used for energies below 1 MeV.

the energy loss of electrons from a ^{90}Sr/^{90}Y source passing through the detector. This was necessary because we did not have available a source of mono-energetic electrons that could be stopped in the detectors. Simulated spectra were obtained within MCNP.

As described in Section3.3.3, our detectors were arranged in a stack. The ^{90}Sr/^{90}Y source was placed in front of the stack. For a given detector, we then considered all different spectra gating only on one detector downstream, gating on two detectors downstream and so on. These different gates effectively provided different energy thresholds and also restricted the direction of electrons contributing to a given spectrum. The slope information for a given detector provided

by the different spectra was redundant. However, the fact that simulations using the same slope reproduce well different spectra validated the simulations and the assumptions of the method.

Figure 4.30 shows the result of the minimization process. The Figure displays the integral of the spectra obtained by subtracting the recorded and simulated spectra as a function of the energy calibration slope. For each detector, there clearly is a narrow range of calibration slopes minimizing the integral. That range is assumed as uncertainty of the slope. The values of the slopes for each detector are reported in Table 4.3. Figure 4.31 and Figure 4.32 show the recorded and the simulated spectra for calibration slopes from Table 4.32; the agreement is satisfactory, with differences possibly stemming from the use of the linear calibration.

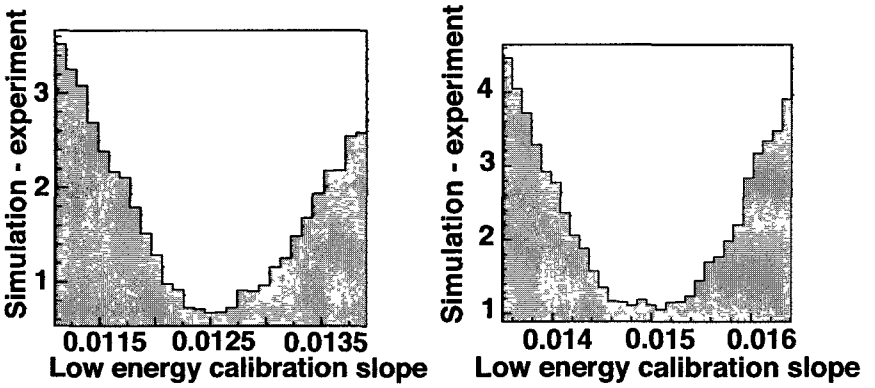

(a) dssd

(b) sssd1

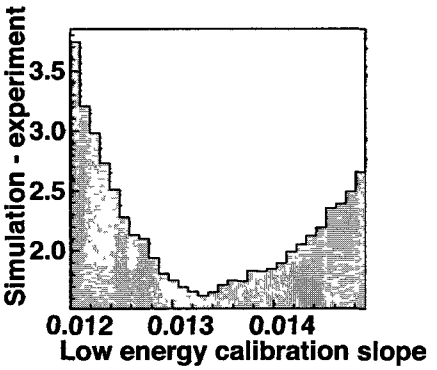

(c) sssd2

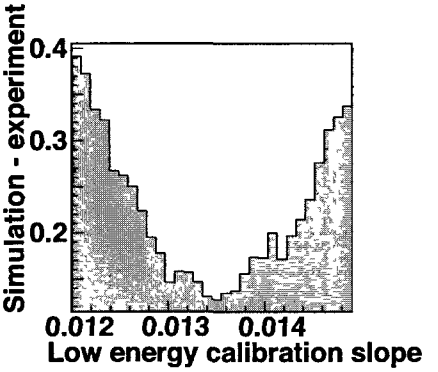

(d) sssd3

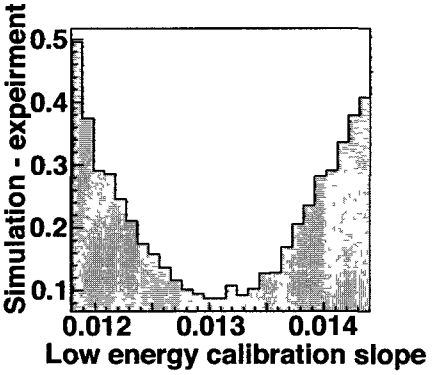

(e) sssd4

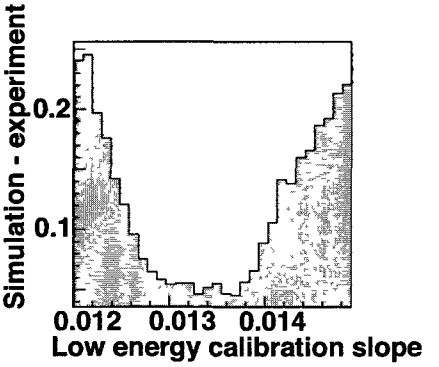

(f) sssd5

Figure 4.30: Minimization of the difference between simulations and experiment. The slope corresponding to the minimum is the one used for calibration.

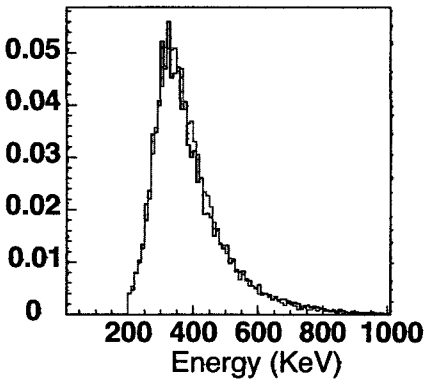

(a) dssd gated on sssd2

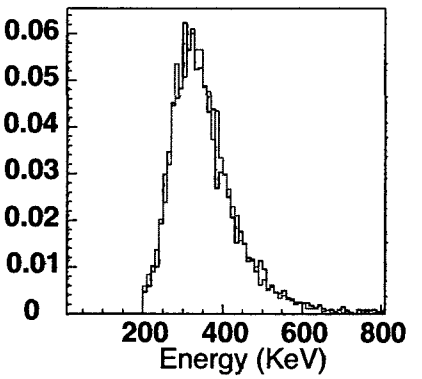

(b) dssd gated on sssd3

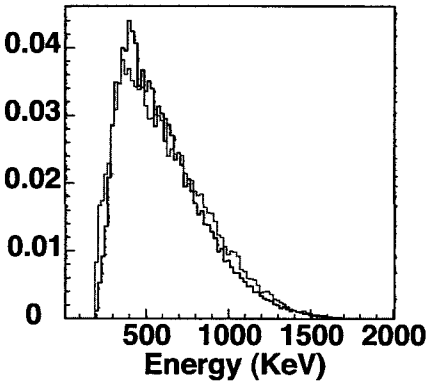

(c) sssd1 ungated

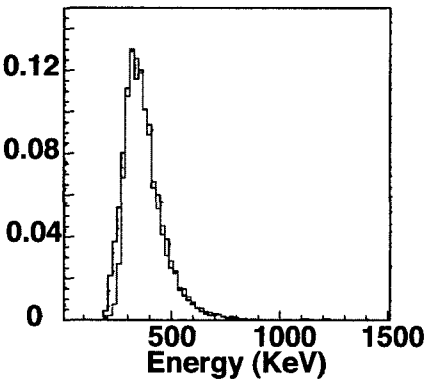

(d) sssd1 gated on sssd3

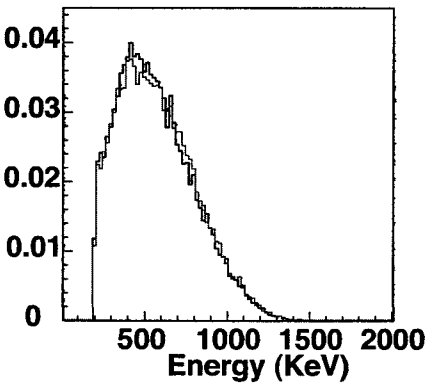

(e) sssd2 ungated

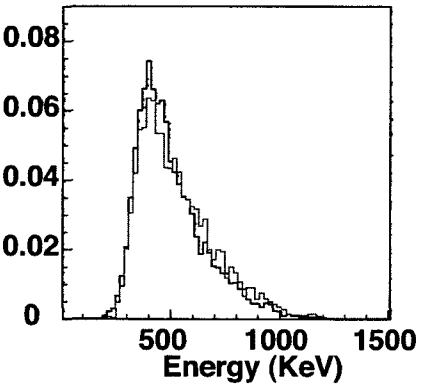

(f) sssd2 gated on sssd3

Figure 4.31: Experimental (black) and simulated (red) Energy deposition spectra by electrons from the β-decay of a $^{90}Sr/^{90}Y$ source for the best energy calibration. The area of all histograms is normalized to unity.

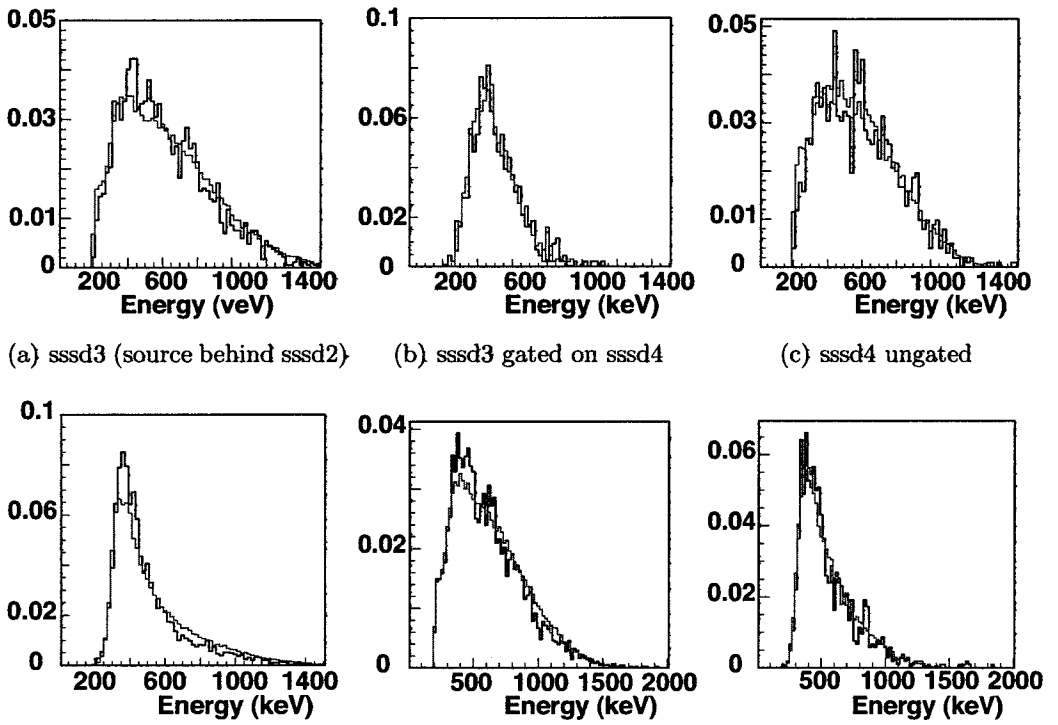

(a) sssd3 (source behind sssd2) (b) sssd3 gated on sssd4 (c) sssd4 ungated

(d) sssd4 gated on 5 (e) sssd5 gated on sssd5 (f) sssd5 gated on sssd6

Figure 4.32: Experimental (black) and simulated (red) Energy deposition spectra by electrons from the β-decay of a $^{90}Sr/^{90}Y$ source for the best calibreation. The area of all histograms is normalized to unity.

Table 4.3: Slope of the low-energy linear calibration

Detector	Low energy calibration slope MeV/Channel
DSSD	0.0125(2)
SSSD1	0.0150(4)
SSSD2	0.01335(5)
SSSD3	0.0133(1)
SSSD4	0.01310(2)
SSSD5	0.01320(3)
SSSD6	0.01300(1)

4.5.4 Simulation of the calorimeter response

The β-decay energy spectrum for allowed β decays is described by:

$$N(p) \propto p^2 \, (Q - T_e)^2 \;\; F(Z,p) \tag{4.17}$$

where Q is the end-point of the electron energy T_e, F(Z,p) is the Fermi function, p is the electron momentum, and N(p) is the shape of the probability distribution. This equation shows that plotting $\sqrt{N(p)/p^2 F(Z,p)}$ as a function of T_e yields a straight line (known as the Curie plot) intercepting the T_e axis at the decay energy Q. Such a linear plot offers a convenient way to determine the endpoint energy Q.

However, in reality, the measured energy spectrum in our calorimeter will be different from the intrinsic β spectrum of the decay for at least two reasons: a) because our β-calorimeter does not cover the 4π solid angle, and hence some particles will escape the calorimeter, depositing only a fraction of their energy; and b) because of the energy resolution of the calorimeter. We performed simulations to asses the impact of these two effects on the Curie plot.

Calorimeter efficiency

The β-calorimeter consists in a stack of six SSSDs in a close configuration at about 2 mm from each other, sandwiched between the DSSD detector and a thick Ge-detector 5 cm apart. The overall efficiency strongly depends on a) the geometry of the stack, b) scattering phenomena , and c) the effect of thresholds. MCNP was used to determine the effect of the first two factors. It was found that electrons with energy higher than 3 MeV can not be stopped by the SSSD stack and that the calorimeter would be able to stop 13% of these 3 MeV electrons. For energies higher than 3 MeV, the last bit of the calorimeter –the Ge detector– is needed. It can stop electrons of energy 14 MeV, but the geometrical efficiency drops to 3%.

Energy resolution

The blue spectrum in Figure 4.33 is a simulation of the energy deposited in the calorimeter by electrons from a β decay with a Q value of 2200 keV. As expected, the spectrum is linear above $\sim$2 MeV, and with a linear fit one obtains the correct Q value. However, when the finite detector energy resolution of about 50 keV per detector is included in the simulations, the resulting spectrum is distorted. The high-energy part is still linear, but with a modified slope shifting the end-point energy towards higher values. Thus, in the case represented in Figure 4.33, the detector's energy resolution introduces a systematic uncertainty of about 100 keV in the measurement of the endpoint value. This systematic uncertainty depends on the number of detectors employed to stop the electrons, and hence it is higher for higher Q values.

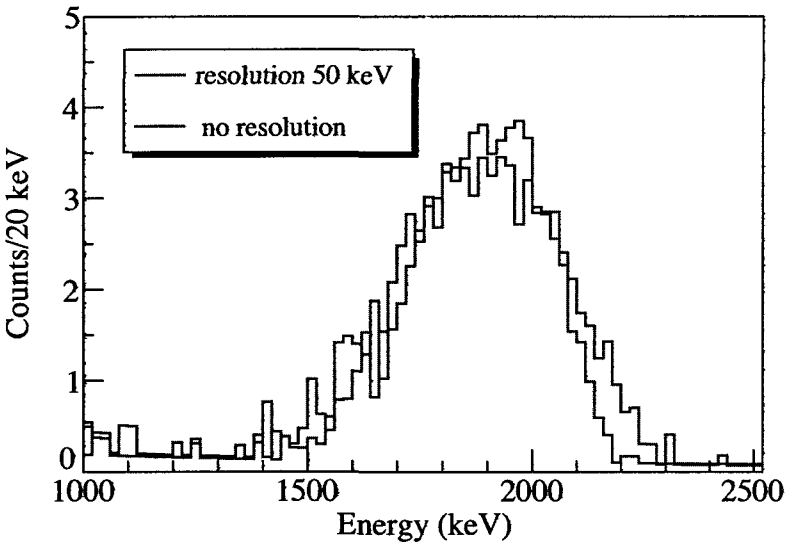

Figure 4.33: MCNP simulations of the calorimeter response including and excluding the finite energy resolution of individual detectors.

Shape of the energy deposited spectrum

Based on the discussion in this section, is it evident that the energy deposited in the calorimeter is indeed linear at high energy, but the fit of the linear part of the spectrum has to take into account a correction for the energy resolution that can be calculated using simulations.

The nuclei of interest in this experiment have high Q-values ranging between 8-12 MeV. For such energies, the Ge detector of the calorimeter is needed to stop electrons. However, although the calorimeter has enough material to stop 14 MeV electrons, during the experiment the gain of the Ge-detector amplifier was optimized for ^{100}Sn. As a result, signals with energy above 3 MeV were overflowing the ADCs (see Section 4.2.2). This is illustrated in Figure 4.34. Some 8 MeV electrons –those depositing a large amount of energy in the SSSD stack–would still be detected, but the linearity at high energy is lost above 5 MeV. This leaves only about 2 MeV for a linear fit, which is not sufficient for accurate results. Therefore,

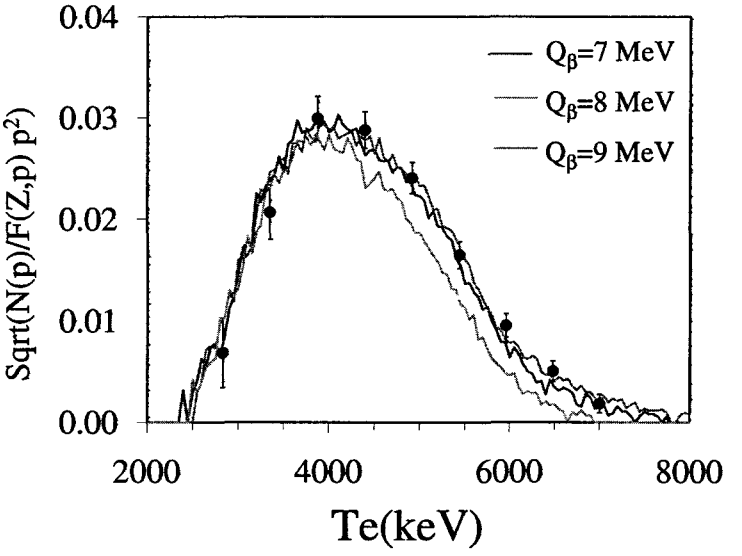

Figure 4.34: Comparison between the experimental total energy deposited in the calorimeter (black points) for the decay of ^{96}Ag, and simulations performed using different Q values.

the Curie plot could not be used for our analysis. The sensitivity of the calorimeter energy deposition spectrum was studied in detail, hoping that the spectrum shape could still be sensitive to the Q values, but as Figure 4.34 shows, this attempt failed because decays with Q values above 7 MeV were not distinguishable in our set up. In summary, our calorimeter was only able to measure β-endpoints up to 3 MeV. There was only one case where this was sufficient to carry out a measurement, and it consisted in the electrons from the ^{90}Sr/^{90}Y source with a known Q value 2279.8(1.7) keV. The measurement of this Q value was performed to test the low-energy calibration of the detectors and for testing the response of the calorimeter to low Q values. The corresponding energy spectrum is shown in Figure 4.35. The extrapolated end-point energy is Q=2360^{+120}_{-50} keV, which is consistent with the known value 2279.8(1.7) keV after correcting for resolution, as explained in the previous subsection 4.5.4.

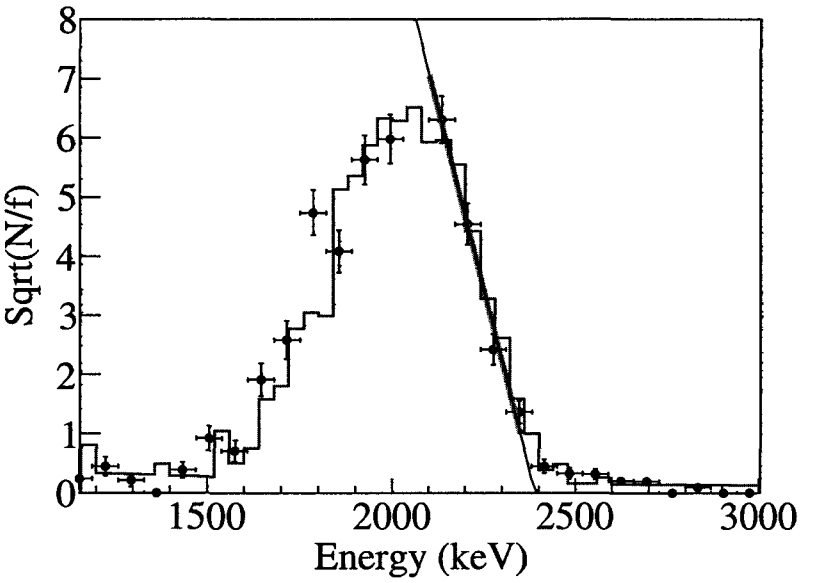

Figure 4.35: (color on line) Curie plot of the energy deposited in the β-calorimeter for the events in which the DSSD, SSSD1, SSSD2, SSSD3, and SSSD4 detect a particle. A simulation for these events is represented by the red histogram. The extrapolation of the linear fit of the spectra performed in the range highlighted in green allows Q-value determination.

Chapter 5

Results

5.1 Experimental results

In Chapter 3, we have described how the nuclei implanted in the BCS were identified based on the determination of their atomic number Z and their mass to charge ratio A/Z. In Chapter 4, we detailed the analysis of the position correlation and time correlations that enabled us to assign a detected proton to a specific implanted nucleus. The correlation process led to the identification of 10 β-delayed proton precursor identified among the implanted one as illustrated in Figure 5.1. This chapter reports the results from the experiment for the these 10 isotopes. For each isotope, several results are described. We report the half-life extracted form the decay curves. For βp-decay events, energy spectra and β-delayed proton emission branching ratio are measured. Finally, we include the gamma spectra in coincidence with protons. All the measurements are briefly compiled at the end of the chapter in Table 5.3 including a comparison with literature.

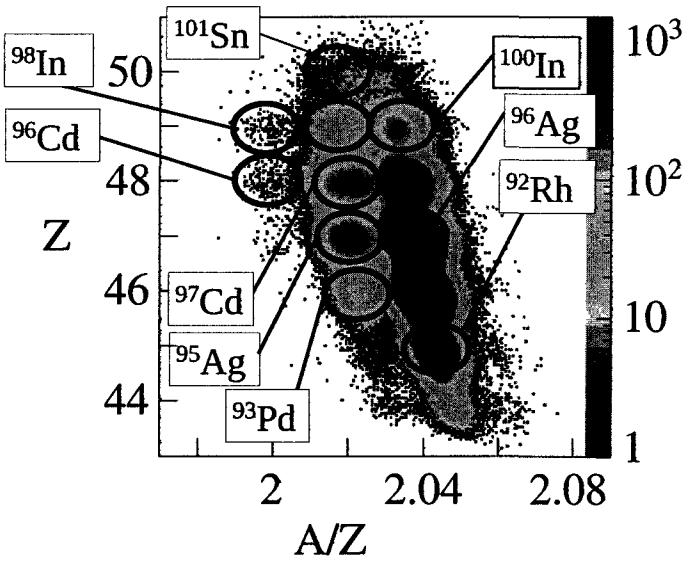

Figure 5.1: Particle identification plot. The labeled nuclei are the βp-emitters identified in this work.

5.1.1 βp-decay of ^{101}Sn

Having just one additional proton compared to doubly magic ^{100}Sn, ^{101}Sn is of particular interest to probe the single particle level structure in this region. Recently, [12] identified a γ-ray transition of 172 keV in an in-beam experiment tagging on β-delayed protons from ^{101}Sn and assigned it to the deexcitation of the first excited $7/2^+$ state to the $5/2^+$ ground state, therefore representing the $g_{7/2}$ $d_{5/2}$ single particle level spacing. The same transition has also been observed in the α-decay measurements of the chain ^{109}Xe$\rightarrow$^{105}Te$\rightarrow$^{101}Sn [7], indicating an opposite level ordering with a $5/2^+$ excited state and a $7/2^+$ ground state. Shell model calculations can reproduce both orderings [40]. The β-decay of ^{101}Sn can in principle shed light on this question by constraining the ground state spin of ^{101}Sn. Several β-decay studies of ^{101}Sn have been carried out in the past [39, 40, 81]. We detect a total of 2000 βp-events from ^{101}Sn. Our half life of 2.1(3) s obtained from the βp-events agrees well with the previous weighted average of 1.9(3) s resulting

in a new weighted average of 2.0(2) s.

Our $P_{\beta p}$=20(1) % agrees with the only previous measurement ($P_{\beta p}=14^{+15}_{-10}$ % [39]) but is much more precise.

The β-delayed gamma spectra observed is shown in Figure 5.2. No gamma lines were detected besides background. Instead we find four counts of a γ line at

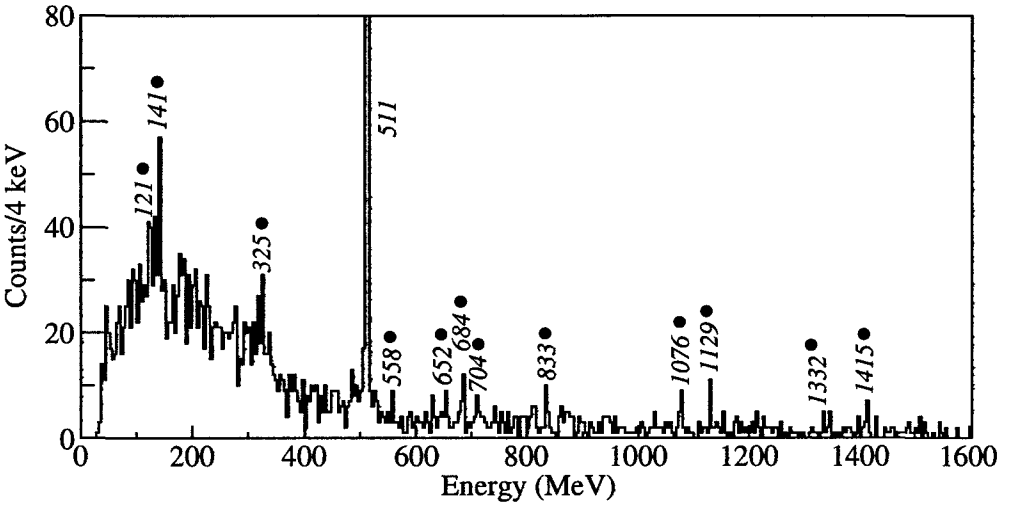

Figure 5.2: β-delayed γ ray spectra from the decay of ^{101}Sn. All the main observed peaks were attributed to background (labeled with a full circle)

1004 keV observed in coincidence with proton events. This peak, shown in Figure 5.3 is most likely the de-excitation of the known first 2^+ state in ^{100}Cd, fed by the βp-decay of ^{101}Sn. We do not see evidence for the 794 keV $4^+ \rightarrow 2^+$ transition, maybe indicating some direct feeding of the 2^+ state.

5.1.2 βp-decay of ^{98}In

^{98}In was first produced and studied in a fragmentation experiment which revealed the contribution of two β-decaying states with half-lives of 32^{+32}_{-11} ms and $1.2^{+1.2}_{-0.4}$ s respectively [82].

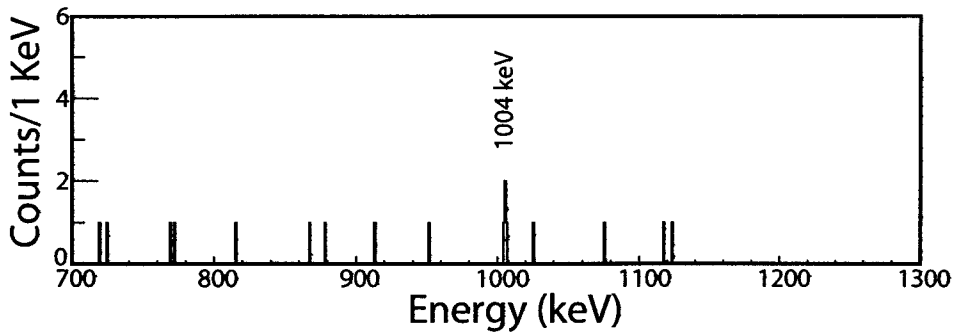

Figure 5.3: 700-1300keV section of the measured γ spectra in coincidence withe β-delayed protons from the decay of ^{101}Sn. The labeled peak corresponds to the know de-excitations in the βp-daughter ^{100}Cd $2^+ \rightarrow 0^+$ at 1004 keV

The short component was attributed to the super-allowed Fermi decay from the 0^+ ground state. The analysis of the β-decay of this nucleus in our experiment confirms the observation of two time components with half-life 47(13) ms, and 0.66(40) s [66]. We present here in addition the analysis of β-delayed proton emission from ^{98}In observed for the first time. The time distribution of 63 βp events confirms the presence of two time components (see Figure 5.4) with half-lives of 135(65) ms and 1.27(30) s, and with branchings of $P_{\beta p}=5.5^{+3}_{-2}$ % and 19.5(13) % for the ground state and the isomeric state respectively. For the isomeric state, our βp half-life is more precise than the half-life reported in [66] because the limitation on proton events reduces the background and eliminates daughter decay contributions.

5.1.3 βp-decay of ^{97}Cd

One of the goals of this experiment was to search for isomeric states in ^{97}Cd. Various shell model calculations agree in predicting two isomeric states, a $1/2^-$ state below 1 MeV, and a $25/2^+$ state at about 2.4 MeV [1, 2]. Both states are

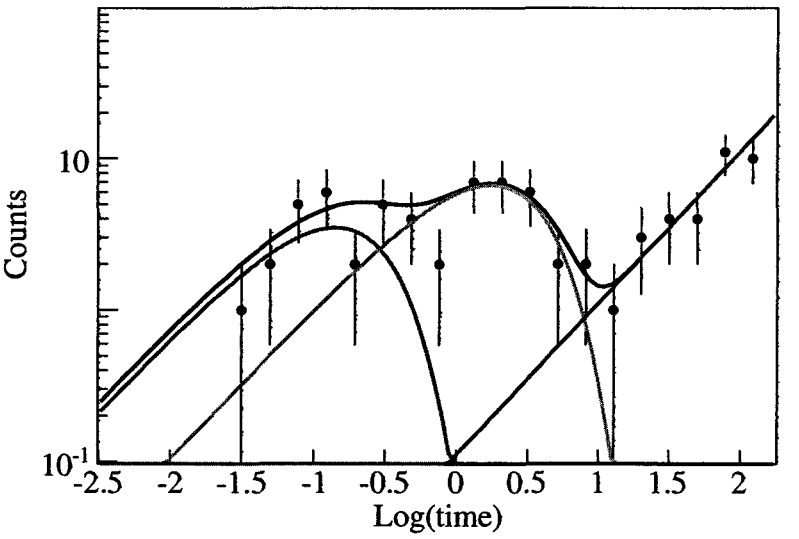

Figure 5.4: Decay curve and fit for the βp-decay of ^{98}In displayed with a logarithmic time binning. The contributions from the ground state (blue), isomeric state (green), background (red), and their sum (black) are shown.

predicted to have size-able β-decay branches, and given the expected large Q-S_p window, both should exhibit β-delayed proton emission.

In this work, more than 10000 βp-events were correlated to implantations of ^{97}Cd. The decay curve of these events in Figure 5.22 shows unambiguously the contribution of two time components with half-lives of 1.0(1) s and 3.8(2) s. There is no evidence for a third component. The existence of two components is confirmed by the analysis of βp delayed γ rays. Figure 5.8 shows the γ spectrum recorded in coincidence with βp-activity from ^{97}Cd. Feeding of the known $12^+ \rightarrow 10^+ \rightarrow 8^+ \rightarrow 6^+ \rightarrow 4^+ \rightarrow 2^+ \rightarrow 0^+$ cascade in the daughter ^{96}Pd can be clearly identified via $\gamma\gamma$ coincidences (see Figure 5.7). The decay curves for each γ transition are shown in Figure 5.9, and the resulting half-lives are listed in Tab. 5.1 again confirming the existence of two decay components. The transitions $12^+ \rightarrow 10^+ \rightarrow 8^+ \rightarrow 6^+ \rightarrow 4^+ \rightarrow 2^-$ are fed mainly by the longer lived decay component. The 1415 keV $2^+ \rightarrow 0^+$ transi-

tion clearly has a shorter half-life of 2.92(15) s. As the long lived $12^+ \rightarrow 10^+ \rightarrow 8^+ \rightarrow 6^+ \rightarrow 4^+ \rightarrow 2^+$ cascade has to decay through the $2^+ \rightarrow 0^+$ transition, this points to a second short lived component feeding the 2+ state. Indeed, a two component fit does improve the decay curve fit for short times significantly (see Figure 5.5).

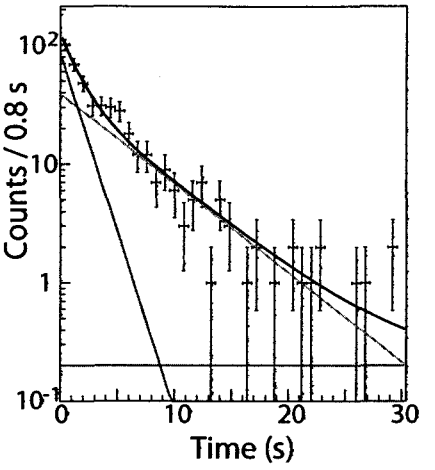

Figure 5.5: Fit of the decay curve of the β-decay events recorded in coincidence with γ rays of 1415 keV using two exponential components with half-lives fixed to the values 4.0(17)s and 1s. A constant background component included in the fit.

High spin states up to 12^+ are expected to be fed mainly by β-delayed proton emission from the $25/2^+$ high spin isomeric state in ^{97}Cd. We therefore assign the half-life of 3.8(2) s to the decay of the predicted $25/2^+$ isomeric state in ^{97}Cd. This half-life is somewhat larger than the 0.6 s predicted by shell model calculations.

In principle, the shorter lived component could originate from the ^{97}Cd ground state, or the predicted $1/2^-$ isomeric state. To shed light on this question we examine the γ ray spectrum recorded in coincidence with β-particles shown in Figure 5.11. The γ lines at 260, 290, 764, 1289, 1306, 2572 keV are part of a known cascade deexciting high lying states in the ^{97}Ag daughter nucleus [83]. The intensities of these γ lines, indicate that the feeding is predominantly through

the $25/2^+$ level at 6221 keV and the $23/2^+$ level at 4915 keV, with about 50% of the decay unobserved. The decay curves gated on these γ lines, for the cases with enough statistics, are shown in Figure 5.11. The corresponding half-lives are compatible with 3.8(2) s. Because of the feeding at high spin, and the half-life being consistent with the long lived decay component, we assign these γ-rays to originate from the β decay of the high spin isomer in ^{97}Cd. However, there is one additional γ ray at 717(2) keV (see Figure 5.10), which does not occur in coincidence with any other transition. The decay curve of this line is shown in Figure 5.12. The corresponding half-life of 1.1(2) s is significantly shorter compared to the other β delayed γ rays and is compatible with the short lived decay component of ^{97}Cd of 1.0 s. This γ ray is most likely associated with the β-decay of the shorter lived ground state of ^{97}Cd (presumably $9/2^+$) feeding the first excited $7/2^+$ state in ^{97}Ag. This state is predicted at an excitation energy of about 700 keV [2] and is expected to decay to the ground state.

It is unlikely that the 717 keV line is associated with the β-decay of the $1/2^-$ isomeric state in ^{97}Cd. This decay would likely feed the predicted low lying $1/2^-$ state in ^{97}Ag. Ref. [2] discuss two possible scenarios based on two different shell model calculations. One calculation predicts the $1/2^-$ state to lie above the $7/2^+$ state, its relatively fast decay (half-life 16 ms) feeding the $7/2^+$ state and the ground state. In this case, the 700 keV line from the deexcitation of the $7/2^+$ ^{97}Ag state would also be expected from the β decay of the $1/2^-$ isomer in ^{97}Cd, but it should be accompanied by a $\approx$ 300 keV line from the possible E3 transition $1/2^- \rightarrow 7/2^+$ in ^{97}Ag, and a weaker $\approx$ 1 MeV line from the deexcitation of the $1/2^-$ state to the ground state. We do not see any evidence for these transitions. The 300 keV transition is expected to be highly converted. However, a search for internal conversion electrons was also unsuccessful. Another shell model calculation

predicts the $1/2^-$ state in ^{97}Ag to lie below the $7/2^+$ first excited state. In this case, the $1/2^-$ state can only decay via a slow M4 transition to the ^{97}Ag ground state, extending the decay time by several seconds. Assigning the 717 keV line to the decay of the $1/2^-$ state in ^{97}Ag in this scenario is therefore inconsistent with our measured short half-life for this line. We therefore tentatively assign the shorter 1.10(8) s half-life to the ground state decay of ^{97}Cd. This is consistent with shell model calculations predicting of 0.9—1.1 s [2].

No clear evidence is found for the $1/2^-$ isomer in ^{97}Cd. There are a number of possible explanations. First, it might not be significantly populated in the fragmentation reaction. Second, it might predominantly decay electromagnetically - one shell model calculation predicts only a 16% β branch. If the half-life is longer than $20\mu s$ we would not be sensitive to the delayed γ rays. Third, while we present some arguments for our short lived component arising mainly from ^{97}Cd ground state decay, the evidence is far from conclusive. Therefore, the possibility that the $1/2^-$ isomer has a half-life comparable to the ground state and that our short lived component is a mixture of two very similar half-lives cannot be excluded with certainty.

Similarly to the case of ^{96}Ag, the comparisons of the relative contributions from ground and isomeric state decays to the βp and β activity allows one to extract $P_{\beta p}$ and the relative population for each state: First we fit the βp decay curve to determine the half-lives of the two states and their relative contribution to the β-delayed proton activity. With the half-lives fixed we then fit the β-decay curve and obtain the relative contribution of the two states to the β-decay activity. The contribution from the $25/2^+$ isomeric state extracted in this way is consistent with the intensity of the 764 keV and 1290 keV γ rays , which likely fed only the decay from the isomeric state. We find a relative production of the isomeric state in the

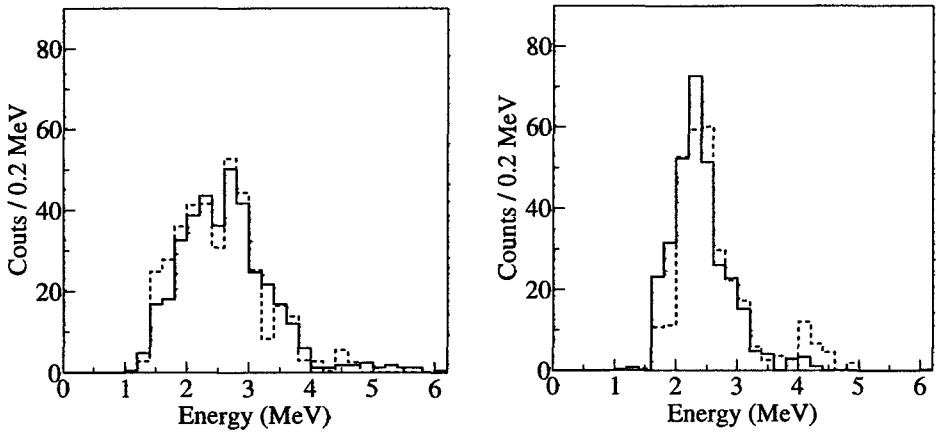

Figure 5.6: Energy spectrum of βp-decay events stemming from the decay of (a) the $25/2^+$ isomeric state observed in this work (solid-line histogram), and the βp-activity observed in [2] (dashed-line histogram). An offset of about 300 keV was applied to the latter spectrum to match our data (b) the $9/2^+$ ^{97}Cd ground state observed in this work, and compared to a shell model prediction (dashed line) [2].

primary fragmentation reaction of 47(10)%, and a $P_{\beta p}$ of 11.8(20)% and 25(4)% for the ground state and isomeric state, respectively.

With our data we were able to extract the energy spectra of the β-delayed protons from the ground state and the $25/2^+$ isomeric state in ^{97}Cd separately (see Figure 5.6(a)). We obtained the spectrum for the isomeric state from the activity observed between 5 and 20 s following the implantation of ^{97}Cd. At such late times no contribution from the 1.1 s component is expected. The ground state spectrum was then obtained by subtracting the isomeric contribution from β-delayed protons during the first 2 s following an implantation, taking into account the relative population and half-lives. The proton spectrum from the ground state is substantially narrower than the spectrum from the isomeric state. Figure 5.6(a) shows that the spectrum from the isomeric decay, and not the spectrum from the ground state, matches the spectrum obtained in [2] indicating that the isomeric state decay dominated in that experiment. On the other hand, the ground state

spectrum is in excellent agreement with the shell model calculations reported in [3].

In an attempt to constrain the excitation energy of the $25/2^+$ isomeric state in ^{97}Cd we can add the end point of the proton energy spectrum recorded in coincidence with the γ-lines at 790 and 1250 keV to the excitation energies of the respective states. Together with estimated ^{97}Ag proton separation energy of 1.880(35) MeV [84] one obtains an excitation energy of about 10 MeV of the highest lying proton decaying states in ^{97}Ag. Using an estimated β-decay Q-value for ^{97}Cd of 10.2(5) MeV [84] this translates into a lower limit for the excitation energy in ^{97}Cd of about 1.3(7) MeV, providing a compatible with the predicted value 2.4 MeV [2].

Table 5.1: Experimental half-lives of selected γ rays from the depopulation of states with spin and parity J in ^{96}Pd* fed by the βp-decay of ^{97}Cd

Energy of ^{96}Pd level (keV)	J	gamma energy (keV)	Half-life s	$I_{\beta p}$(%)
4573	12^+	790	3.5(4)	22(3)
3783	10^+	1250	4.0(3)	52(6)
2530	8^+	106	3.6(3)	¡7
2424	6^+	325	3.5(2)	13(6)
2090	4^+	684	3.65(25)	17(6)
1451	2^+	1415	2.29(15)	67(16)
Energy of ^{97}Ag level (keV)				I_{β}(%)
6221	(27/2+)	1306		24
4915	(23/2+)	2575		24
2343	(21/2+)	290	3.75(60)	0
2053	(17/2+)	763	3.8(6)	0
1290	(13/2+)	1209	3.85(70)	0
717	(7/2+)	717	1.1(2)	20(3)

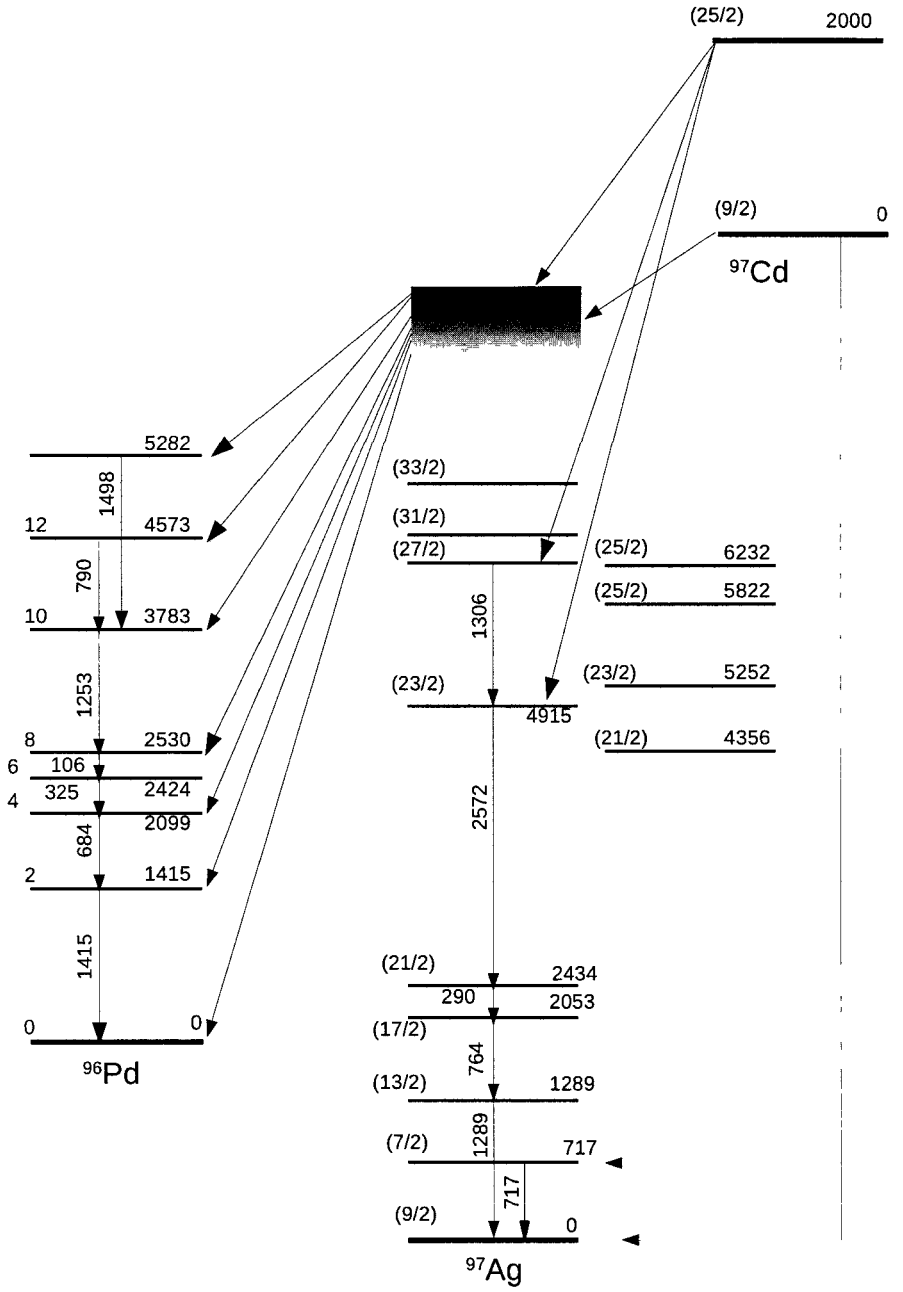

Figure 5.7: Excited states in ^{96}Pd and ^{97}Ag populated by βp-emission of ^{97}Cd. Intermediate unresolved levels in ^{97}Ag are indicated by a gray box. The level energies are drawn to scale. The spin parity assignments are based on previous work [83].

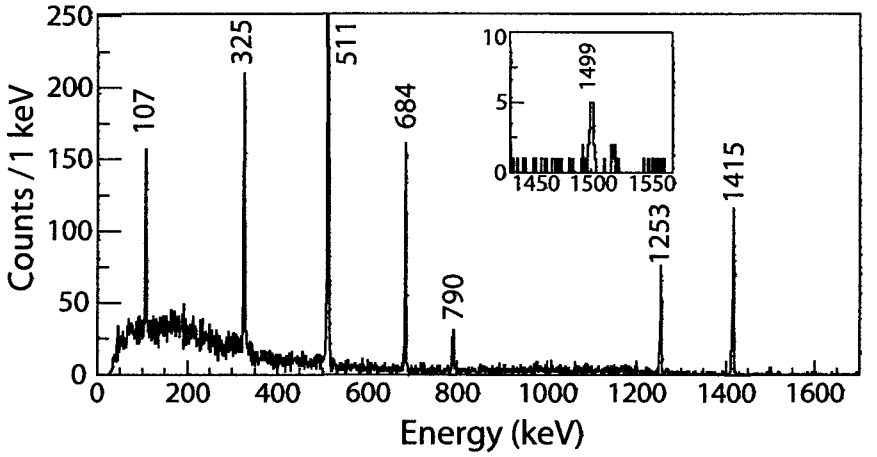

Figure 5.8: Section of the γ spectrum recorded in coincidence with β-delayed protons from the decay of ^{97}Cd. Besides the positron annihilation peak at 511 keV, the peaks shown, originate from the γ decay of excited states in ^{96}Pd populated by the βp-decay of ^{97}Cd. The peaks constitute a $12^+ \rightarrow 10^+ \rightarrow 8^+ \rightarrow 6^+ \rightarrow 4^+ \rightarrow 2^+ \rightarrow 0^+$ cascade. The inset shows a weak peak at 1499 keV which corresponds to the γ decay of a state in ^{96}Pd at 5282 keV with unassigned spin, into the 10^+ state.

5.1.4 βp-decay of ^{96}Cd

^{96}Cd is a possible waiting point in the astrophysical *rp*-process and might also be a progenitor for the synthesis of the p-nucleus ^{96}Ru in the rp process [64,85]. The first half-life measurement of $1.03^{+0.24}_{-0.21}$ s from our experiment was reported in [66].

For the analysis of β delayed proton emission from ^{96}Cd we use the probability weighted particle identification from [66] that takes into account the small overlap of ^{96}Cd and ^{97}Cd in time-of-flight, owing to the momentum spread of the beam. In order to account for a possible contamination from the decay of ^{97}Cd, the βp decay spectrum (see Figure 5.13) was fitted with an additional exponential component with a half-life of 2.21 s corresponding to the average βp decay half-life for ^{97}Cd obtained in this work. The amplitude of this component was determined from the calculated number of ^{97}Cd contaminants and the $P_{\beta p}$ for ^{97}Cd from this work. The ^{96}Cd half-life was fixed at 1.03 s obtained from the β decay data with higher

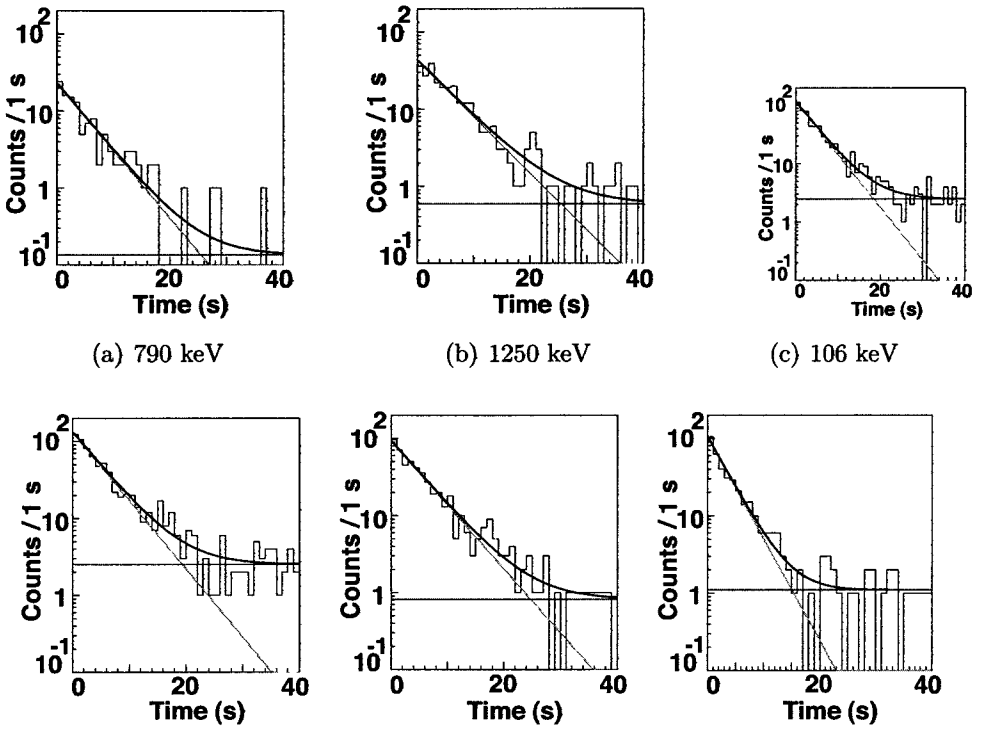

(a) 790 keV (b) 1250 keV (c) 106 keV

(d) 325 keV (e) 684 keV (f) 1415 keV

Figure 5.9: Decay curves recorded for the βp-activity of 97Cd observed in coincidence with selected γ rays from the depopulation of ^{96}Pd* levels

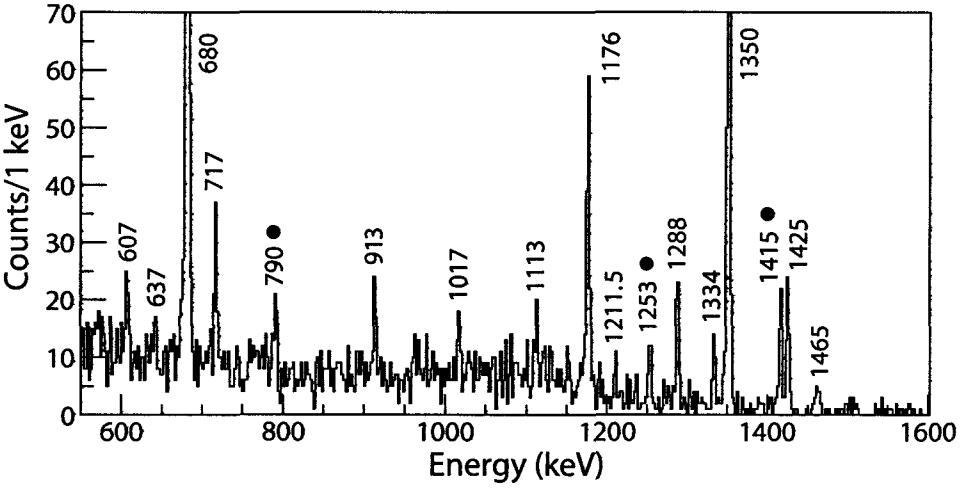

g

Figure 5.10: Section of the γ spectrum recorded in coincidence with ^{97}Cd β-decay events. It shows an important γ peak at 717 keV which can possibly stem from the β-decay of the ^{97}Cd ground state. The other two labeled peaks: 684, and 763 keV in the figure correspond respectively to a contamination from the β-decay of ^{96}Ag, and the de-excitation of the $17/2^+$ state in ^{97}Ag, populated by the β-decay of the ^{97}Cd high spin isomeric state.

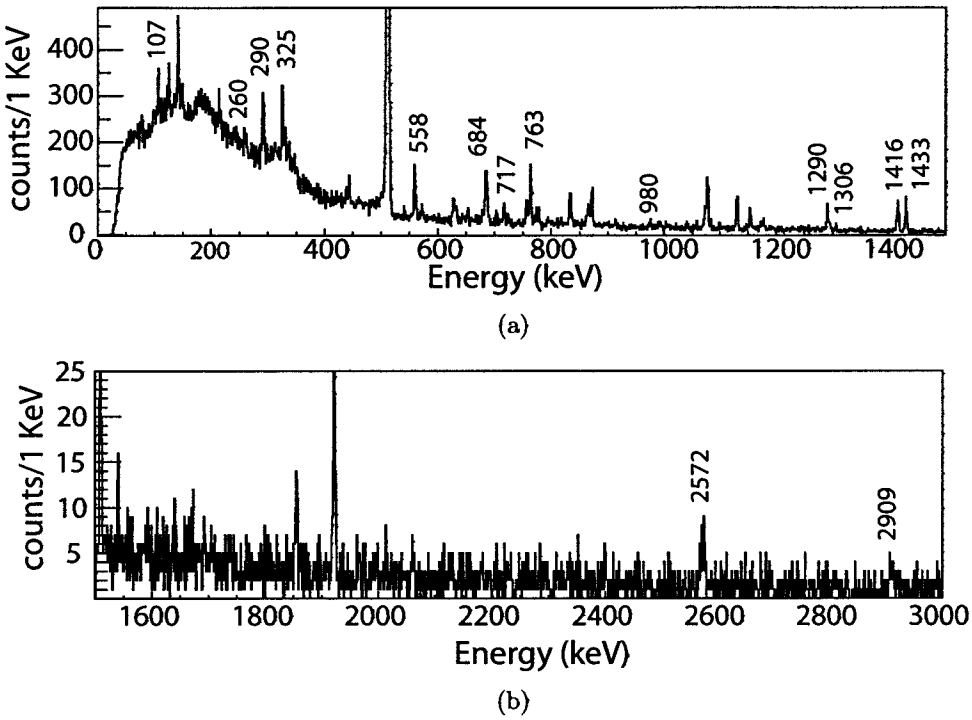

Figure 5.11: Section of the γ spectrum recorded in coincidence with ^{97}Cd β-decay events.

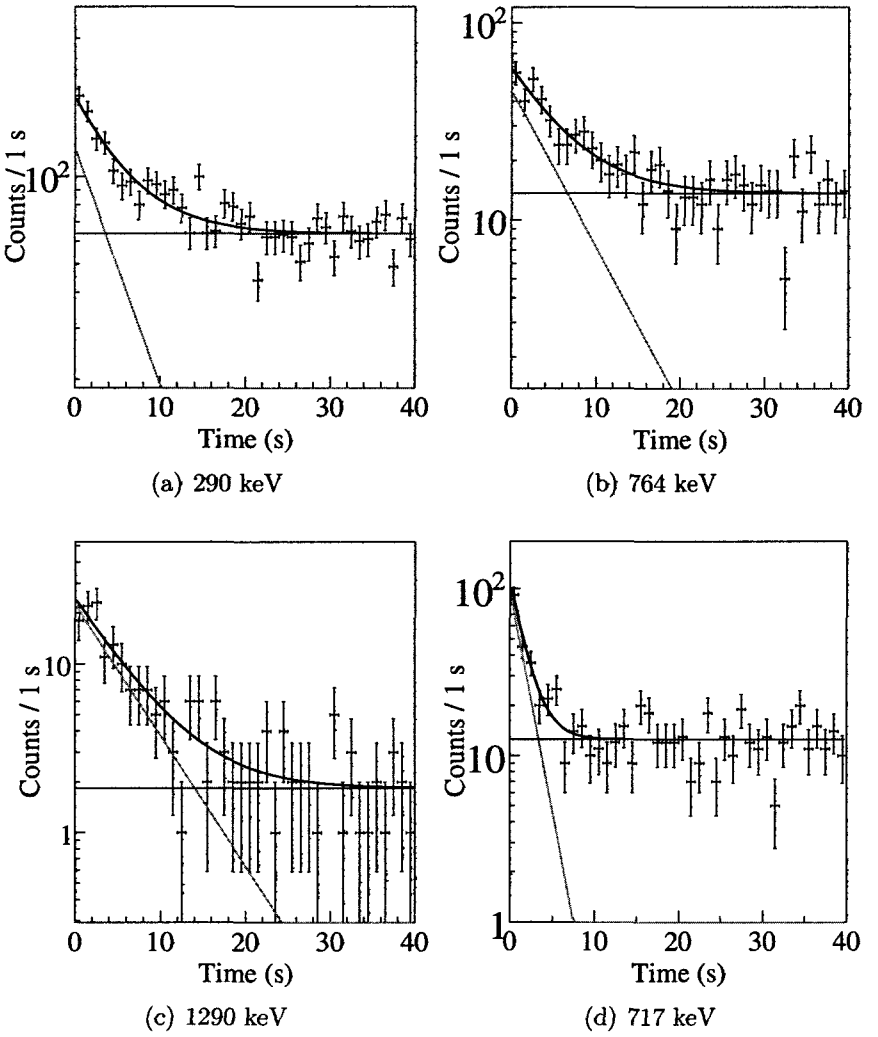

Figure 5.12: Decay curves recorded for the β-activity correlated to implantations of ^{97}Cd in coincidence with selected γ rays from the depopulation of levels in the daughter nucleus ^{97}Ag*

statistics. The analysis was performed multiple times for classes of events with at least 10% (241 events), 30%, 50%, and 95% probability to be ^{96}Cd, respectively, resulting in consistent $P_{\beta p}$ values confirming the correct treatment of the ^{97}Cd contamination. The most precise result of $b_{\beta p} = 5.5(40)$ % is obtained from the events with 50% probability. The error includes uncertainties in the half-lives of ^{96,97}Cd, in the $P_{\beta p}$ value of ^{97}Cd, and in the contamination level of ^{97}Cd.

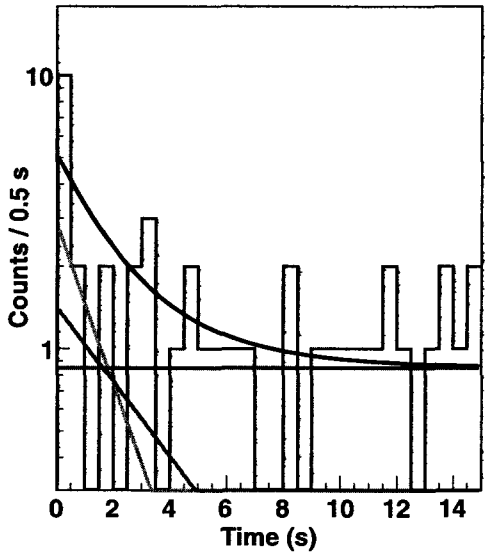

Figure 5.13: decay curve and fit for the βp-decay of ^{96}Cd. The contribution of ^{96}Cd (green), contamination of ^{97}Cd (blue), background (red), and their sum (black) are plotted.

5.1.5 βp-decay of ^{96}Ag

^{96}Ag is known to have two low lying β decaying states, one being the ground state and one an isomeric state. Based on their experimental $\beta\gamma$ data [3] determined individual half-lives of 4.40(6) s and 6.9(6) s, and the decay scheme shown in Figure 5.14. They used of a total absorption spectrometer (a single NaI crystal with about 100% efficiency for γ rays) allowing them to directly observe the two states. As can

be understood from Figure 5.14, the observation of the γ at 1415 keV in coincidence or anti-coincidence with any of the γ at 106, 325 and 684 keV identifies respectively the short and long-lived components, which are assigned with the tentative spins 8^+ or the 2^+ state based on systematics and shell model calculations. In the same experiment, individual branching for β-delayed proton emission of 8.5(15)% and 18(5)%, and, were also determined from the two component fit of the βp-activity.

In our experiment, we could isolate the short-lived state gating on the gamma rays at 106, 325,684 keV. In this way we determine the half-life 4.395(85) s.

Figure 5.15 shows the energy spectra of the βp-events generated from the the decay of ^{96}Ag. As already discussed in section 4.3.1, it agrees very well with [3]. The study of the time distribution of this βp-activity is shown in Figure 5.16. Here, the time distribution is fit using besides a background component, one exponential (Figure 5.16(a)) and two exponential components (Figure 5.16(b)). The half-life obtained with a single time component agrees well with [2] who could not distinguish the two components. Our statistics is also not sufficient to extract two time components from a decay curve fit. However, if we fix one half-life to 4.395 s, as determined from the gamma-ray time distribution, then the data require a second component, for which we obtain a half-life of 6.7(4) s. The error includes the statistical error from the fit, and the systematic uncertainty due to the fixed short-lived component. For this half-life, the error includes the statistical which result from the fit, and the systematic uncertainty due to he fix short lived-component. The same fit provides the relative contribution of the two decaying ^{96}Ag states to the β-delayed proton activity. The relative contributions of the states to the β activity can be obtained by comparing the intensities of the β-delayed 325 keV γ rays mainly fed by the β-decay of the shorter lived state, to the intensity of the 1415 keV γ ray line fed by the β-decay from both states. Taken

together we extract the production rates of the short and long-lived states to be 73(6)% and 27(5)% and their $P_{\beta p}$=5.0(6)% and 12.5(20)% respectively. These $P_{\beta p}$ values are somewhat smaller than the ones reported in [3], although they agree within 2σ.

The same fit provides the relative contribution of the two decaying ^{96}Ag states to the β-delayed proton activity. The relative contributions of the states to the β activity can be obtained by comparing the intensities of the β-delayed 325 keV γ rays mainly fed by the β-decay of the shorter lived state, to the intensity of the 1415 keV γ ray line fed by the β-decay from both states. Taken together we extract the production rates of the short and long-lived states to be 78(10) and 22(10)% and their $P_{\beta p}$=6.50(80)% and 14(3)% respectively.

Figure 5.17 shows a portion of the γ spectrum recorded in coincidence with the βp-activity.

The γ lines at 1351 and 680 keV were observed here with higher resolution than in [3], half-life measurement of this lines were possible (see table) and βp-spectra in coincidence with these lines also measured (see fig.). In addition, we observe two additional γ lines at 717, and 913 keV that were previously reported from in-beam spectroscopy of ^{95}Rh, and attributed to the depopulation of the $(17/2^+)$ level at 2069 keV and the $(17/2^+)$ level at 2264 keV [86]. The 2069 keV state might be the one reported by [3] at 2080 keV. We also observe clearly two γ lines at 1076, and 1425 keV. Their energies are compatible with the few counts reported by [3] at similar energies, which by comparison with the N=50 isotone ^{93}Tc were tentatively assign the spin $5/2^+$and 11/2+. In addition, we observe a number of weaker γ transitions that we can clearly assign to ^{95}Rh, but which do not correspond to any known level in ^{95}Rh. The low statistics prevents us from placing these transitions in the ^{95}Rh level scheme. They are listed in Tab.5.2 together the known transitions

observed in this work.

As was already emphasized in [3], the γ line at 1351 keV, which stems from the depopulation of the $13/2^+$ state in 95Rh is fed mainly by the decay of 8^+ state, while the line at 680keV stems from a state that is presumably $7/2^+$ and is populated mainly by the decay of the 2^+ state only. This is because protons tend to carry little angular momentum, and is corroborated by the half-life measurement. The new half-life we measure agrees with this picture, and hence with the spin assignments of excited states in 95Rh.

Table 5.2: ^{96}Ag βp-delayed γ rays assigned to transitions in ^{95}Ru with half-lives and intensities. The latter is determined assuming that each peak stems only from either the 2^+ or the 8^+ state, depending on the half-life. In same cases the statistics does not allow a half-life determination. When known, the energy and spin of the level that originates the γ peaks is reported.

Peak energy	half-life	Initial State		Final State		$I_{\beta p}$ (%)
(keV)	s	(keV)	J^π	(keV)	J^π	
607.5(10)	5.1(11)					
637(2)						
716.5(5)	4.6(10)	2069	$(15/2+,17/2^+)$	1350.9	$13/2^+$	0.11(3)
912.7(5)	4.8(10)	2264	$(17/2^+)$	1350.9	$13/2^+$	0.090(27)
680.6(1)	6.4(4)	680.5	$(7/2^+)$	0		4.9(18)
1176.5(5)	5.1(8)	1176.5	$(5/2^+)$	0		0.25(8)
1288.0(5)	6.9(4)					0.5(2)
1333.0(5)	6.2(18)					0.27(3)
1351.0(1)	4.25(4)	1351	$13/2^+$	0	$(9/2^+)$	0.60(15)
1424.5(3)	3.9(8)	1424.5	$(11/2^+)$	0	$(9/2^+)$	0.6(2)
1461						

5.1.6 βp-decay of ^{95}Ag

The first identification and half-life measurement of ^{95}Ag was reported in [72], where a half-life of 2.0(1) s was inferred from βp-decay data. Later, a half-life

of 1.74(13) s was deduced from $\beta\gamma$ coincidence data [2]. The discrepancy was explained with a possible ^{95}Pd contamination in the earlier βp study, and was not interpreted as evidence of a contribution from a β decaying isomer [2].

The nucleus of ^{95}Ag as well as other odd-A nuclei in the ^{100}Sn region, is particularly interesting because of the occurrence of spin gap isomers. In the case of ^{95}Ag, a $1/2^-$ and a $23/2^+$ isomeric state, were predicted by shell model calculations [1,2]. However, in the case of ^{95}Ag both isomers were identified in γ-decay studies [9,10]. The rather short lifetime limits of < 500 ms and < 16 ms, respectively, and the inferred decay modes, are at odds with the shell model calculations of [1], who predict sizable β branching. On the other hand, the data agree very well with the shell model calculations of [2], who employ a larger model space, and who predict short lived states with negligible β branches. β-decay from ^{95}Ag is therefore likely dominated by the decay from the ground state.

In the present work, βp-emission from ^{95}Ag was studied for the first time after [72]. The proton energy spectrum in Figure 5.21 agrees with [72], and our βp-decay half-life of 1.80(8)s, with no evidence of a second time component, agrees with the $\beta\gamma$ half-life obtained by [2] resolving the discrepancy with the earlier βp decay data [72] and supporting the conclusions of [2].

We determine for the first time $P_{\beta p}$=2.5(3)%. We are not expecting a significant contribution to this proton activity from the βp-emission of the $21/2^+$ isomeric state in ^{95}Pd for three reasons: a)it would be difficult to populate it via the β-decay of the (9/2+) ^{95}Ag ground state b) its half-life is long (13s), and c) its $P_{\beta p}$ small (0.74±0.19%).

In addition, we identify for the first time two γ lines, following the βp decay of ^{95}Ag with energies of 247.5(20) keV and 316.4(3) (see Figure 5.19). Their half-lives are 1.37(40) s, and 1.70(25) s respectively, which is compatible with the half-life of

^{95}Ag. We therefore assign these γ-lines to previously unknown transitions in the ^{94}Rh daughter.

5.1.7 βp-decay of ^{93}Pd

The N = Z + 1 nucleus ^{93}Pd, is a waiting point in the astrophysical rp-process. ^{93}Pd was first identified experimentally in a fragmentation experiments at the NSCL [87]. The first half-life measurement of $9.3^{+2.5}_{-1.7}$ s was reported based on a preliminary data analysis [88]. It was pointed out however that this preliminary analysis suffered from some problems [89]. Later, a final value of 1.0(2) s was published [82]. Further experiments confirmed this new value with reported half-lives of 0.9(2) s [36] and 1.3(2) s [37]. We obtain a half-life of 1.115(45) s from our βp decay spectrum confirming the previous measurements and improving the accuracy. β-delayed proton activity from ^{93}Pd was first reported in [36], who obtain an upper limit for $P_{\beta p}$ of 5%. [37] observed two γ rays with energies of 865.7(5), and 991.5(10) keV following the β-delayed proton emission of ^{93}Pd. They find that the intensities of the observed lines when compared with statistical model predictions [22,90], are more consistent with a $9/2^+$ ground state of ^{93}Pd, though they cannot exclude $7/2^+$. The same models also predict that for a $9/2^+$ ground state of ^{93}Pd, βp decay would weakly populate the 6^+ state in ^{92}Ru, followed by emission of a 817 keV γ-ray. This line was too weak to be observed in [37]. Besides of the confirmation of the previously reported βp delayed γ-rays at 865 and 991 keV we indeed do see some evidence of a 817 keV line (Figure 5.23(a)), but the time distribution of these events (see Figure 5.25) does not seem to be compatible with an exponential decay with a half-life of 1.115 s. A Poisson likelihood maximization fit of this data to an exponential function with a fixed half-life of 1.115 s, and a free background rate, results in a calculated χ^2 of about 25. The fit has 2 free

parameters (background rate and initial activity) and hence, the probability for such a χ^2 given the hypothesis of 1.115 sec half-life is very low (basically zero). A fixed background rate for the decay curve gated on gammas in the energy range 750-850 keV (0.02 counts/sec) would not change this result. Monte-Carlo calculations support the same conclusions. They show that the probability to record a time distribution like the one in Figure 5.25 with four detected counts and three of them occurring at time larger than 3 sec is about 0.6%. On the other hand, the probability that the observed counts originate from a random background is also unlikely. Given the background rate, the probability that four counts randomly form a peak is about 4% only. We attribute the observed peak to a contamination, possibly from ^{92}Rh whose β decay also populates the 6^+ state in ^{92}Ru (see [91,92], and Section 5.1.8 of this thesis).

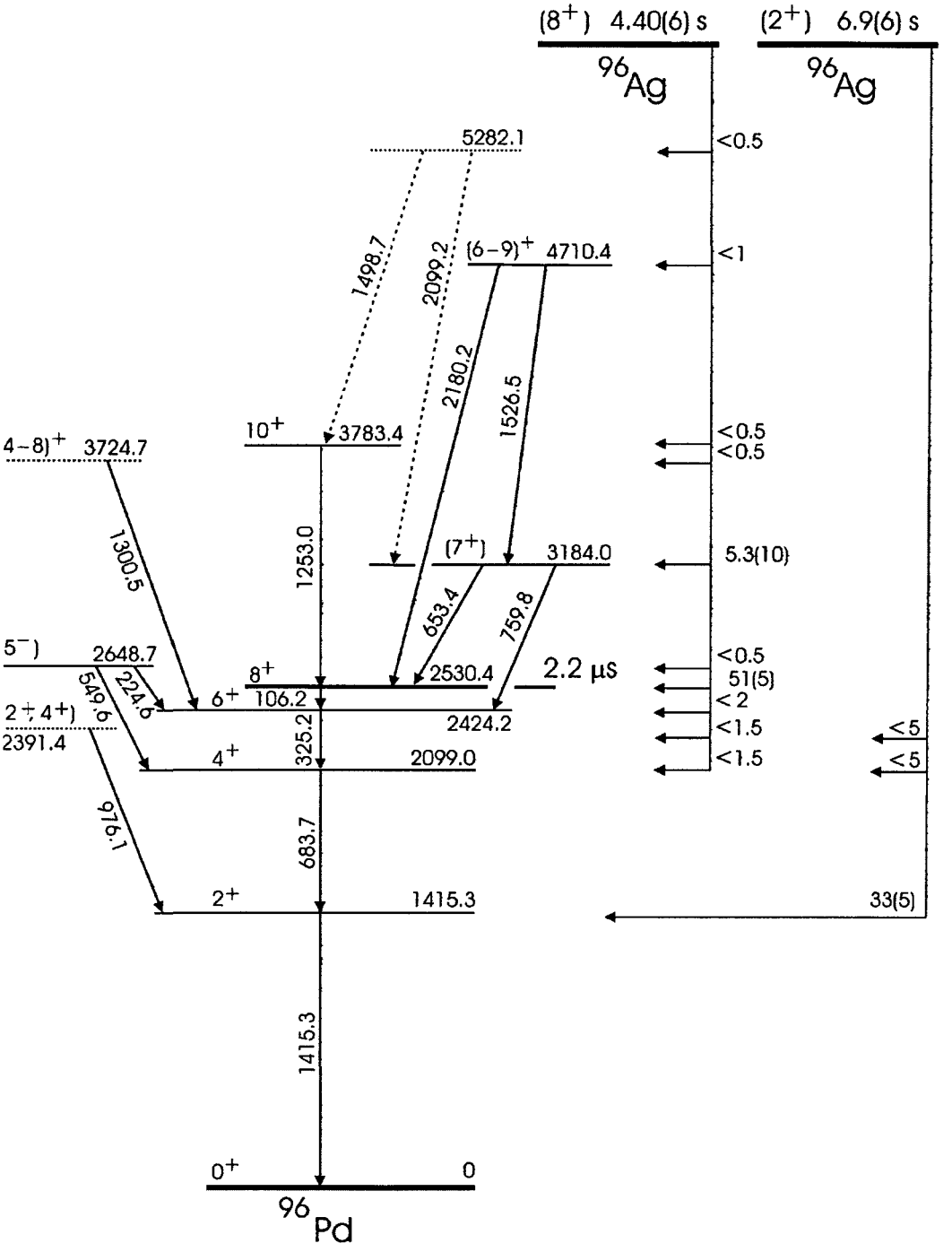

Figure 5.14: Decay scheme of the two ^{96}Ag states that β-decay into states of ^{96}Pd, as deduced in [3].

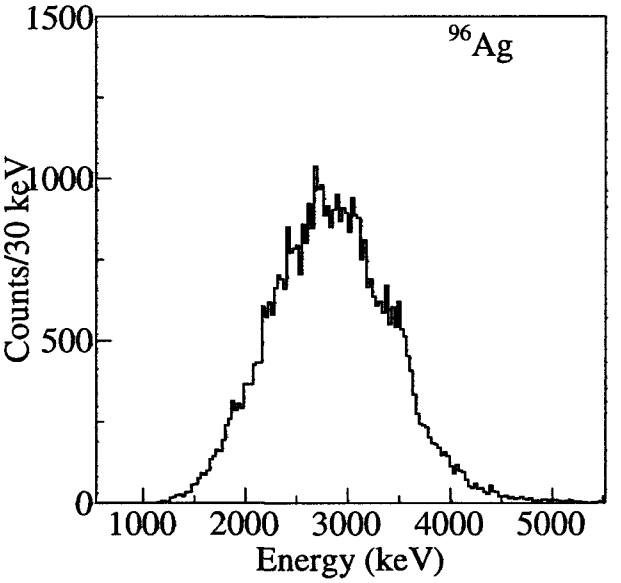

Figure 5.15: Energy spectrum measured for the βp-decay of ^{96}Ag.

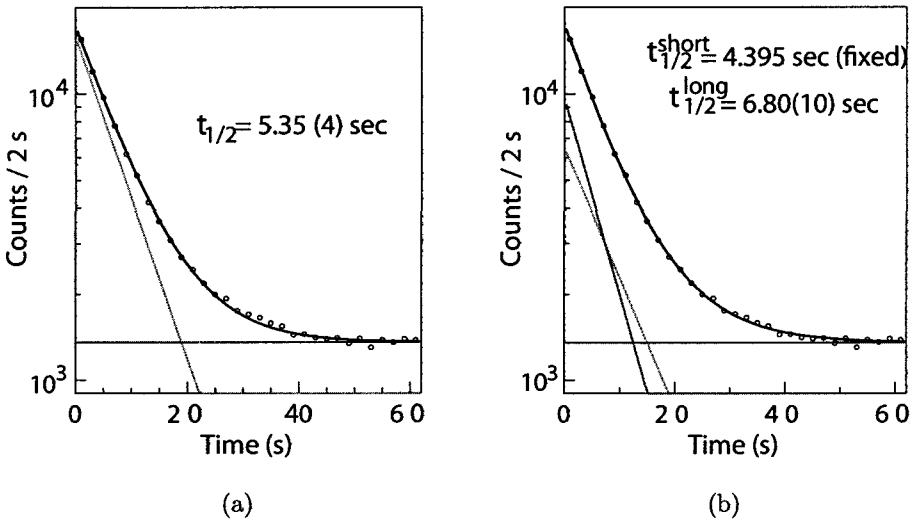

Figure 5.16: Time distribution of β-delayed proton activity from 96Ag fit with (a) one exponential component plus background, and (b) two exponential components, one of them fixed to a half-life of 4.395 s

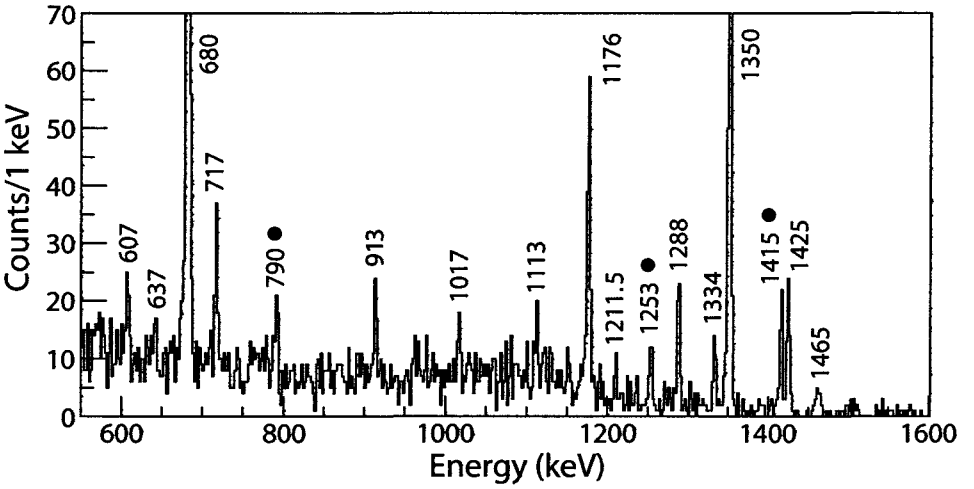

Figure 5.17: Section of the measured γ spectrum in coincidence with βp-decays of ^{96}Ag. The strongest transitions are labeled with the corresponding energy. The lines marked with full circles are background lines from ^{97}Cd. The others are attributed to the depopulation of states in ^{95}Rh.

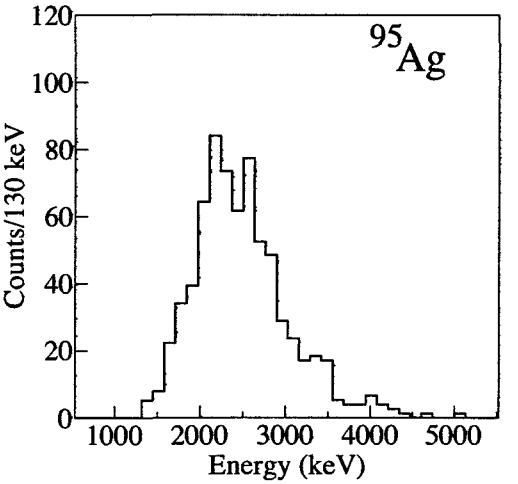

Figure 5.18: Energy spectrum of the energy deposited by the βp-events of ^{95}Ag.

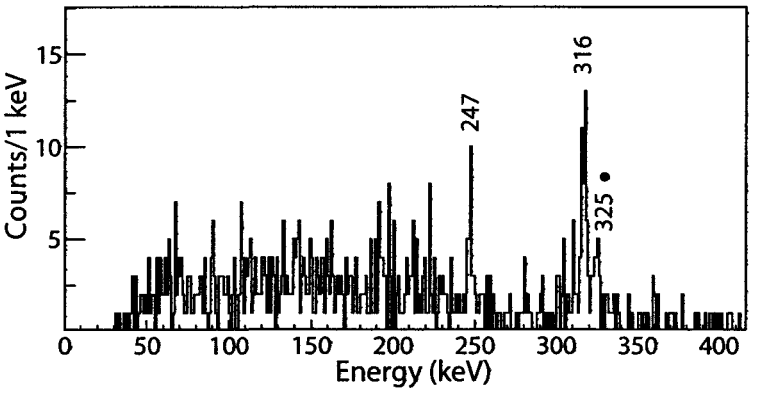

Figure 5.19: Section of the γ spectrum recorded in coincidence with β-delayed protons from the decay of ^{95}Ag. Two γ lines at 247.5 and 316.4 keV are assigned to the βp-decay of ^{95}Ag. The line at 325 keV is a contamination from the βp-decay of ^{97}Cd.

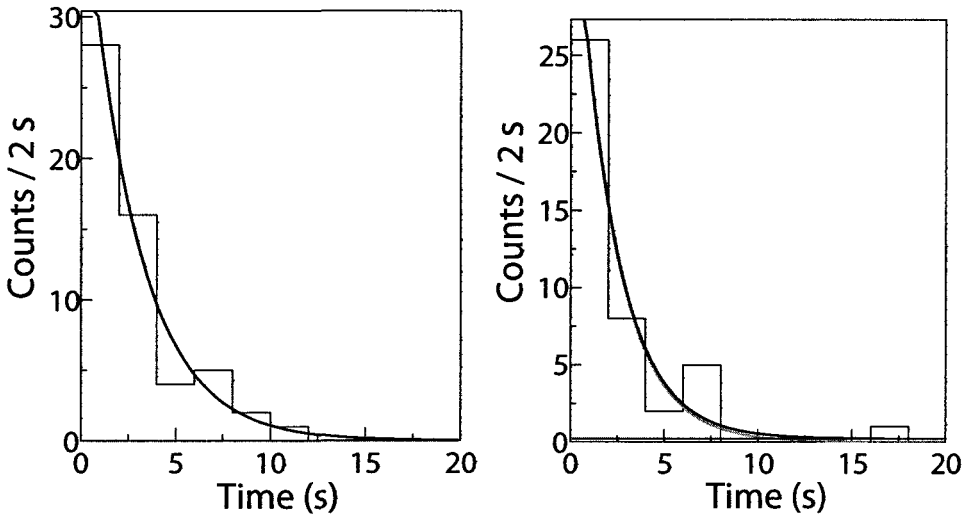

Figure 5.20: Decay curve of the 95Ag βp-decay event gated on the gamma-ray a)316 keV and b)247 keV.

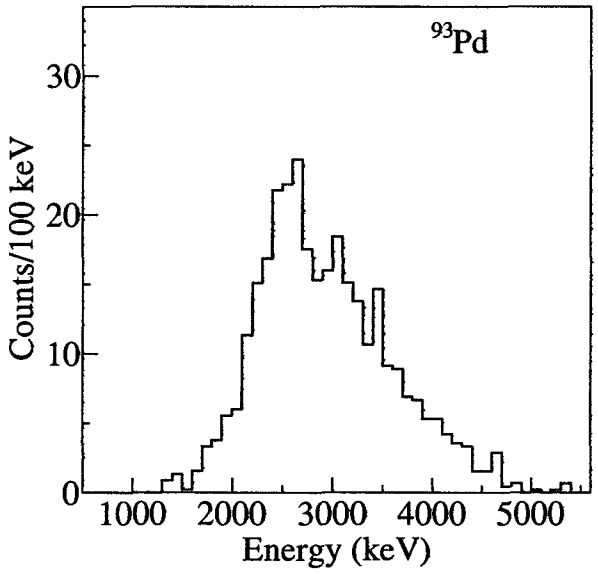

(a)

Figure 5.21: Energy deposited in the DSSD by the β-delayed proton emission events for ^{93}Pd.

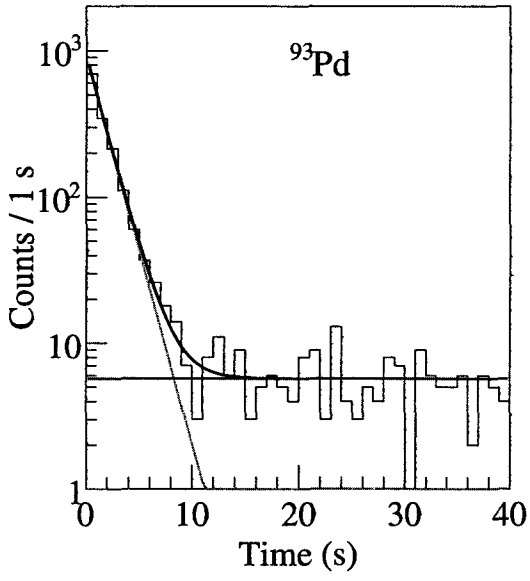

(a)

Figure 5.22: Time distribution of the βp-events from ^{93}Pd.

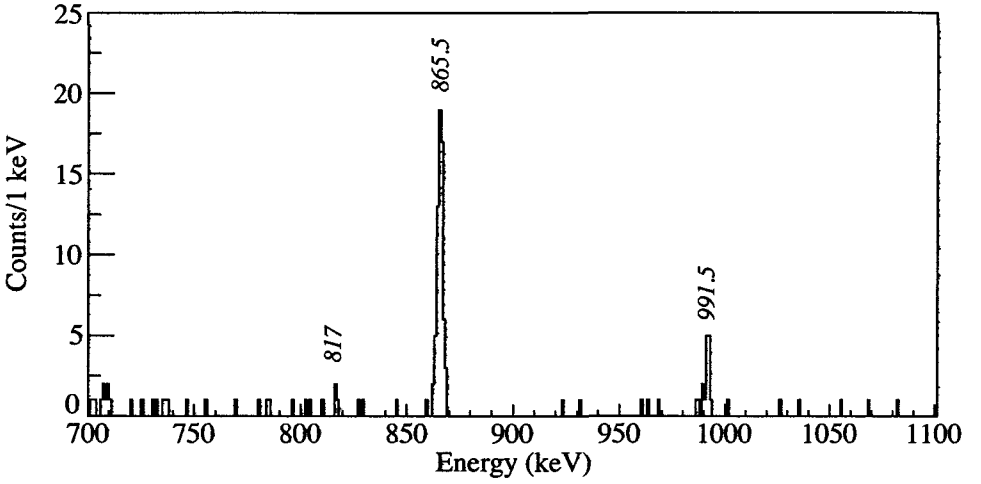

(a)

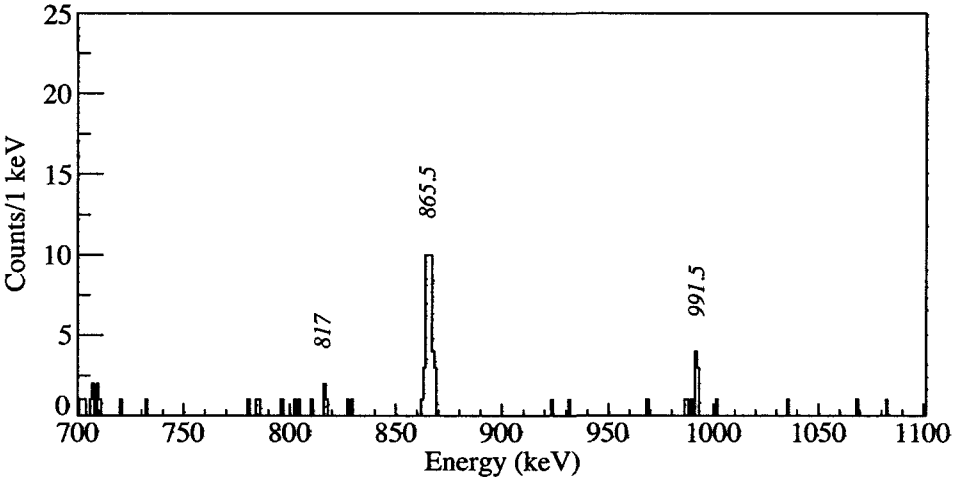

(b)

Figure 5.23: Section of the measured γ spectrum in coincidence with β-delayed protons from the decay of ^{93}Pd. The upper panel shows the spectrum recorded with full statistics. In the lower panel, a subset of the implant –60% of them, chosen drawing a smaller gate in the PID plot–is shown. In both cases, the labeled peaks correspond to the know de-excitations in the βp daughter ^{92}Ru $2^+ \rightarrow 0^+$ (865 keV) and $4^+ \rightarrow 2^+$ (991 keV). Four counts at 817 keV suggest the weak population of the $6^+ \rightarrow 4^+$ transition.

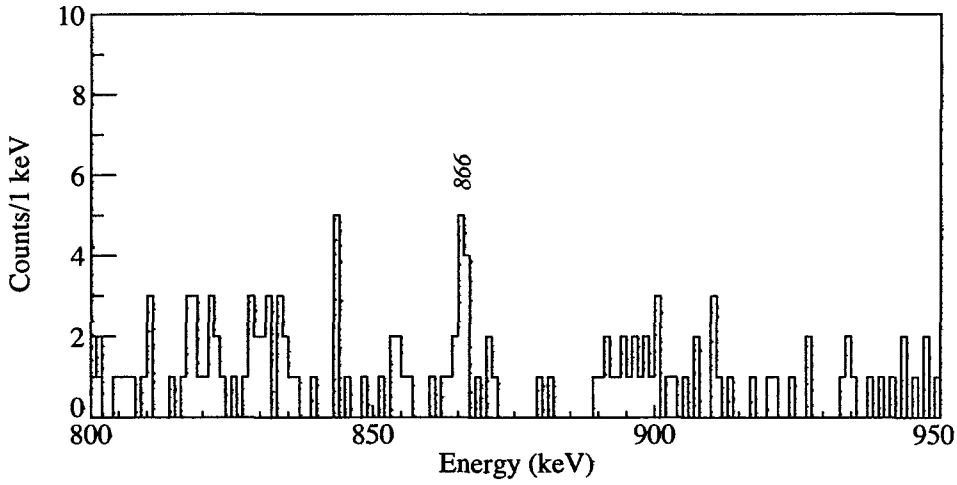

Figure 5.24: Section of the γ spectra recorded in coincidence with β-decays not followed by proton emission. In this case, a short correlation time of 1 s was chosen to maximize the signal to background ratio. The labeled peak corresponds to the de-excitation of a known $13/2^+$ state in ^{93}Rh

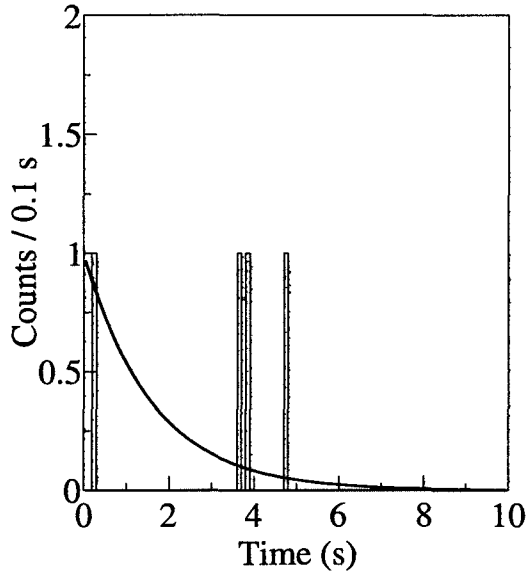

Figure 5.25: Time distribution of β-delayed proton decay events in coincidence with the γ rays at 817 keV. The represented decay curve fit with an exponential decay of fixed half-life 1.115 s

The further attempt to reduction the background by gating the γ spectra on protons that are only in the energy window available for β-delayed proton emission of ^{93}Pd into the 6^+ state in ^{92}Ru at 2671.5 keV was not successful. This window is infect 4922(160) keV and hence it approximately coincide with the upper limit of the entire proton distribution hence do not constitute a further constraint. This estimate is based on the recent penning trap mass measurements of ^{93}Rh, and ^{92}Ru [93], that results in a S_p=2007(9) keV, on the most recent deduced mass for ^{93}Pd [94] that result in a Q_{EC}=9600(160) keV, and the known energy of the 6^+ state 2671.5 keV. This upper limit approximately coincide with the upper limit of the entire distribution, and hence, it can not be used to reduce background.

The intensities of the three observed γ lines were used to estimates the relative βp t branching ratios to different states in ^{92}Ru: 100% (2^+), 19(7)% (4^+), and $<$ 6% (6^+). Those values agree with the ones reported in [37] in principle confirming the assignment $9/2^+$ for the ground state of ^{93}Pd based on comparison with statistical model calculations. On the other hand, we report here for the first time a total β-delayed proton branch for ^{93}Pd of 7.4(4)%, slightly higher than the upper limit of 5%, established in [36]. Taking the statistical model calculations presented in [37] at face value, this would be more consistent with a $7/2^+$ ground state in ^{93}Pd ($P_{\beta p}$ = 4.8%) than a $9/2^+$ ground state ($P_{\beta p}$ = 1.7%), possibly indicating a problem in the theoretical model. The energy spectrum of β-delayed protons is shown in Figure 5.21, and agrees with [36], confirming the absence of significant isobaric contamination in the latter.

There is a question about the assignment of the β-delayed γ-ray of 864.1 keV reported by [36], who assign it to the decay of a known $13/2^+$ state in ^{93}Ru. On the other hand, [37] favor an assignment to the deexcitation of the first 2^+ state in ^{92}Ru of similar energy (864.6 keV). We can now clearly distinguish γ-rays from

β and βp decay. As Figure 5.23(b) shows, both γ-rays are produced following the β-decay of ^{93}Pd so [36] likely observed a mixture. The intensity ratio that we observe for the two lines is $I_{\beta 864}/I_{\beta p 864}$=2.3(5).

5.1.8 βp-decay of ^{92}Rh

The nucleus of ^{92}Rh has been previously studied by both in-beam [95–98] and βdecay spectroscopy [91, 92]. In the most recent β-decay study of the mentioned ones [92], the placement of the γ line at 919.1 keV did not agree with previous in-beam experiments, and a new line at 340 keV was identified and placed in the level scheme. Our data agrees with the level scheme proposed by [92]. We confirm that the line at 919 keV is in coincidence with 991 and 865 keV, but not with 817, and 163 keV. We infer for ^{92}Rh from both βp and $\beta\gamma$ data an half-life of 5.3(2) sec.

We also detect proton activity stemming from the decay of ^{92}Rh (see Figure 5.26). The βp-ratio that we measured measured for the first time is 1.9(1). Besides, in Figure 5.27 shows the gamma spectrum recorded in coincidence with βp-events from ^{92}Rh. The γ lines at 395, 893, 1096 keV from the known 91Tc levels at 394.4, 892.4 and 1097 keV are detected.

[92] report the existence of a 2^+ isomeric state with half-life 0.53(37) s, detected as a second time component in the decay curve of ^{92}Rh recorded in coincidence with the γ radiation 864 keV gamma radiation.

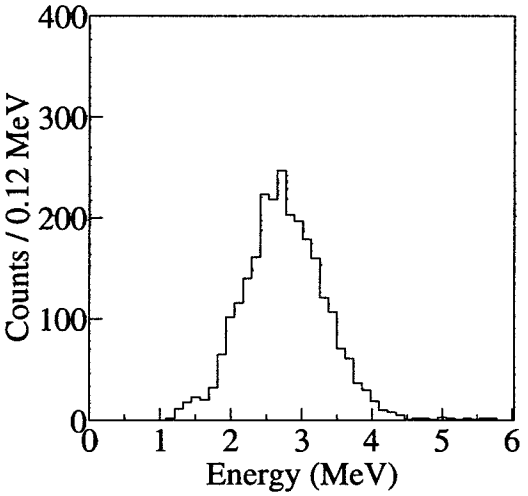

Figure 5.26: Energy deposited in the DSSD by the β-delayed proton emission events for ^{93}Pd.

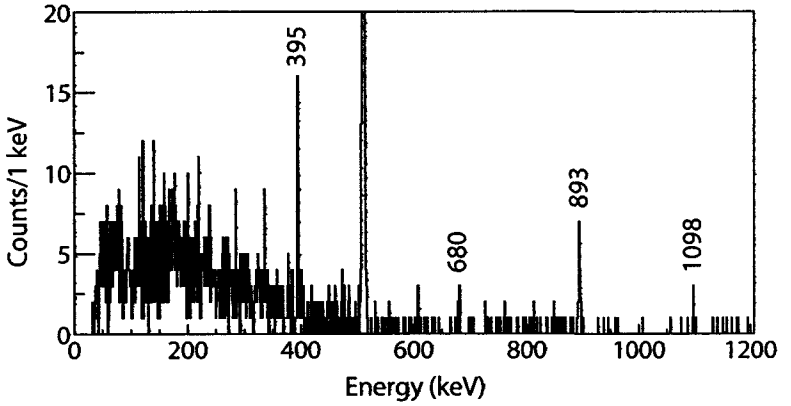

(a)

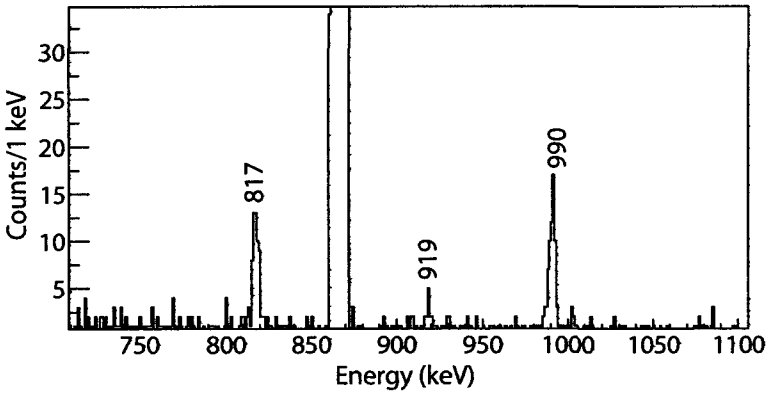

(b)

Figure 5.27: (a) Section of the γ spectrum from the decay of ^{92}Rh, in coincidence with protons, and (b) in coincidence with the 864 keV gamma-ray

Table 5.3: Compilation of half-lives and $P_{\beta p}$ measured in this work and reported in the literature.

		Half-life (s)		$P_{\beta p}$ (%)	
Isotope	J^π	This work	Literature	This work	Literature
^{93}Pd		1.115(45)	1.0(2) [82]	7.4(4)	<5 [36]
			0.9(2) [36]		
			1.3(2) [37]		
^{92}Rh$^{(g)}$	6^+	5.3(8)	4.6(25) [92]	2.0(3)	
^{92}Rh$^{(m)}$	(2^+)		0.5(2) [92]		
^{95}Ag		1.85(8)	2.0(1) [72]	2.5(3)	
			1.3(2) [3]		
^{96}Ag	(2^+)	4.395(85)	4.40(6) [1]	6.5(8)	8.5(15) [1]
	(8^+)	6.8(10)	6.9(6) [1]	14(3)	18(5) [1]
^{96}Cd			$1.03^{+0.24}_{-0.21}$ [66]	5.5(40)	
^{97}Cd	$(9/2^+)$	1.0(1)	2.8(6) [3]	11.8(20)	
	$(25/2^+)$	3.8(2)		25(4)	
^{98}In$^{(g)}$		0.047(13)[a]	0.032^{+32}_{-11} [82]	5.5^{+3}_{-2}	
^{98}In$^{(m)}$		1.27(30)	$1.2^{+1.2}_{-0.4}$ [82]	19.5(13)	
^{99}In		3.1(2)[a]	3.0^{+8}_{-7} [82]	0.9(4)	
		3.05(60)			
^{100}In		5.7(3)[b]	5.9(2) [38]	1.7(4)	1.6(3) [38]
		6.0(5)	6.1(9) [99]		0.8(3) [99]
			6.7(7) [100]		

[a] Half-life inferred from β-decay data.

[b] Half-life inferred from weighted average of $\beta\gamma$ and βp-decay data.

Chapter 6

Astrophysical implication

In this chapter we discuss the implications of our new measurements for the rp-process. The chapter is structured in four parts. In Section 6.1, we summarize the model used to simulate X-ray bursts. In Section 6.2, we discuss the impact of the new $P_{\beta p}$ measurements. In Section 6.3, we discuss the implication of the newly measured half-life of ^{97}Cd. In Section ??, we suggest that the measurements of $P_{\beta p}$ in the ^{100}Sn region helps to extend systematic trends of βp-emission strength known for lighter nuclei to heavy region of interest for the rp-process.

6.1 Single-zone X-ray burst model

To explore the implications of our new measurements for X-ray burst models, we used a single-zone X-ray burst model [101] based on ReaclibV1 rates provided by JINA Reaclib online database [102]. In this model, variation of burning conditions and initial composition with depth is neglected, and only a single burst is calculated, requiring to fold inter burst (compositional inertia) into the choice of initial conditions. We chose conditions that reflected the burning of a low metal-

licity solar composition with little pre-burst hydrogen burning [63]. Burst ignition conditions were chosen to reflect an accretion rate of 10% of the Eddington rate, a thermal flux out of the neutron crust of 0.15 MeV per accreted nucleon, and a metallicity Z= 10^{-3} of the accreted material. An accreted layer with solar metallicity would produce a similar burst at a higher accretion rate. Therefore, our calculation models the first burst occurring after a longer period of quiescence. This model predicts a rather extended rp-process into the Sn region and is thus suitable to explore the general features of an rp-process flow in the Cd-Sn region. The reactions flow in the Cd-Sn region is shown in Figure 6.1.

In principle, 1D multi-zone codes are available today to carry out more sophisticated modeling of an entire burst sequence. In such models, the neutron star surface is modeled by layers of material with independently tracked. Although Multi-zone codes allow one to consider effects like the ignition of ashes of previous bursts on later ones and the heat generated by this process, they are computationally intensive and unnecessary for qualitative studies such as ours, where we only aimed to study relative sensitivity of one input parameter. Single-zone models are computationally less demanding, and on the other hand, have been shown to give similar results to multi-zone models, when the initial conditions are properly calibrated.

6.2 Effects of βp-emission in the ^{100}Sn region

In order to understand the impact of our new $P_{\beta p}$ measurements on the rp-process, we need to study how the β-delayed proton emission of nuclei in the ^{100}Sn region affects the rp-process path. The results of the single zone X-rays model were found to be the same for all nuclei under investigation, which are illustrated in Figure 6.1.

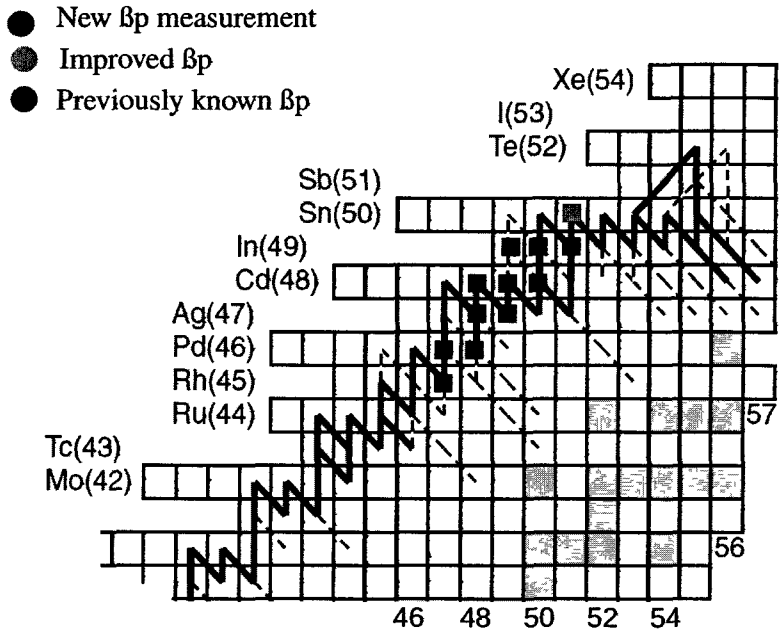

Figure 6.1: β-delayed proton precursors studied in this work along with the rp-process path. Different colors (online) identify new $P_{\beta p}$, improved $P_{\beta p}$, or previously known $P_{\beta p}$.

Thus, we illustrate our findings using ^{97}Cd as a reference case. Figure 6.2 (left panel) shows a representation of the reaction flow during the X-ray burst phase when a series of proton captures and beta decays (reaction flow) drives matter toward heavier nuclei. When this flow reaches ^{97}Cd, a fraction of the flow proceeds into ^{98}Cd via β-decay and one-proton capture. The remaining fraction – corresponding to $P_{\beta p}$–also proceeds into ^{98}Cd, but via βp-emission into ^{96}Pd first and then via two proton captures. Therefore, the effect of the βp-emission during the X-ray burst is to produce ^{96}Pd that would not be produced otherwise. The right panel of Figure 6.2 shows a representation of the flow of matter during the freeze-out phase, when the proton captures are no longer possible owing to a temperature drop or to a running out of hydrogen fuel. In this case, if βp-decay were not considered, the amount of ^{97}Cd produced in the previous phase would

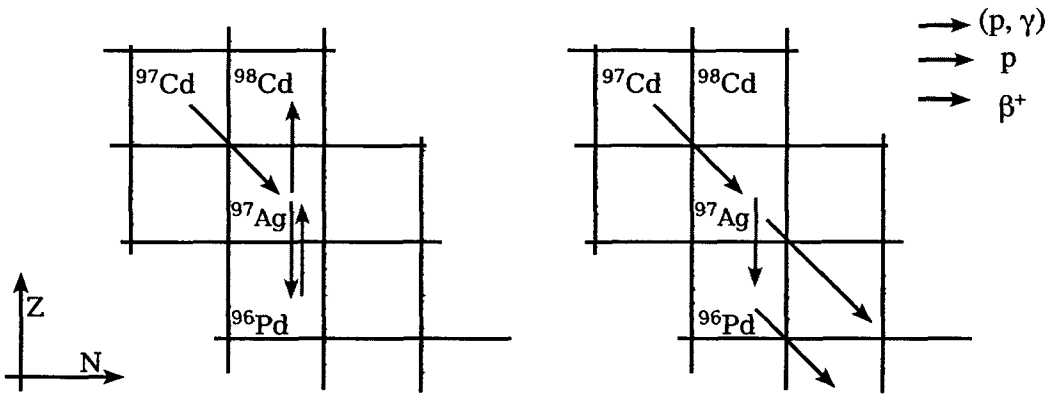

Figure 6.2: Reaction flow after reaching ^{97}Cd in the X-ray burst phase (left panel) and freeze-out phase (right panel).

decay back to stability via beta decay, and because beta decay proceeds thought isobaric chains, all the ^{97}Cd abundance would finally be found in ^{97}Mo. If instead, βp-decay were considered, the same fraction of the flow as before ($P_{\beta p}$) would proceed through ^{96}Pd, but this time it would not be destroyed by the proton capture process.

Figure 6.3(a) illustrates the analysis described above with more quantitative details. The time dependent abundances of the nuclei in the rp-process path produced immediately after β-decay of ^{97}Cd (i.e. ^{97}Ag, ^{96}Pd and ^{98}Cd) are analyzed, including βp-emission (solid lines) and without including βp-emission (dashed lines). When the ^{97}Cd βp-emission is considered ($P_{\beta p}$=12%), the production of ^{96}Pd starts at earlier time compared to when βp-emission is not considered. However, the amount of ^{97}Ag and ^{98}Cd are not significantly affected at this early stage. This indicates that the (p, γ) capture reaction immediately converts any ^{96}Pd produced by β-delayed proton emission into ^{97}Ag, the same nucleus that would have been produced by simple β-decay. The rp-process path is hence not strongly affected by the β-delayed proton emission. During the freeze-out phase, instead, the amount of ^{97}Cd left after the X-ray burst β- and βp-decays back to stability. Like in the

X-ray burst phase, the βp-decay of ^{97}Cd also produces ^{96}Pd, but at this stage it will not undergo proton capture, and β-decays instead, ultimately producing ^{96}Mo rather than ^{97}Mo.

In addition to the previous analysis, we considered interesting to investigate the dependence of the effect of the βp-emission on waiting point half-life. We therefore varied the half-life of ^{97}Cd artificially. The result is depicted in Figure 6.3(b) for

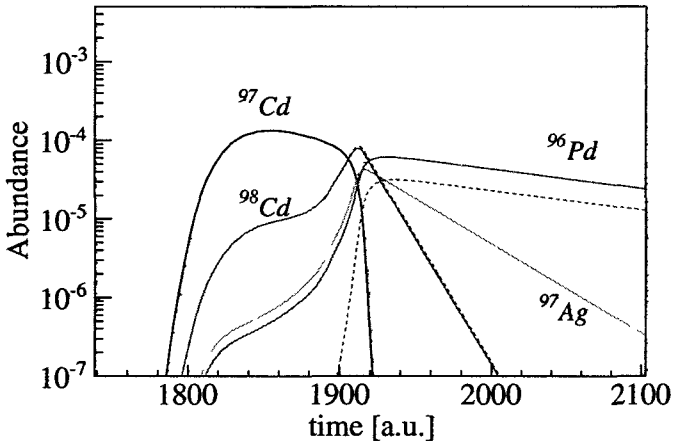

(a)

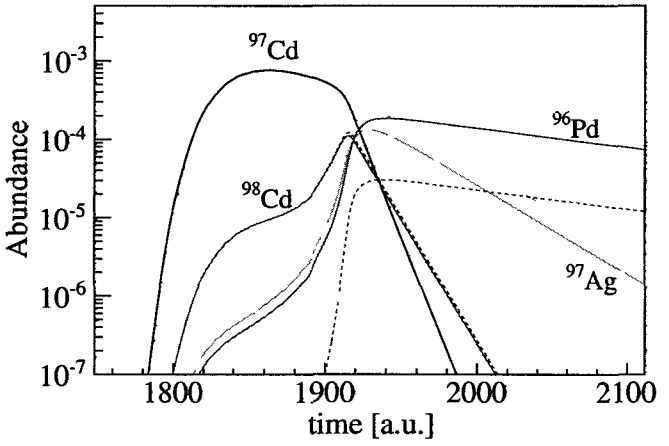

(b)

Figure 6.3: Calculated abundance as a function of time for the nuclei ^{97}Cd, ^{97}Ag, ^{96}Pd and ^{98}Cd including βp-emission (solid lines) and without including βp-emission (dashed lines).

the half-life of $T_{1/2}$=5 s. The mechanism is exactly the same than in the shorter half-life case (Figure 6.3(a)), but the abundance of ^{97}Cd after the burst is higher because ^{97}Cd is a waiting point.

Figure 6.4 shows the isobaric abundance for each mass A calculated with and without all the new $P_{\beta p}$. $P_{\beta p}$ has a significant effect only for masses A=92,96 and 100, corresponding to the βp-decay of ^{93}Pd, ^{97}Cd and ^{101}Sn.

We aimed to study how the protons emitted during βp-emission are further processed, concluding that they are possibly captured by light nuclei that have a lower Coulomb barrier. This is illustrated in Figure 6.5, which shows a plot of the time dependent abundance for hydrogen and the light nuclei such as ^{24}Al and ^{24}Mg. For this plot, only the $P_{\beta p}$ of ^{97}Cd was considered, and it was artificially increased to 100% to emphasize the effect. There were some abundance variations that happen when the freeze-out starts (when the Hydrogen abundance drops), hence possibly related to the βp-emission of ^{97}Cd. This suggests that β-delayed protons are captured mostly on light nuclei. Thus, we conclude that βp-emission do

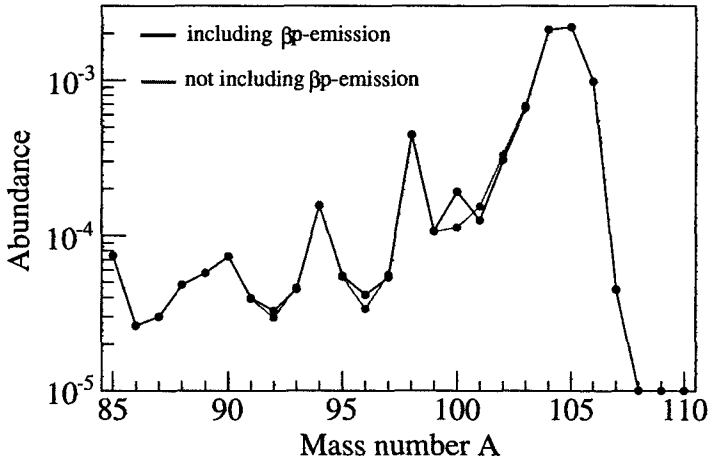

Figure 6.4: Final abundance distribution (mass fraction divided by mass number, summed over isobaric chains) in a single zone x-ray burst calculation with (red) and without (black) β-delayed proton emission.

have an effect on the final composition of the X-ray burst ashes during the freeze-out phase when proton capture rates are slow due to lower temperature or hydrogen exhaustion (otherwise an emitted proton would tend to be recaptured). The largest effect from β-delayed proton emission occurs for the $A = 100$ mass chain, which is significantly fed by the substantial β-delayed proton branch of ^{101}Sn, for which we have improved the accuracy by an order of magnitude. Our results also show that β-delayed proton emission has an effect on rp-process calculations, although the effect is not significantly strong, due to the rather small $P_{\beta p}$ determined in this work. The effect of the emitted protons on hydrogen abundance and burst energetics is not important in this model.

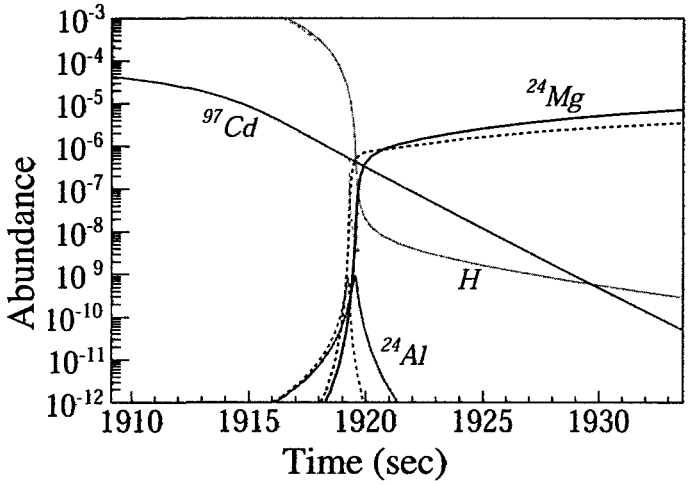

Figure 6.5: Calculated abundances for the nuclei H, ^{24}Si and ^{24}Mg as a function of time including βp-emission of ^{97}Cd (solid line), and without including βp-emission of ^{97}Cd.

As it was pointed out by [18], the nucleus ^{93}Pd is the progenitor of ^{93}Nb in the rp-process. However, the βp-emission populates ultimately ^{92}Mo, improving the ability of the rp-process to produce the p-nucleus ^{92}Mo. This possibility is even more intriguing if one thinks that in the pulsed rp-process ((rp)^2-process), in

which one burst ignites the ashes of a previous burst, overproduce ^{93}Nb [103]. A similar situation applies to ^{97}Cd, which is progenitor of ^{97}Mo via β-decay, and of ^{96}Ru by βp-decay. The nuclei ^{93}Pd and ^{97}Cd are the only ones in the ^{100}Sn region that could possibly affect the production of p-nuclei, because are the only waiting points with a βp-branch. The other waiting points such us ^{96}Cd, ^{92}Pd, ^{94}Pd are even-even so expected to have small $P_{\beta p}$.

After our measurement of the $P_{\beta p}$=6% for ^{93}Pd, and $P_{\beta p}$=12% for ^{97}Cd, we can now quantify the effect of the βp-emission of these two nuclide on the production of p-nuclei and conclude that although βp-emission plays a role in the production of ^{92}Mo and ^{96}Ru, this effect is not substantial.

6.3 Impact of the ^{97}Cd ground state half-life

Although the proton capture Q-value for ^{97}Cd is positive, proton capture is suppressed by strong (γ,p) photodisintegration of ^{98}In, which is only bound by 582 keV, as determined from systematics [84]. This results in 95% branching into β-decay at ^{97}Cd, making ^{97}Cd an rp-process waiting point [85].

Proton capture on ^{96}Ag (ground state spin 2^+ or 8^+) is unlikely to populate or feed the high spin $25/2^+$ isomer in ^{97}Cd. Therefore, the ground state β-decay half-life mainly is needed for rp-process calculations. Corrections for the decay from thermally populated low lying excited states are probably small.

Previous to this experiment, the half-life measurements of 3^{+4}_{-2} and 2.8(6) s were obtained without distinguishing ground state from the predicted isomeric state [2, 35]. The theoretical prediction for the ground state and isomeric stater were 0.9 and 0.6 s respectively. On the other hand, the relative production rate of the two state is absolutely not predictable. Assuming a relative production of

50% for the two states, an upper limit for the ground state half-life that combined with 0.6 s is 5 s.

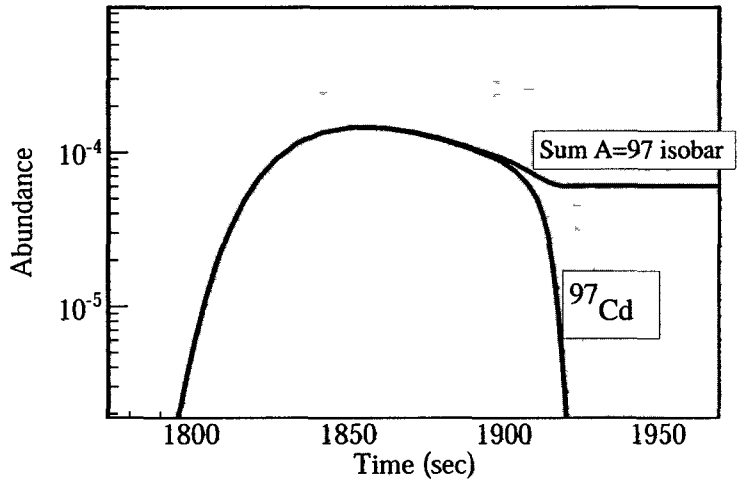

Figure 6.6: Time dependent abundance of ^{97}Cd and of the summed abundance of all A=97 isobars. The solid line represents the abundance calculated with the new ^{97}Cd half-life ($T_{1/2}$=1.1±0.1 s), while the shaded region represents the abundance range based on half-life suggested by theoretical models and previous measurements (0.6-5 s) [1, 2]. The thickness of the line representing the experimental half-life is approximately equal to the abundance uncertainty due to half-life uncertainty.

The implications of the new measurement of ^{97}Cd ground state half-life on the rp-process is shown in Figure 6.6. The total isobaric abundance for each mass is shown for the new half-life of 1.1 s, and for the theoretical upper half-life limit of 5 s. The lower limit of 0.5 s is not represented because it is very similar to the abundance calculated using the half-life 1.1 s. The relatively short half-life of the ^{97}Cd ground state favors the production of masses with A>104, with reduction of masses in the range A=97-104. Masses A=97 is the one most effected, with reductions of 80%. The uncertainty in the $A = 97$ rp-process production –due to half-life–is now reduced by about a factor of 20. Under these circumstances, other

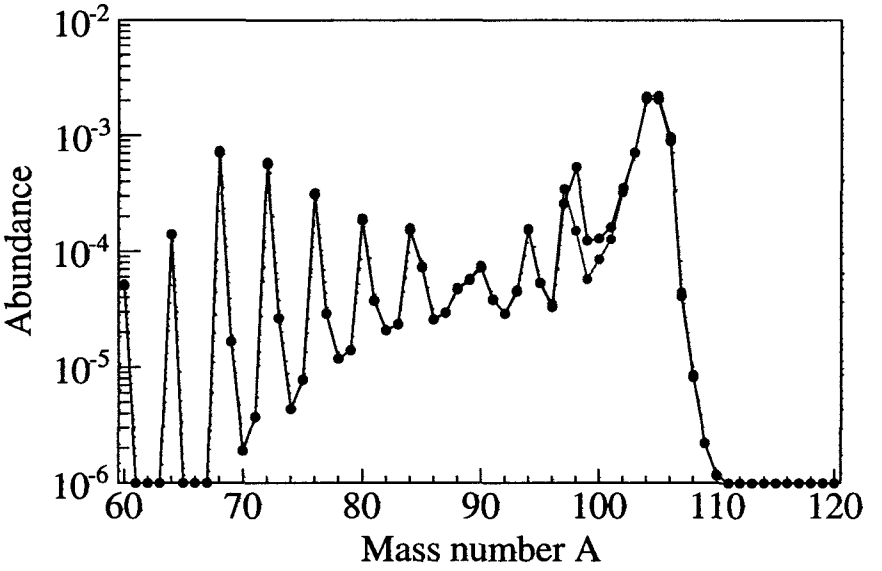

Figure 6.7: Impact of the ^{97}Cd ground state half-life on the final abundance distribution (mass fraction divided by mass number, summed over isobaric chains) in a single zone x-ray burst calculation. Shown is the distribution for the theoretical upper limit of 5 s (black) and the new measured half-life of 1.1 s (red).

sources of uncertainty such as the unknown Q-value for ^{97}Cd(p,γ)^{98}In dominate.

The impact of the new half-life on the light curve has also been explored and

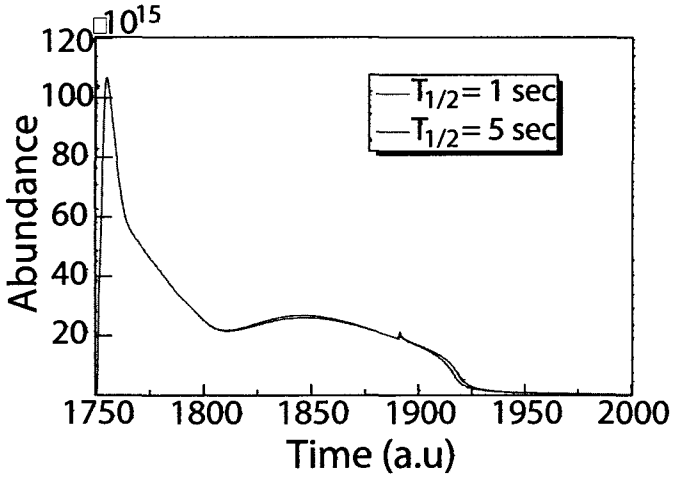

Figure 6.8: Comparison of the X-ray burst luminosity for ^{97}Cd half-life of 1 and 5 s.

is illustrated in Figure 6.8. The short half-life affects most of the duration of the burst. Material is burned faster, and the burst is shorter. The effect is of the order of only a few seconds or few percent.

Chapter 7

Summary and outlook

In summary, this dissertation presents the results of a study of β-delayed proton emission properties of neutron-deficient nuclei in the ^{100}Sn region: ^{92}Rh, ^{93,94}Pd, ^{95,96}Ag, ^{96,97,98}Cd, ^{98,99,100}In, and ^{101}Sn. These results include the β-delayed proton energy spectra for all these isotopes, the measurement of their βp-branching ratio $P_{\beta p}$, and other properties such as proton-γ coincidence spectroscopy. In addition, we measure for the first time the ground state half-life of ^{97}Cd and identify for the same isotope a $25/2^+$ isomeric state. These results were made possible by the development of the Radio Frequency Fragment Separator RFFS, which allowed the beam purification necessary for this experiment.

Prior to this dissertation, the role of the β-delayed proton emission in the rp-process was questioned, and a proper answer could not be given for lack of experimental data such as β-delayed proton branching ratios. An important question was whether the βp-decay of ^{93}Pd and ^{97}Cd produced in the rp-process is a significant source of the light p-nuclei ^{92}Mo and ^{96}Ru found in nature. We find that the β-delayed proton emission in the ^{100}Sn region does affect the final composition of the rp-process ashes, mainly for the masses A=92,93,96,97,100,101. βp-emission

also slightly alter the burning conditions in the late stage of the *rp*-process. We find that $P_{\beta p}$ for ^{93}Pd and ^{97}Cd are too small to make the rp-process a significant source of ^{92}Mo and ^{96}Ru. The relatively short half-life for ^{97}Cd further reduce the production of A=96,97 nuclei. With the ground state half-life measurement of ^{97}Cd all the rp-process waiting point nuclei now have a measured half-life.

In addition, our $P_{\beta p}$ measurements also allow us to extend the systematic trends of βp-emission strength known for lighter nuclei into the ^{100}Sn region. These trends suggests that all the nuclei of interest for the *rp*-process may have $P_{\beta p}$ smaller than about 20%.

The results also have implications for our understanding of the structure of nuclei. We find evidence of the predicted $25/2^+$ isomeric state in ^{97}Cd and we measure its half-life. Because of the sensitivity of isomeric properties to shell model interaction, this isomer provides an important testing ground for shell models in the future. The fact that the our measured half-life (3.8±0.2 sec) disagrees with the calculated one (0.6 sec [2]) already indicate that there are details in the calculation that need to be revised.

Our experimental data also allow us to measure the $P_{\beta p}$ for ^{101}Sn with much higher accuracy than the previous study [39]. The uncertainty of this value had been one of the limitations in constraining the properties of the ^{101}Sn ground state [40], and is now significantly reduced. This is the first step –mass measurement will also be needed to remove remaining uncertainties to enable comparison of the nuclear structure predicted by shell models. All the β-delayed proton energy spectra that are presented in this work provide further constraints for future shell model calculations, constraining for instance the high-energy-part of the GT-strength.

This dissertation was successful to accomplish its goals, but for further studies

in the ^{100}Sn region, the statistic and the setup could be improved. First, the purification of the beam could be improved by using a second RFFS stage, and the quality of the particle identification should be improved developing a momentum tracking detector able to handle high rates. The momentum tracking would also allow for a larger A1900 acceptance. Second, a higher efficiency decay station is desirable, which can be achieved with an improved electronics such as lower noise preamplifiers that allow one to work with lower electronic thresholds. A larger number of detectors could also be used to improve the solid angle coverage of the β-calorimeter. Third, the use of two separate data acquisition systems, one triggered by the BCS and one triggered by SeGA would extend the time window available for prompt and β-delayed γ observation allowing, for instance, to study longer lived isomeric states and improving the γ efficiency. Finally, as one moves toward the proton drip line, direct proton emission can occur. To study these phenomena, the BCS should be modified since implantation would obscure the protons emitted immediately after. A different BCS should be developed with detectors outside the implantation location, which would also be a natural solution for the β-pile-up problem, and for study correlation in case of β-delayed-two proton emission –another phenomena likely to occur at the proton drip line.

Appendix A

Partial, reduced widths, spectroscopic factors

In this appendix we describe the concepts of penetration factors, partial, total, reduced widths, and spectroscopic factors. In the following sections, proton emission from one single state in the simplified case of nuclear potential as a simple square well with a sharp nuclear radius is studied for spin-less neutral particle in s-wave (l=0) to illustrate how a $Breit-Wigner$ resonance raise, and to illustrate the meaning of quantities like particle, reaction, and total widths. This description is extended to charged particles with arbitrary l to illustrate quantities like penetration factors, reduced widths, and resonance shift. Further, particles with spins are considered, and partial width introduced. Finally, the compound nucleus description is introduced, as increase number of states involved, introducing the spectroscopic factors.

A.0.1 The Breit-Wigner formula for s-wave neutrons

Lets assume a nuclear potential seen by the captured particle as a square well. The general solution of this problem, in the interior is:

$$u_{in} = Ae^{iKr} + Be^{-iKr} \tag{A.1}$$

We specialize the previous formula considering that that a phase has to accounted between incoming and outcoming spherical wave, accounting foe the possibility that the particle is absorbed in the nuclear interior due to a reaction. This lead to the following:

$$u_{in} = Be^{2i\alpha}e^{-q} + Be^{-iKr} = 2Be^{i\alpha-q}cos(Kr + \alpha + iq) \tag{A.2a}$$

$$u_{out} = e^{iKr} \tag{A.2b}$$

both and q are real with q>0 becasue no particle con return.

The continuity of the logarithmic derivative of the wave functoin requires:

$$f_0 = R\left(\frac{1}{u_{in}}\frac{du_{in}(r)}{dr}\right)_{r=R} = -KR\,tan\,(KR + \alpha + iq) \tag{A.3}$$

A resonance is characterized by the a perfect match of the wave function amplitude in the interior and in the exterior. This correspond to an easy penetration of the incident particle and the cross section has a maximum. In other words, the logarithmic derivative is zero at r=R. The Equation A.3 then became:

$$f_0 = -KR\,tan\,(KR + \alpha + iq) = 0 \tag{A.4}$$

At the energy E,

$$f_0 \approx f_0(E,q) + (E - E0)\left(\frac{\partial f_0}{\partial E}\right)_{E,q=0} - iqKR \tag{A.5}$$

and finally, plugging eq in eq, the reaction corss section is:

$$\sigma_{re,0} = \frac{\pi}{k^2} \frac{\frac{(2kR)(2qKR)}{(\partial f_0/\partial E)^2_{E0,q=0}}}{(E - E0)^2 + \frac{(qKR+kR)^2}{(\partial f_0/\partial E)^2_{E0,q=0}}} \tag{A.6}$$

At this point we introduce the definitions:

$$\Gamma_{\lambda e} \equiv -\frac{2kR}{(\partial f_0/\partial E)_{E0,q=0}} \qquad (particle\ width) \tag{A.7a}$$

$$\Gamma_{\lambda r} \equiv \frac{2qKR}{(\partial f_0/\partial E)_{E0,q=0}} \qquad (reaction\ width) \tag{A.7b}$$

$$\Gamma_{\lambda} \equiv \Gamma_{\lambda e} + \Gamma_{\lambda r} \qquad (total\ width) \tag{A.7c}$$

so became:

$$\sigma_{re,0} = \frac{\pi}{k^2} \frac{\Gamma_{\lambda e}\Gamma_{\lambda r}}{(E - E0)^2 + \Gamma_{\lambda}^2/4} \tag{A.8}$$

Which is known as the $Breit - Wigner formula$ for s-wave ($l = 0$) neutrons.

The particle width is slipt into two factors. The first depend only on the energy and on the conditions outside the nucleus, while the sedond factor is called reduced width and incorporae the properies of thenuclear interior, and is independent on the channel energy..

$$\Gamma_{\lambda e} \equiv 2P_0\gamma_{\lambda e}^2 \qquad with \qquad \gamma_{\lambda e}^2 \equiv -\left(\frac{\partial f_0}{\partial E}\right)_{E0,q=0} \tag{A.9}$$

A.0.2 The Breit-Wigner formula for charged particles and arbitrary l

The radial wave function, solution of the Schrodinger equation outside the nuclear surface, are no longer spherical waves, but in case of neutrons are given by the spherical Bessel and Neumann functions F_l=(j_l) and G_l=(kr)n_l(r), while are the Coulomb wave functions in case of charged particles.

eq A.2a became

$$u_{in} = Ae^{-i\sigma_l}[G_l(r) + iF_l(r)] + B^{i\sigma_l}[G_l(r) - iF_l(r)] \tag{A.10}$$

Like in the previous case, the continuity of the logarithmic derivative at r=R:

$$R\left(\frac{1}{u_{in}^{+}(r)}\frac{du_{in}^{+}(r)}{dr}\right)_{r=R} \tag{A.11a}$$

$$= R\left[\frac{G_l(dG_l/dr) + F_l(dF_l/dr) + iG_l(dF_l/dr) - iF_l(dG_l/dr)}{F_l^2 + G_l^2}\right]_{r=R} \tag{A.11b}$$

$$\equiv S_l + iP_l \tag{A.11c}$$

where:

$$S_l = R\left[\frac{G_l(dG_l/dr) + F_l(dF_l/dr)}{F_l^2 + G_l^2}\right]_{r=R} \quad and \tag{A.12a}$$

$$P_l = R\left(\frac{k}{F_l^2 + G_l^2}\right)_{r=R} \tag{A.12b}$$

and eq ?? became:

$$\sigma_{re,l} = (2l+1)\frac{\pi}{k^2}\frac{\Gamma_{\lambda e}\Gamma_{\lambda r}}{(E-E0)^2+\Gamma_\lambda^2/4} \tag{A.13}$$

$$\Gamma_{\lambda e} \equiv -\frac{2P_l(E)}{(\partial f_l/\partial E)_{E_\lambda,q=0}} = 2P_l\gamma_{\lambda e}^2 \qquad (particle\ width) \tag{A.14a}$$

$$\Gamma_{\lambda r} \equiv \frac{2qKR}{(\partial f_0/\partial E)_{E0,q=0}} \qquad (reaction\ width) \tag{A.14b}$$

$$\Gamma_\lambda \equiv \Gamma_{\lambda e} + \Gamma_{\lambda r} \qquad (total\ width) \tag{A.14c}$$

$$E_r \equiv E_\lambda + \frac{S_l(E)}{(\partial f_l/\partial E)_{E0,q=0}} = E_\lambda - S_l(E)\gamma_{\lambda e}^2 \qquad (resonance\ energy) \tag{A.14d}$$

From this equations, it is clear the meaning of P_l and S_l. The penetration factor appears in the particle width, while the shift factor causes the observed resonance to be different from the level energy E_λ.

So far we have only discussed the single-channel case. The genearlization to multiple channels is provided by the RT-matrix formalism.

for a target with j_t and projectile with j_p, the possible values of the resonance that can be populated is

J=j1+j2+l.

$$\sigma_{re} = \frac{\pi}{k^2}\frac{2J+1}{(2jp+1)(2jt+1)}\frac{(\sum_{ls}\Gamma_{\lambda c})(\sum_{l's'}\Gamma_{\lambda c'})}{(E-E_\lambda-\Delta_\lambda)^2+\Gamma_\lambda^2/4} \tag{A.15}$$

with:

$$\Gamma_{\lambda c}(E) = 2P_c(E)\gamma_{\lambda c}^2 \tag{A.16a}$$

$$\Gamma_{\lambda}(E) = \sum_{c''} \Gamma_{\lambda c''}(E) \tag{A.16b}$$

$$\Delta_{\lambda}(E) = \sum_{c''} \Delta_{\lambda c''(E)} \tag{A.16c}$$

$$\Delta_{\lambda c}(E) = -\left|S_c(E) - B_c\right| \gamma_{\lambda c}^2 \tag{A.16d}$$

$$\beta(E) = arctan \frac{\Gamma_{\lambda}(E)}{2[E_{\lambda} - E + \Delta_{\lambda(E)}} \tag{A.16e}$$

The partial width $\Gamma_{\lambda c}$ correspond to the decay (or formation) probability of level λ through a particular channel c.

A.0.3 partial and reduces width

So far we have described single-particle resonances. However, bp-emission occur troe very narrow and closely spaced that cannot explained by single-particle potentials. They are indeed described as interaction between many nucleon in the nucleus. Such a fine structure results from the many ways in which a many-body system can be excited.

Formally:

$$\begin{aligned} H =& H_{\zeta}^t + T_K^p(r) + \sum_{i=1}^{A} V_i(\bar{\zeta}, x) \\ =& [H_{\zeta}^t + T_K^p(r) + \bar{V}_i(\bar{\zeta}, x)] + [-\bar{V}(r) + \sum_{i=1}^{A} V_i(\bar{\zeta}, x)] \\ =& H_0 + H' \end{aligned} \tag{A.17}$$

The potential $\bar{V}(r)$ give rise to escribe single particle states, while the residual interaction H' causes these states to split into a large number of states. Each of them is carachterize by a distinct complicated muxure of wavr functions, and hence a γ^2 in general differ fffor each state. Each one of these state can in principle be observed in the cross section, and the average coss section recall the single particle resonance.

Radial wave function of a compound state expanded in the basis of the single-particle radial wave function u_{pc}.

$$u_c(R) = \sum_p A_{\lambda pc} u_{pc}(R) \tag{A.18}$$

for the above discussion, there is one state in the previous that dominates so :

$$u_c(R) \approx A_{\lambda pc} u_{pc}(R) \tag{A.19}$$

Because the partial width is the decay (formation) of the level λ through the channel c, it can be calculated integrating the current though a sphere of radius R over the intere solid angle. To describe the decay of the compound state, the wave function for r>R is purely outgoing, so described only by u_{pc}=A u^+_{pc}. It results hence that:

$$\Gamma_{\lambda c} = 2\frac{\hbar^2}{mR^2} P_c A^2_{\lambda pc} \frac{R}{2} \left| u_{pc}(R) \right|^2 \tag{A.20}$$

and this can be expressed as:

$$\Gamma_{\lambda c} = 2\frac{\hbar^2}{mR^2} P_c C^2 S \theta^2_{pc} \tag{A.21}$$

with:

$$C^2 S = A^2_{\lambda pc} \tag{A.22a}$$

$$\theta^2_{pc} = \frac{R}{2} \left| u_{pc}(R) \right|^2 \tag{A.22b}$$

Appendix B

Table of the known βp-emitters near the proton drip line

Table B.1: Table of the known bp-emitters with relative half-life, and when availble bp-branching ratio. All of these nuclei are close to the rp-process path

Nucleus	J^{π}	half-life	decay mode, bbp
^{9}C	(3/2-)	126.5 ms 9	$\beta^{+}p = 61.6$
^{13}O	(3/2-)	8.58 ms 5	$\beta^{+}p$ 100
^{17}Ne	1/2-	109.2 ms 6	ecp 100
^{20}Mg	0+	90.8 ms 24	$\beta^{+}p$ 27
^{21}Mg	5/2+	122 ms 3	$\beta^{+}p = 32.6$ 10
^{22}Al	(3)+	59 ms 3	B+2P = 0.9 5
^{22}Al	(3)+	59 ms 3	$\beta^{+}p$ 60
^{23}Al	5/2+	470 ms 30	$\beta^{+}p = 0.46$ 23

Continued on next page

Table B.1 – continued from previous page

Nucleus	J_π	half-life	decay mode, bbp
^{24}Al	4+	2.053 s 4	β^+p = 0.0016 3
^{22}Si		29 ms 2	β^+p = 32 4
^{23}Si	(5/2)+	42.3 ms 4	ecp = 71 3
^{23}Si	(5/2)+	42.3 ms 4	EC2P = 3.6 4
^{24}Si	0+	140 ms 8	β^+p = 38 4
^{25}Si	5/2+	220 ms 3	β^+p = 35 2
^{26}P	(3+)	20 ms +35-15	β^+p 0.9
^{26}P	(3+)	20 ms +35-15	B+2P 1
^{27}P	1/2+	260 ms 80	β^+p = 0.07
^{28}P	3+	270.3 ms 5	ecp = 0.0013 4
^{27}S	(5/2+)	21 ms 4	B+2P = 2.0 10
^{27}S	(5/2+)	21 ms 4	β^+p = ?
^{28}S	0+	125 ms 10	ecp = 20.7 20
^{29}S	5/2+	187 ms 4	ecp = 47 5
^{31}Cl		150 ms 25	β^+p = 0.7
^{32}Cl	1+	298 ms 1	ecp = 0.026 5
^{31}Ar	5/2(+)	14.4 ms 6	ecp = 63 7
^{31}Ar	5/2(+)	14.4 ms 6	EC2P = 7.2 11
^{32}Ar	0+	98 ms 2	ecp = 43 3
^{33}Ar	1/2+	173.0 ms 20	ecp = 38.7 10
^{35}K	3/2+	178 ms 8	ecp = 0.37 15
^{36}K	2+	342 ms 2	ecp = 0.048 14
^{35}Ca		25.7 ms 2	ecp = 95.7 14

Continued on next page

Table B.1 – continued from previous page

Nucleus	J_π	half-life	decay mode, bbp
^{35}Ca		25.7 ms 2	EC2P = 4.2 3
^{36}Ca	0+	102 ms 2	ecp = 54.3 15
^{37}Ca	3/2+	181.1 ms 10	ecp = 82.1 7
^{40}Sc	4-	182.3 ms 7	ecp = 0.44 7
^{40}Ti	0+	53.3 ms 15	ecp = 100
^{41}Ti	3/2+	80.4 ms 9	ecp 100
^{42}Cr	0+	13.3 ms 10	ecp = 94.4 50
^{43}Cr	(3/2+)	21.6 ms 7	B+2P = 6 5
^{43}Cr	(3/2+)	21.6 ms 7	β^+p = 23 6
^{44}Cr	0+	53 ms +4-3	ecp ¿ 7 3
^{45}Cr	(7/2-)	60.9 ms 4	β^+p = 34.4 8
^{46}Mn	(4+)	36.2 ms 4	ecp = 57.0 8
^{47}Mn	(5/2-)	100 ms 50	ecp 3.4 9
^{48}Mn	4+	158.1 ms 22	β^+p = 0.28 4
^{45}Fe	(3/2+)	1.89 ms +49-21	β^+p 43 10
^{46}Fe	0+	13.0 ms 20	ecp = 78.7 38
^{47}Fe	(7/2-)	21.8 ms 7	EC2P = ?
^{47}Fe	(7/2-)	21.8 ms 7	ecp 0
^{48}Fe	0+	44 ms 7	ecp ¿ 3.6 11
^{49}Fe	(7/2-)	64.7 ms 3	β^+p = 56.7 4
^{50}Fe	0+	155 ms 11	β^+p 0
^{50}Co	(6+)	44 ms 4	ecp ¿ 54 13
^{49}Ni		7.5 ms 10	β^+p = 83 13

Continued on next page

Table B.1 – continued from previous page

Nucleus	J_π	half-life	decay mode, bbp
^{52}Ni	0+	38 ms 5	β^+p = 17.0 14
^{53}Ni	(7/2-)	45 ms 15	β^+p 45
^{57}Zn	(7/2-)	40 ms 10	β^+p 65
^{58}Zn	0+	86 ms 8	ecp ¡ 3
^{59}Zn	3/2-	182.0 ms 18	ecp = 0.10 3
^{60}Ga	(2+)	70 ms 13	β^+p = 1.6 7
^{61}Ga	3/2-	167 ms 3	ecp ¡ 0.25
^{61}Ga	3/2-	167 ms 3	ecp ¡ 0.25
^{60}Ge	0+	¿ 110 ns	ecp = ?
^{61}Ge	(3/2-)	44 ms 6	ecp ¿ 58
^{69}Se	(1/2-,3/2-)	27.4 s 2	ecp = 0.045 10
^{70}Kr	0+	52 ms 17	ecp 1.3
^{71}Kr		64 ms +8-5	ecp = 5.2 6
^{72}Kr	0+	17.1 s 2	ecp ¡ 1E-6
^{73}Kr	3/2-	27.3 s 10	ecp = 0.25 3
^{73}Sr		¿ 25 ms	ecp ¿ 0
^{75}Sr	(3/2-)	71 ms +71-24	ecp = 6.5 33
^{77}Sr	5/2+	9.0 s 2	ecp ¡ 0.25
^{77}Y	(5/2+)	57 ms +22-12	ecp = ?
^{78}Y	(0+)	53 ms 8	ecp = ?
^{79}Y	(5/2+)	14.8 s 6	ecp = ?
^{80}Y	(4-)	30.1 s 5	ecp = ?
^{79}Zr		56 ms 30	ecp = ?

Continued on next page

Table B.1 – continued from previous page

Nucleus	J_π	half-life	decay mode, bbp
^{80}Zr	0+	4.6 s 6	ecp = ?
^{81}Zr	(3/2-)	5.5 s 4	ecp = 0.12 2
^{83}Zr	(1/2-)	41.6 s 24	ecp = ?
^{82}Nb	(0+)	50 ms 5	ecp = ?
^{82}Nb	(0+)	50 ms 5	ecp = ?
^{84}Nb	(1+,2+,3+)	9.8 s 9	ecp = ?
^{84}Mo	0+	2.3 s 3	ecp = ?
^{87}Mo	7/2+	14.02 s 26	β^+p = 15 8
^{86}Tc	(0+)	54 ms 7	ecp = ?
^{89}Ru	(9/2+)	1.5 s 2	ecp ¡ 0.15
^{93}Ru	(1/2)-	10.8 s 3	ecp = 0.027 5
^{94}Rh	(4+)	70.6 s 6	ecp = 1.8 5
^{93}Pd	(7/2+,9/2+)	0.79 s 17	ecp = ?
^{95}Pd	(21/2+)	13.3 s 3	β^+p = 0.90 16
^{94}Ag	(0+)	26 ms +26-9	ecp = ?
^{94}Ag	(21+)	0.40 s 4	ecp = 27
^{98}Ag	(6+)	47.5 s 3	ecp = 0.0011 5
^{97}Cd	(9/2+)	2.8 s 6	ecp = ?
^{98}Cd	0+	9.2 s 3	ecp ¡ 0.025
^{99}Cd	(5/2+)	16 s 3	β^+p = 0.17 +11-5
^{100}In	(6+,7+)	5.9 s 2	ecp = 1.6 3
^{101}In	(9/2+)	15.1 s 3	β^+p = ?
^{102}In	(6+)	23.3 s 1	β^+p = 9.3E-03 13

Continued on next page

Table B.1 – continued from previous page

Nucleus	J_π	half-life	decay mode, bbp
^{100}Sn	0+	0.86 s +37-20	ecp ¡ 17
^{101}Sn	(5/2+)	1.7 s 3	ecp = 26
^{103}Sn	(5/2+)	7.0 s 2	ecp = 1.2 1
^{105}Sn	(5/2+)	34 s 1	β^+p = ?

Appendix C

K/β^+ ratio for allow transitions

Fig.C.1 shows a number of curves representing the k/b+ ratio for a given atomic number Z. For each Z, two curves are defined, one continius and one dashed, that cover two complementary energy ranges between 0.14 MeV and 6 MeV. The k/b+ ratio relative to the continius curves, have to be red on the left y-axis, while the k/b+ rastio relative to the dashed one has to be red on the right y-axis. Left and right y-axis have different scale. The range of Z rapresented range from 15-85 in steps of 10. The Z not rapresented in the plot can be extrapolated using the other curves.

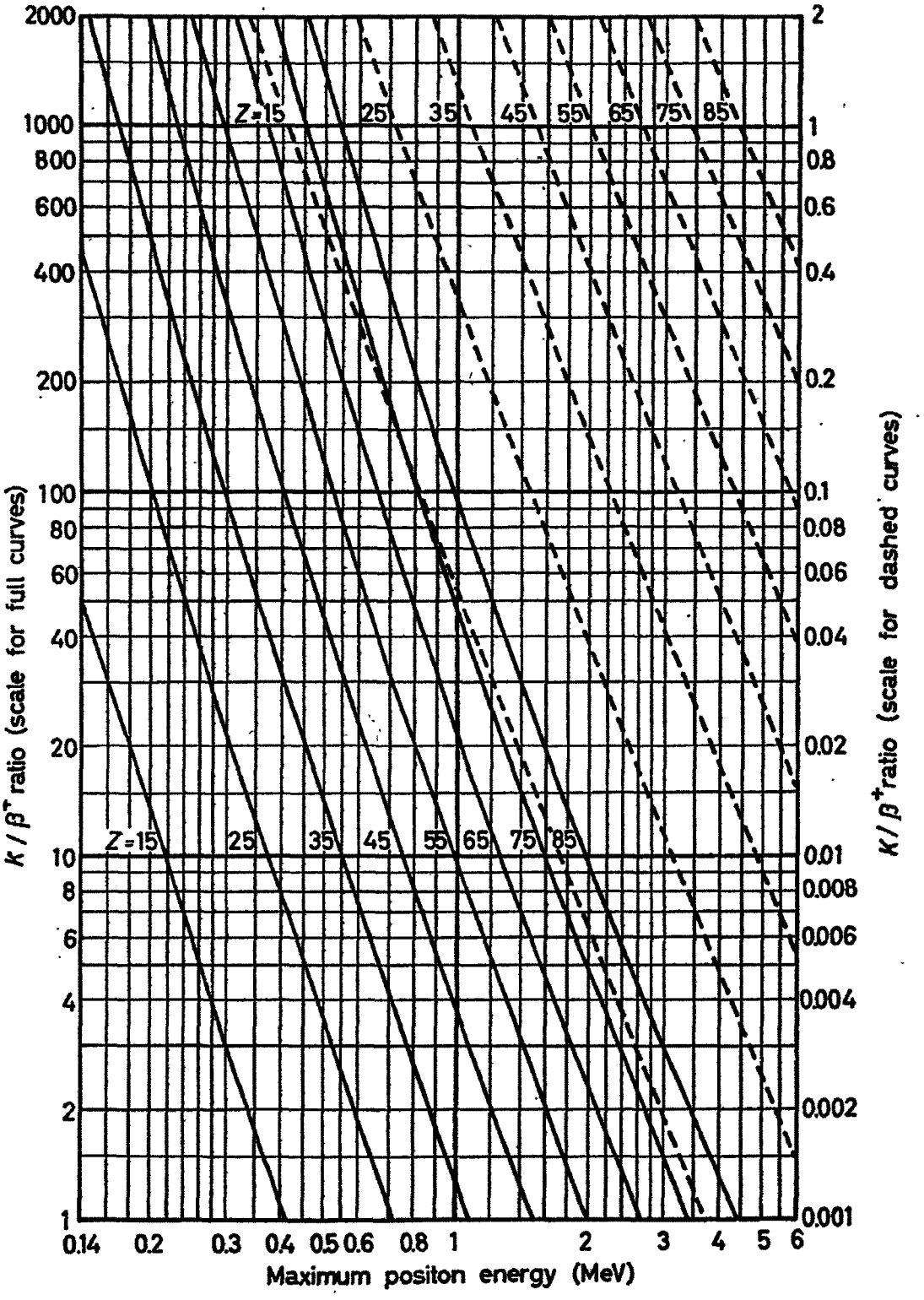

Figure C.1: Theoretical K/β^+ ratio for allowed transitions

BIBLIOGRAPHY

[1] K. Ogawa. *Phys. Rev. C*, 28(958), 1983.

[2] K. Schmidt et al. *Nucl. Phys. A*, 624(492), 1997.

[3] L. Batist et al. *Nucl. Phys. A*, 720:245–273, 2003.

[4] H. Grawe et al. *Eur. Phys. J. A*, 25:357, 2005.

[5] I. Mukha et al. *Phys. Rev. C*, 70(4):044311, 2004.

[6] A Escuderos and L Zamick. *Phys. Rev. C*, 73(4):044302, 2006.

[7] S.N. Liddick et al. *Phys. Rev. Lett.*, 583:857–860, 2006.

[8] E. Nolte et al. *Z. Phys. A*, 305:289–294, 1982.

[9] J. Doring et al. *Phys. Rev. C*, 68(034306), 2003.

[10] N. Marginean et al. *Phys. Rev. C*, 67(061301(R)), 2003.

[11] D. Bazin et al. *Nucl. Instr. Meth. Phys. Res. A*, 606(411c), 2009.

[12] D. Sewerniak et al. *Frontiers in nuclear structure, astropjyiscs, and reactions: FINUSTAR 2. AIP Conference Proceedings*, 1012:79–83, 2008.

[13] S.E. Wallace et al. *Astrophy. J. s.*, 45(375):389–420, 1981.

[14] T. Strohmayer and L. Bildsten. *Compact stellar X-ray sources*, pages 113–156, 2006.

[15] H. Schatz and K.E. Rehm. *Nucl. Phys. A*, 777:601–622, 2006.

[16] S. Gupta et al. *Astrophys. J.*, 662:1188–1197, 2007.

[17] J.B. Stoker et al. *Phys. Rev. C*, 79(015803), 2009.

[18] R.N. Boyd. *Proton-Emitting Nuclei: PROCON '99*, 518(239-245), 1999.

[19] A. Honkanen et al. *Nucl. Phys. A*, 611:47, 1996.

[20] K. Takahaski et al. *Atomic Data and Nuclear Data Tables*, 12:101, 1973.

[21] J.C. Hardy. *Phys. Lett.*, 63B(1):27, 1976.

[22] P. Hornshoj et al. *Nucl. Phy. A*, 187(609), 1972.

[23] V.I. Goldansky et al. *Nucl. Phys.*, 19:482, 1960.

[24] V.A. Karnauklov et al. *Proc. Asilomar Conf. on Reactions Between Conplex nuclei*, page 434, 1963.

[25] R. Barton et al. *Can. J. Phys.*, 41(2007), 1963.

[26] J. Cerny et al. *Ann. Rev. Nucl. Sci.*, 27:333, 1977.

[27] j. Aysto et al. *Phys. Scr.*, T5:193, 1983.

[28] V. Banerjee et al. *J. Phys. G.*, 24:1403, 1998.

[29] S. Czajkowski et al. *Nucl. Phys. A*, 616:278c, 1997.

[30] B. Blank et al. *Prog. Par. Nucl. Phys.*, 60:403, 2008.

[31] M.J.G. Borge et al. *Hyperfine Interaction*, 129:97, 2000.

[32] D.M. Moltz et al. *Particle Emission from Nuclei*, III:133, 1989.

[33] J. Giovinazzo et al. *Nucl. Phys. A*, 674:394, 2000.

[34] W.X. Huang et al. *Phys. Rev. C*, 59(5):2402, 1999.

[35] W. Kurcewicz et al. *Z. Phys. A*, 308, 1982.

[36] K. Schmidt et al. *Eur. Phys. J. A*, 8, 2000.

[37] S.W. Xu et al. *Eur. Phys. J. A*, 11, 2001.

[38] C. Plettener et al. *Phys. Rev. C*, 66(044319), 2002.

[39] A. Stolz. Phd thesis. Technical report, TU Munchen, 2001.

[40] A. Kavatsyuk et al. *Eur. Phys. J. A.*, 31:319–325, 2007.

[41] A.L. Goodman. *Phys. Rev. C*, 58:R3051, 1998.

[42] D.S. Brenner et al. *Phys. Lett. B*, 243:1, 1990.

[43] H. Sagawa et al. *Phys. Rev. C*, 48(R960), 1993.

[44] G.Q. Li et al. *Phys. Rev. C*, 58:1393, 1998.

[45] M. Sandzelius et al. *Phys. Rev. Lett.*, 99(022501), 2007.

[46] S. Grodzins et al. *Phys. Lett. B*, 2:88, 1962.

[47] S. Raman et al. *At. Data Nucl. Data Tables*, 42:1, 1989.

[48] B. Hadinia et al. *Phys. Rev. C*, 72(041303), 2005.

[49] C. Vaman et al. *Phys. Rev. Lett.*, 99(162501), 2007.

[50] A. Banu et al. *Phys. Rev. C*, 72(061305(R)), 2005.

[51] R. Wadsworth et al. *Acta Physica polonica B*, 40(3):611, 1990.

[52] D.J. Rowe et al. *Phys. Rev. Lett.*, 87(17), 2001.

[53] A.F. Lisetskiy et al. *Phys. Rev. C*, 70(044314), 2004.

[54] J.J. Ressler et al. *Phys. Rew. C*, 69(034317), 2004.

[55] F. Haberl et al. *Astrophys. J.*, 314:266, 1987.

[56] J.E. Grindal et al. *Astrophys. J.*, 221:234, 1978.

[57] J.A. hackwell et al. *Astrophys. J.*, 233:115, 1979.

[58] Van Paradijs et al. *Accretion Driven Stellar X-ray Sources*, Cambridge University Press:191, 1983.

[59] Pedersen et al. *Nature*, 294:725, 1981.

[60] W.H.G. Lewin et al. *Space Sci. Rev.*, 62:223, 1992.

[61] Lawrance et al. *Astrophys. J.*, 267:301, 1983.

[62] A. Kong et al. *Mon. Not. R. Astron. Soc.*, 2000.

[63] Schatz et al. *Phys. Rev. Lett.*, 86(16), 2001.

[64] N. Weinberg et al. *Astrophys. J.*, 639(1018), 2006.

[65] J.J.M. in Zand et al. *Astronomy Astrophysics*, 16(13952), 2010.

[66] D. Bazin et al. *Phys. Rev. Lett.*, 101(252501), 2008.

[67] D.J. Morrisey et al. *Nucl. Instr. Meth. Phys. Res. B*, 204:90–96, 2003.

[68] M. Mocko. *Ph.D thesis, Michigan State University*, 2006.

[69] A. Stolz et al. *Nucl. Instr. and Meth. Phys. Res. B*, 241:858, 2005.

[70] O. Tarasov and D. Bazin. *Nucl. Phys. A*, 764(411c), 2004.

[71] M. Hellstrom et al. *Z. Phys. A*, 1990.

[72] K. Schmidt et al. *Z. Phys. A*, 350, 1994.

[73] S.Baker et al. *Nucl. Inst. Meth.*, 221:437, 19842003.

[74] P.R. Bevington and D.K. Robinson. *Data Reduction and Error Analysis for Physical Science 2^{nd} ed.*, (McGraw-Hill, Boston), 1992.

[75] P.T. Hosmer. *Ph.D. thesis, Michigan State University*, 2005.

[76] S. Goudsmith et al. *Phys. Rev.*, 57:24, 1940.

[77] L. Landau. *J. Phys. USSR*, 8:201, 1944.

[78] O. Blunck and S. Leisegang. *Z. Phys.*, 128:500, 1950.

[79] N. Reynaert et al. *Med. Phys.*, 29(10):2246–2454, 2002.

[80] Schaart et al. *Phys. Med. Biol.*, 47:1459–1484, 2002.

[81] Z. Janas et al. *Phys. Scr. T*, 308(56):262–265, 1995.

[82] P. Kienle et al. *Prog. Part. Nucl. Phys.*, 2001.

[83] M. Lipoglasek et al. *Phys. Rev. C*, 97(082501), 205.

[84] A.H. Wapstra G. Audi and C. Thibault. The ame2003 atomic mass evaluation (ii). *Nucl. Phys. A*, 729, 2003.

[85] Schatz et al. *Phys. Rep. 294*, 294:167–263, 1998.

[86] H.A. Roth et al. *Phys. Rev. C.*, 50:1330, 1994.

[87] M. Hencheck et al. *Phys. Rev. C.*, 50(4), 1994.

[88] E. Wefer et al. *in Proceedings of the AIP Conf. Proc.*, 495(375), 1999.

[89] A. Stolz. in proceedings of pingst 2000. Technical report, Lund, Sweden, p.113, 2000.

[90] J.C. Hardyet al. *Phys. Lett. B*, 109(242), 1982.

[91] S-H. Zhou et al. *Chin. Phys. Lett.*, 16(18), 1999.

[92] S. Dean et al. *Eur. Phys. J. A*, 21:243–255, 2004.

[93] J. Fallis et al. *Phys. Rev. C*, 78(022801(R)), 2008.

[94] A. Kankainen et al. *Phys. Rev. Lett.*, 101(142503), 2008.

[95] E. Nolte et al. *Z. Phys. A*, 298(191), 1980.

[96] S.E. Arnell et al. *Z. Phys. A*, 346(111), 1993.

[97] M. Gorska et al. *Acta Phys. pol B*, 27(165), 1996.

[98] C. Lingk et al. *Phys. Rev. C*, 56(R2349), 1997.

[99] J. Szerypo et al. *Nucl. Phys. A*, 584:221–240, 1995.

[100] A. Stolz et al. *International Nuclear Physics Conference, AIP Conf.*, (Proc. No.610 (AIP, Melville,NY,):728, 2002.

[101] K. Schmidt et al. 2008.

[102] R.H. Cyburt.

[103] R.N. Boyd et al. *Int. Symp. Origin of Matter and Evolution of Galaxies 97*, page 350, 1998.